Stony Brook University

Bolometric effect and phonon cooling in graphene-superconductor junctions

A Dissertation presented

by

Heli Vora

to

The Graduate School

in Partial Fulfillment of the

Requirements

for the Degree of

Doctor of Philosophy

in

Physics

Stony Brook University

August 2014

Stony Brook University

The Graduate School

Heli Vora

We, the dissertation committe for the above candidate for the

Doctor of Philosophy degree, hereby recommend

acceptance of this dissertation

Xu Du - Dissertation Advisor
Assistant Professor, Department of Physics and Astronomy

Philip Allen - Chairperson of Defense
Professor, Department of Physics and Astronomy

Jin Koda
Assistant Professor, Department of Physics and Astronomy

Leon Shterengas
Associate Professor, Department of Electrical Engineering
Stony Brook University

This dissertation is accepted by the Graduate School

Charles Taber
Dean of the Graduate School

Abstract of the Dissertation

Bolometric effect and phonon cooling in graphene-superconductor junctions

by

Heli Vora

Doctor of Philosophy

in

Physics

Stony Brook University

2014

Graphene, a two-dimensional allotrope of graphite, possesses remarkable electronic properties which stem from the fact that the electrons in graphene are described by the Dirac-Weyl Hamiltonian. As a result, graphene exhibits a linear energy dispersion relation with zero effective mass. With its single-atomic-layer thickness, not only electrons but also phonons are of a two dimensional nature, differentiating graphene from the conventional semiconductor based two-dimensional electron gas systems. The combination of two-dimensional phonons, ultra small volume, low density of states and linear energy spectrum allows graphene to have weak electron-phonon coupling and extremely small electronic heat capacity. These properties make it a desirable material for use in a bolometer device, which is a sensitive electromagnetic radiation detector.

We present a novel device design, which combines graphene with superconducting contacts and investigate its bolometric response. Two configurations of superconductor (S)- graphene(G)- superconductor(S) Josephson junction (SGS) and superconductor(S)- insulator(I)- graphene(G) (SIGIS) tunnel junction are studied. Devices with aluminum, niobium and niobium nitride as superconducting contacts are studied. In SIGIS tunnel junctions, titanium oxide is used as the barrier oxide to achieve high efficiency impedance

matched bolometers. In these devices, "hot electrons" are created via application of microwave radiation and their relaxation to the bath temperature is studied. With the hot electrons effectively confined by the superconducting contacts, we demonstrate electron cooling via phonon interactions. This device geometry allows us to study electron-phonon coupling in single and bilayer graphene at low temperatures. In single layer graphene, a disorder-modified temperature dependence of electron-phonon cooling power is observed. And in bilayer graphene, it is shown that the electron-phonon coupling parameter has an inverse dependence on the chemical potential, opposite to that found in single layer graphene.

To my family,
For their constant support.

Contents

List of Figures

List of Tables

Acknowledgements

Many individuals have helped me realize my childhood dream of studying physics and this thesis is dedicated to all of them. The individual with the biggest contribution towards this achievement is my thesis advisor, Dr. Xu Du. Being his first student, I was fortunate to learn everything directly from him, which makes me believe I got the best training possible. His hard work and enthusiasm are contagious and I thank him for bringing out the abilities in me, I never knew I was capable of. He has shaped my critical thinking and scientific reasoning and has helped me mature as a physicist from an amateur enthusiast. He has always been very approachable and answered even the stupidest of my questions with patience. He is the finest scientist I know who has fantastic experimental capabilities and if I can become even half the physicist he is, I would be very fortunate. I do hope I have proved worthy of being his first PhD student. It has been an absolute thrill to work with him these past few years.

One of the important aspects of this dissertation was the collaboration with Prof. Dan Prober at Yale University. I would like to thank members of his group, Chris McKitterick, Daniel Santavicca and Joel Chudow for their collaborative work and their technical assistance. The collaboration has been immensely helpful and I have gained much from the visits to Yale and numerous discussions with Dan. I thank him for his careful readings of my papers and for sharing his wealth of knowledge.

I would also like to thank all the members of the Physics department at Stony Brook, who have stood by me during very crucial stages of my doctoral studies. I thank professors Marivi Fernandez-Serra, Peter Stevens, Matthew Dawber, K.K. Likharev, Harold Metcalf, Tom Weinacht and Laszlo Mihaly for their support. I would like to thank professor Matthew Dawber for readily providing his guidance whenever needed and for the use of their AFM.

I would like to thank all my fellow group members, Fen Guan, Mohammed Humed Yusuf, Piranavan Kumaravadivel, Naomi Mizuno, Peter Beierle, Mike Mienko and Rick Darienzo for providing a very healthy and fun-filled work environment and especially for all their help with fixing/building lab equipment whenever needed. Without them, long hours in lab would have been very dull indeed. Thanks to Benjamin Bein for his help with the AFM and

spending many hours in helping with my scans. I would especially like to thank Bent Nielsen, who was always ready to help with anything I needed. I thank him for all the metal evaporations, his help with the sputter chamber, measurement setup, helium and nitrogen handling and almost all aspects of lab work. His technical expertise has been of great help in my dissertation research. I would like to thank all the machine shop staff, Mark Jablonski, Paul DiMatteo, Jeff Slechta, Walter Schmeling and Jeff Thomas for their help in building my measurement setup. I would also like to thank Sara, Pernille, Socoro, Pat and the wonderful people in the Physics main office who made sure I never had to worry about any administrative trouble.

Life without friends at Stony Brook would not have been possible and I want to thank Betul Pamuk, Murat Kurtcephe, Marija Kotur, Luana Pedroza, Manas Kulkarni, Karin Gilje, Shawn Pollard, Rahul Patel, Aruna B., Upasna Thapar and Manisha Rao for making my days at Stony Brook enjoyable. I would especially like to extend my thanks to Sriram Ganeshan, Divya Bhatnagar and Chee Sheng Fong for their constant support and all the help.

Most of all, I owe all that I am today to my most wonderful family. The childhood support and encouragement that I have gotten from my parents has helped me build a confidence in myself and to go after my dreams. My parents, Chetan and Trupti, have sacrificed much for their children's benefit; even uproot their lives for a year so that we could get the best education in the world. With their support and encouragement, I have been able to fly as high as I want, always knowing that if I ever fell, they would be there to catch me. I do hope that I have proved worthy and made them proud. I would also like to thank my sister, Nemi, who is the one person in this world who knows and understands me the most. Even though she is younger than me, she has been patient and mature when dealing with my many complains of grad-school life away from home.

Last but not the least, I would like to thank Tanuj for standing by me, understanding and sharing my passions and providing his support in all aspects of my life. I could not have gone through last six years without you and I do hope we have many more science-filled years of togetherness to come!

1 Introduction to the Electronic Properties of Graphene

In this chapter, a brief review of some of the relevant electronic properties of graphene is presented, including a short derivation of graphene's tight binding band structure and the theory of hot electron cooling through electron-phonon interactions, which will be useful for later discussion of the results.

1.1 Single layer graphene

Graphene is a single atomic layer thick sheet of graphite with carbon atoms arranged in a honeycomb crystal lattice. The unique electronic properties of graphene originate from its lattice symmetry and the atomic structure of carbon [1]. Carbon is a group IV element consisting of four outer-shell electrons. In graphene, one electron in the s-orbital combines with two of the p_x and p_y orbital electrons to form hybridized sp^2 orbitals. These form in-plane carbon-carbon σ-bonds which give rise to the high mechanical strength of graphene. 4^{th} valence electron half-occupies the p_z orbital which extends perpendicular to the graphene plane. The side-ways overlap of these orbitals forms the weak π-bonds, which determine the electrical conductivity of graphene.

1.1.1 Band structure

To calculate tight binding band structure, consider a two carbon atom unit cell in single layer graphene. These two atoms, at atomic sites, labeled A and B in Fig 1, form the basis of a triangular lattice. Even though they are chemically equivalent, physically these two carbon atoms are inequivalent due to the different neighboring environment they sense. The two lattice vectors(a's) and their reciprocal lattice vectors(b's) are given by,

$$\begin{aligned} a_1 &= \tfrac{a}{2}(\sqrt{3}, 1), \quad a_2 = \tfrac{a}{2}(\sqrt{3}, -1) \\ b_1 &= \tfrac{2\pi}{a}(\tfrac{1}{\sqrt{3}}, 1), \quad b_2 = \tfrac{2\pi}{a}(\tfrac{1}{\sqrt{3}}, -1) \end{aligned} \tag{1}$$

where $a = \sqrt{3}d_{c-c} = 2.46$ Å. d_{c-c} is the distance between two carbon atoms. Consider the carbon atom shown in red in Fig 1. Its three nearest neighbors are at coordinates given by,

$$\delta_1 = \left(\frac{a}{\sqrt{3}}, 0\right), \ \delta_2 = \left(-\frac{a}{2\sqrt{3}}, \frac{a}{2}\right), \ \delta_3 = \left(-\frac{a}{2\sqrt{3}}, -\frac{a}{2}\right) \tag{2}$$

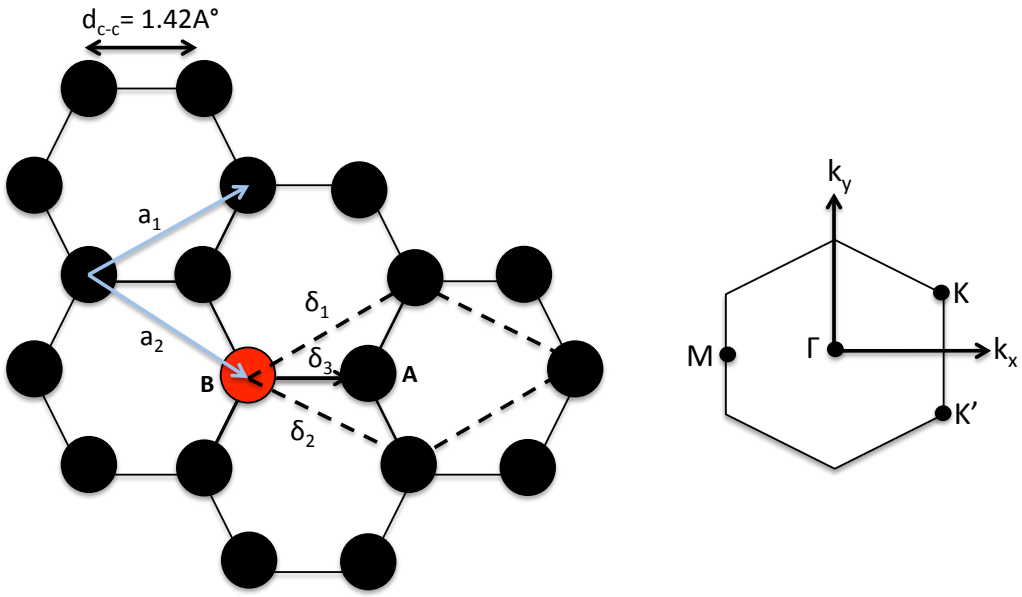

Figure 1: (left) Atomic structure of graphene. Each unit cell of the honeycomb lattice has two atomic sites (A and B). (right) First Brillouin zone of graphene with high symmetry points labeled Γ, M, K and K'.

First Brillouin zone of graphene, shown in Fig 1 (right), has high symmetry points labeled Γ, M, K and K'. Out of six corners of the hexagonal Brillouin zone, only two are inequivalent and others are related by a reciprocal lattice vector. Solving for the tight binding hamiltonian Eigenvalues would yield the energy spectrum.

$$\mathbf{H} - \mathbf{ES} = \mathbf{0}$$
$$H = \begin{pmatrix} H_{AA} & H_{AB} \\ H_{BA} & H_{BB} \end{pmatrix} \tag{3}$$

Here, **S** is the orbital overlap matrix and can be shown to be the unity matrix in graphene's case. The nearest-neighbor 2×2 hamiltonian is written as follows:

$$\begin{aligned} H_{AA} &= H_{BB} = E_{2p_z} \\ H_{AB} &= H_{BA}^* \\ H_{AB} &= t(e^{-i\mathbf{k}\cdot\boldsymbol{\delta_1}} + e^{-i\mathbf{k}\cdot\boldsymbol{\delta_2}} + e^{-i\mathbf{k}\cdot\boldsymbol{\delta_3}}) \end{aligned} \tag{4}$$

E_{2p_z} is the energy of $2p_z$ orbitals at A and B atoms and t is the nearest-neighbor hopping parameter, extracted as a fitting parameter from ab-inito simulations. In single layer graphene, $t \sim 3$ eV is found [1]. By inserting equations 4 and 2 into equation 3, the tight-binding energy spectrum of a single layer graphene is derived. Valence and conduction band energies are given as,

$$E_{\pm}(k) = \pm t\sqrt{1 + 4\cos\frac{\sqrt{3}a}{2}k_x\cos\frac{a}{2}k_y + 4\cos^2\frac{a}{2}k_y} \tag{5}$$

Two energy bands meet at K and K' points at zero energy. In undoped, intrinsic graphene the Fermi level aligns with the K and K' points where conductance and valence bands meet, also referred to as the charge neutrality points (CNP). A low energy band structure, important in experimental situations, can be arrived at by expanding Eq 5 at $k = K+q$, with $|q| << |K|$.

$$E_{\pm}(q) = \pm\hbar v_F|q| \tag{6}$$

Thus, the symmetry of the honeycomb lattice gives rise to the energy dispersion shown in Figure 2. The K and K' points are the so-called Dirac points, near which the energy dispersion is linearly conical corresponding to a Hamiltonian,

$$\hat{H} = \pm v_F\vec{\sigma}\cdot\vec{P} \tag{7}$$

where $v_F = 3ta/2\hbar \approx 10^6$ m/s is the Fermi velocity, $\vec{\sigma}$ are the Pauli matrices, and $\vec{P}$ is the momentum relative to the Dirac point. Since there are two non-identical carbon atoms per unit cell, the wave functions have the form of a spinor $\begin{pmatrix} \psi_A \\ \psi_B \end{pmatrix}$, where A and B denote the two atomic sites. This gives rise to an additional degree of freedom, the pseudospin, which describes the

distribution of the wavefunction on the two atomic sites. The pseudospin vector $\vec{\sigma}$ is either parallel or anti-parallel to the momentum vector, and $\vec{\sigma}\cdot\hat{P} = \pm 1$ ($\hat{P}$ being the unit vector of momentum) gives the chirality of the electronic excitations, the quasiparticles.

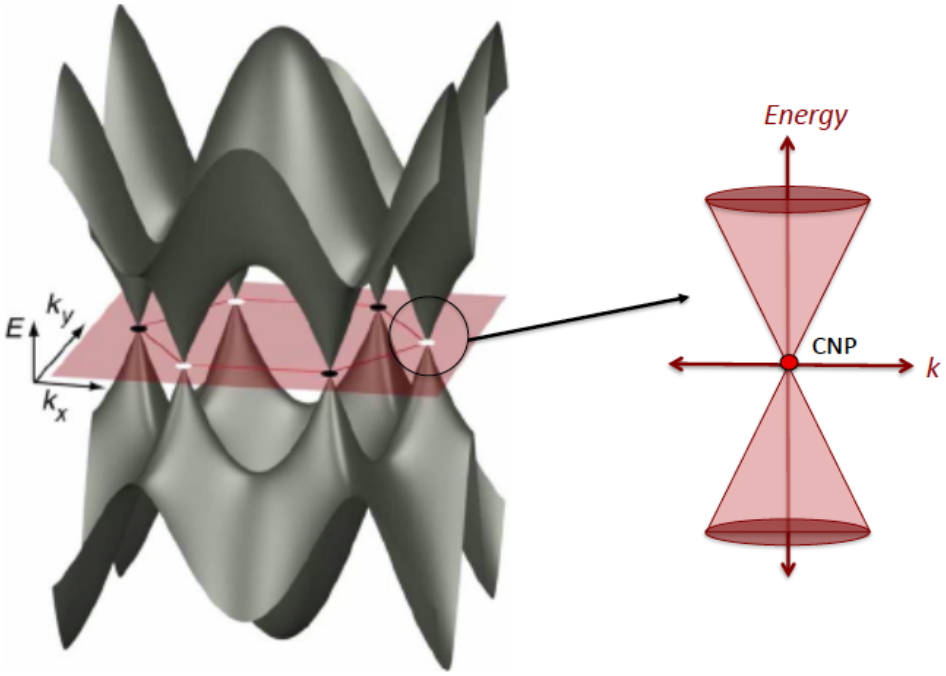

Figure 2: (left) Tight binding band structure of graphene, adapted from [2]. Valence band and conduction band meet at the corners of Brillouin zone. (right) Low energy linear dispersion relation of graphene showing the Dirac energy spectrum with charge neutrality point (CNP) as the point where valence band and conduction band meet.

1.1.2 Electronic specific heat

As a result of graphene's linear energy dispersion, the 2D electron density of states (DOS) has a linear energy dependence in graphene:

$$N(E) = \frac{2E}{\pi(\hbar v_F)^2} \tag{8}$$

where $\hbar$ is the reduced Planck constant. The DOS approaches zero at the charge-neutral Dirac point. Due to its small volume and low DOS, graphene has very small electron heat capacity ($C_{\rm e}$).

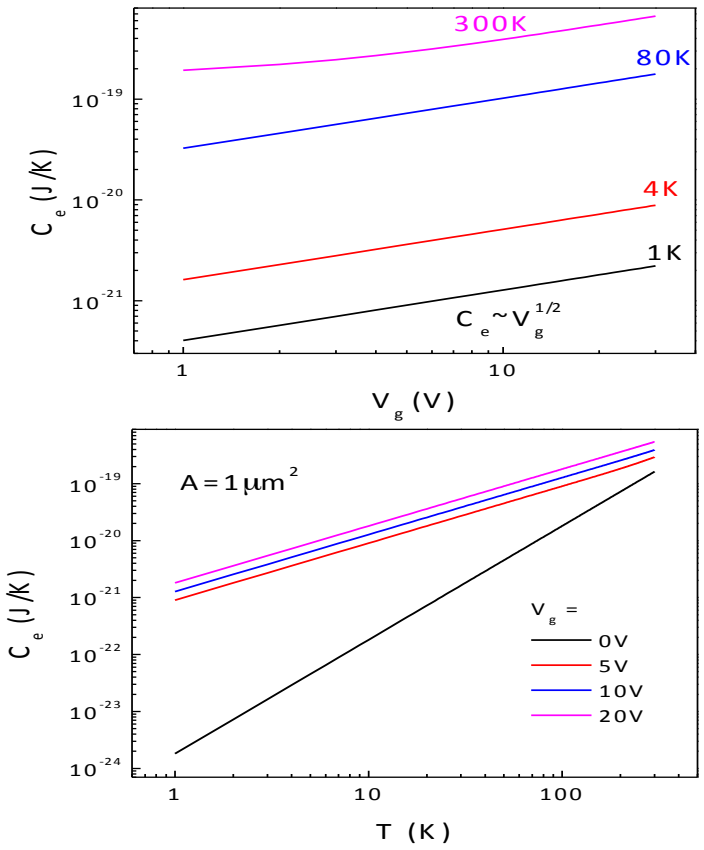

Figure 3: Calculated gate voltage (top) and temperature (bottom) dependence of the electron heat capacity for a 1 μm^2 graphene [3]. Here it is assumed that graphene sits on top of a SiO_2(300 nm)/Si substrate.

Considering the simple case of an electron gas, electronic heat capacity is given as follows:

$$C_{\rm e} = A \int \varepsilon N(\varepsilon) \frac{\partial f(\varepsilon)}{\partial T} {\rm d}E \tag{9}$$

Here, A is the area of graphene, $N(E)$ is the DOS in graphene, and $f(E)$ is

the Fermi distribution function given as,

$$f(E) = \frac{1}{(1 + e^{(E-\mu)/(k_B T)})} \tag{10}$$

Value of C_{e} in graphene, and its dependence on gate voltage and temperature can be calculated by numerically solving the integral in Eq 9 using the definitions of Eq 8 and 10. Results of this calculation are shown in Figure 3. The heat capacity depends linearly on temperature except at the Dirac point, where a T^2 dependence is expected [4]. At low temperatures and at Fermi energy the heat capacity of single layer graphene can be estimated as,

$$C_e(E_F) = \frac{\pi^2}{3} N(E_F) k_B^2 T \tag{11}$$

At experimentally relevant conditions, heat capacity in graphene can easily reach extremely small values (e.g., $C_e \sim 10^{-21}$ J/K for $T < 5$ K at $V_{\mathrm{g}} \sim 10$ V and n $\sim 7 \times 10^{11}$ cm^{-2}, for a 1 μm^2 sample). These values cannot be achieved in conventional metal structures.

1.1.3 Electrical conductivity

The conductivity of graphene can be described by the Boltzmann transport equation:

$$\sigma = \frac{e^2 v_F^2 N(E_F) \tau(k_F)}{2} \tag{12}$$

Here $N(E_F)$ is the DOS at the Fermi level, and $\tau(k_F)$ is the scattering time. Different types of charge carrier scattering mechanisms give rise to the scattering rates that depend on the Fermi wave vector/energy [5]:

$$\frac{\hbar}{\tau(k_F)} = \frac{n_i^{scatt}}{8} N(E_F) \int \mathrm{d}\theta |V_{scatt}(q)|^2 (1 - \cos^2(\theta)) \tag{13}$$

where n_i^{scatt} is the impurity density, $V_{scatt}(q)$ is the Fourier transform of the scattering potential, and $q = 2k_F sin(\theta/2)$. It is believed that the dominant scattering in graphene is from charged impurities which induce Coulomb scattering, [6, 7] with scattering time and correspondingly a conductivity

given as:

$$\tau_{k_F} \propto \frac{k_F}{n_i^C}$$
$$\sigma \propto \frac{k_F^2}{n_i^C} \propto E_F^2 \tag{14}$$

Here n_i^C is the density of the charged impurity scattering centers. Short range scattering from point defects and phonons [6, 8] also plays an important role in limiting the conductivity of graphene. In contrast to the long range Coulomb scatterers, the short range scatterers give an energy independent conductivity and corresponding scattering time as follows:

$$\tau_{k_F} \propto \frac{1}{n_i^s k_F}$$
$$\sigma \propto \frac{1}{n_i^s} \tag{15}$$

where n_i^s is the density of the short range scatterers. The charge carriers in graphene can also be scattered by vacancies and corrugations [5, 8], which form bound states called the mid-gap states.

In a graphene field effect device (Fig 4 (top)), the carrier density in graphene can be tuned by capacitively inducing charge carriers using a gate voltage. Consequently the Fermi energy and Fermi wave vector can be tuned:

$$n = \frac{\varepsilon\varepsilon_0 V_g}{ed}$$
$$E_F = \hbar v_F \sqrt{n\pi}$$
$$k_F = \sqrt{n\pi} \tag{16}$$

where V_g is the gate voltage, and ε and d are the dielectric constant and the thickness of the gate insulator, respectively. The experimentally observed gate voltage dependence of the resistivity (Fig 4 (bottom)) is a direct result of tuning the Fermi energy and scattering time. For example, the Coulomb scattering contributes resistivity which has a $1/V_g$ dependence, while the short range scatterers contribute to a gate-voltage-independent resistivity. The combined effect, summed up using Matthiessen's rule, gives the commonly observed $\mathrm{R} - V_g$ dependence [9].

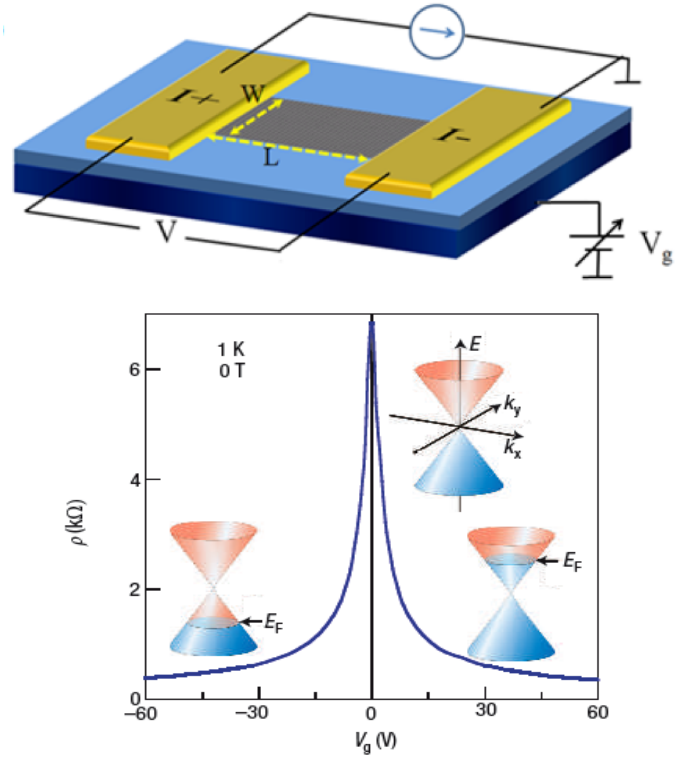

Figure 4: (top) Typical graphene Field Effect (FET) device geometry. (bottom) Gate tuning of graphene resistance by shifting the Dirac cone with respect to Fermi energy, from [10].

1.1.4 Electron-phonon interactions

Phonon emission due to electron-phonon scattering ultimately governs the intrinsic thermal conductivity of the hot electrons in graphene and thus determines the sensitivity of graphene-based bolometers. Graphene's linear electronic dispersion and 2D nature of electrons as well as phonons lead to a unique electron-phonon interaction compared to what has been found in conventional metals, semiconductors and 2DEG systems.

Phonon dispersion relation for a free-standing graphene is shown in Fig 5. In a free-standing graphene, due to three degrees of freedom there are in total, six phonon modes. Three higher energy modes correspond to optical phonons and three lower energy modes correspond to acoustic phonons. At

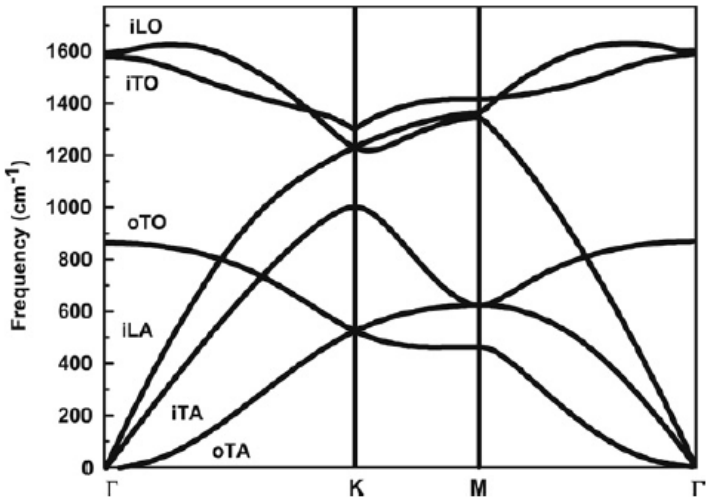

Figure 5: Phonon dispersion relation in graphene showing three acoustic phonon modes and three optical phonos mode, adapted from ref [11]. Prefix i denotes in-plane and o denotes out-of plane modes.

low temperatures, only acoustic modes, having a linear dispersion relation $\omega = sq$ participate. Here, s is the sound velocity. The out-of plane degree of freedom is suppressed when graphene sits on a substrate and hence this acoustic phonon branch, labeled oTA in Fig 5 and usually referred to as flexural phonons, does not participate. The flexural phonons have a quadratic dispersion relation which differentiates them from the in-plane acoustic phonon modes. For the purpose of devices described here, focus is limited to the longitudinal acoustic phonon (iLA) and transverse acoustic phonon (iTA) branches.

Under different experimental conditions, different phonon modes may contribute to electron-phonon scattering. The optical phonon energy (ω_0) in graphene is about 200 meV [12, 13] which is well above the operating temperature range of graphene-superconductor devices. Bolometric detection devices that are discussed here have graphene sitting on a substrate. Therefore, the out-of plane flexural phonons are not considered, which might play a role in heat conduction in the case of suspended graphene [14–16]. For graphene on a dielectric substrate, coupling to the substrate phonons must be considered as substrate optical phonons might be excited if the device op-

eration temperature is high, and therefore these excitations would contribute to cooling. Depending on the choice of substrate, this might vary. For devices fabricated on SiO_2 substrates, it has been demonstrated that the substrate remote phonon contribution to electron-phonon scattering is only evident for $T > 200$ K [17]. However, a study of suspended graphene or graphene-hBN bolometric devices should be carried out to further determine the role of substrate and electronic mobility on hot electron cooling in graphene.

At low temperatures, the most important contribution to electron-phonon scattering is from acoustic phonons in graphene. Coupling constants for transverse acoustic phonons (TA) are about an order of magnitude smaller than those for longitudinal acoustic (LA) phonons, and the TA phonons do not contribute significantly to heat conduction [18]. Discussion here is therefore limited to electron-LA phonon coupling.

Most theoretical studies of the graphene electron-phonon interaction assume that an average electronic temperature can be defined. That is, heat is distributed in the electron system via electron-electron interactions much faster than it is given off to lattice, and the occupation of energy levels is given by the Fermi function at an effective electron temperature. This assumption is justified since electron-electron interactions have a much shorter time scale than electron-phonon interactions in graphene (e.g., femto-second vs. pico-second, at room temperature [19, 20]). An average phonon temperature definition is also assumed, since phonon relaxation through energy transfer to substrate is strong enough [21]. In this case, if the average electronic temperature is different from the average phonon temperature, due to weak electron-phonon interaction, a "hot-electron" situation is created [22].

For graphene, two temperature ranges are important in studying the electron-phonon interaction: a high temperature range with $T >> T_{BG}$, also termed the equipartition (EP) regime; and a low temperature range with $T << T_{BG}$ called Bloch-Gruneisen (BG) regime. Here, T_{BG} is the Bloch-Gruneisen temperature given by,

$$k_B T_{\mathrm{BG}} = (2s/v_F)E_F \approx 0.04E_F \tag{17}$$

where s is the acoustic phonon sound velocity of 2×10^4 m/s in graphene. A carrier density of $n \sim 10^{12}$ cm^{-2} and $E_F = \hbar v_F \sqrt{n\pi} \sim 1.8 \times 10^{-20}$ J, corresponds to $T_{BG} \sim 50$ K. In the EP regime all phonon modes are nondegenerate and in the BG regime, a bosonic distribution of the phonons applies.

Electron-phonon interactions determine the limit on intrinsic carrier mobility in graphene when no impurity scattering is present. This has been

studied with measurements of the resistivity vs. temperature to determine the transport scattering time τ_{trans} [12, 13, 21]. For a clean graphene flake, its temperature dependence is calculated to be $\tau_{trans}^{-1} \sim T^4$ in the low temperature (BG) regime and $\tau_{trans}^{-1} \sim T$ in the high temperature (EP) regime [13]. The T^4 temperature dependence of the resistivity in the Bloch-Gruneisen regime has been demonstrated at extremely high carrier densities using an electrolytic gate [23]. In the low and moderate density regime relevant to the SiO_2-supported graphene devices, electron-phonon scattering gives a negligibly small contribution to the resistivity compared to other scattering mechanisms [13, 23]. It is therefore necessary to study the nature of electron-phonon scattering through the phonon thermal conductivity for graphene systems of low and moderate density.

Clean Limit

In this section, the temperature dependence of the phonon cooling power (related to the thermal conductance by $G = \frac{dP}{dT}$), without taking disorder into account, is discussed. Generally this can be calculated from the Boltzmann equation in which the occupation probability of an electron excitation with momentum $\hbar k$ in band α is given by [12, 13, 21, 24],

$$\partial_t f_k^\alpha = S_{e-ph}(f_k^\alpha) \tag{18}$$

where S is the collision integral given by,

$$S_{e-ph}(f_k^\alpha) = -\sum_{p\beta}[f_k^\alpha(1-f_p^\beta)W_{k\alpha\to p\beta} - f_p^\beta(1-f_k^\alpha)W_{p\beta\to k\alpha}] \tag{19}$$

Using Fermi's golden rule one can calculate scattering rates

$$W_{k\alpha\to p\beta} = 2\pi\sum_q w_q^{\alpha\beta}[(N_q+1)\delta_{k,p+q}\delta(\epsilon_{kp}^{\alpha\beta}-\omega_q) + N_q\delta_{k,p-q}\delta(\epsilon_{kp}^{\alpha\beta}+\omega_q)] \tag{20}$$

where N_q is the Bose distribution function of a phonon with wave vector q. The energy exchanged with the phonon heat bath is $\epsilon_{kp}^{\alpha\beta} = \epsilon_{k\alpha} - \epsilon_{p\beta}$. Here, $w_q^{\alpha\beta}$ is the squared transition matrix element that depends on the coupling mechanism between electron-phonon. In case of acoustic phonons with linear phonon dispersion $w_q = sq$ and deformation potential coupling $w_q^{\alpha\beta} = D^2q^2(1+s_{\alpha\beta}cos\theta)/4\rho_m\omega_q$, where $s_{\alpha\beta} = \pm 1$ for interband (-) and intraband (+) scattering. $\theta = \theta_p - \theta_k$ is the relative angle between incoming

and outgoing electron momenta and ρ_m is graphene's mass density. Correspondingly, the phonon cooling power is given by:

$$P = -\partial_t \sum_{k\alpha} \epsilon_{k\alpha} f_k^\alpha = -\sum_{k\alpha} \epsilon_{k\alpha} S_{ph}(f_k^\alpha) \tag{21}$$

Based on the Boltzmann equation approach, detailed calculations can be carried out and analytical solutions can be obtained at several limits through expansion of P up to leading order in s/v_F, taking advantage of the large difference between the two velocities [12, 21, 24]. It is instructive to note that interband transitions between valence and conduction bands do not contribute significantly to cooling power since they require phonon energy greater than $\hbar v_F q$, which cannot be provided by acoustic phonons having energy $\hbar\omega_q = \hbar s q$. Thus, only intraband scattering contributes significantly to phonon cooling power [25].

To obtain an analytical expression, it is necessary to evaluate the cooling power in the limit of highly doped ($\mu >> k_B T_e$) or neutral graphene ($\mu << k_B T_e$), μ being the chemical potential. In these limits, the cooling power in graphene follows the familiar power-law temperature dependence as in higher dimensional materials [21]:

$$P = A\Sigma(T_e^\delta - T_{ph}^\delta) \tag{22}$$

Here, A is the area of the graphene, Σ is the electron-phonon coupling constant and T_e is the electronic temperature. A finite lattice temperature T_{ph} is assumed. The expression for the cooling power for a highly doped and clean graphene in the low temperature regime $T << T_{BG}$ is given by [12, 13, 21, 24],

$$\begin{aligned} P &= A\Sigma(T_e^4 - T_{ph}^4) \\ \Sigma &= \frac{\pi^2 D^2 |\mu| k_B^4}{15\rho_m \hbar^5 v_F^3 s^3} \end{aligned} \tag{23}$$

Here D is the deformation potential. This T^4 power law has been observed experimentally, although values found for Σ differed by $\sim 10^2$ in these experiments [26, 27]. Behavior of the thermal conductance in the intermediate temperature regime, $T \sim T_{BG}$, is numerically calculated in reference [21].

In the highly doped, low temperature regime, the energy relaxation time temperature dependence is given as $\tau_{eph} \sim T^{-2}$, different from $\tau_{trans} \sim T^{-4}$

dependence of the transport relaxation time [21]. In the case of the neutral high temperature regime where $\mu << k_B T_e$, the temperature dependence becomes much more complicated than the low temperature limit [12, 21]. To include effects of screening, the transition matrix elements $w_q^{\alpha\beta}$, which depend on the coupling mechanism between electrons and phonons, should be divided by graphene's dielectric function and the cooling power scales as $P \sim T^6$ [18] ($\sigma \sim T^{-6}$ [28]). These effects are usually neglected, as matrix elements in graphene are believed not to arise due to the Coulomb potential [13, 24]. The experimental results show the cooling power temperature dependence calculated in the absence of screening [23, 26, 27].

Effects of disorder

In the above discussion, disorder and other scattering sources were not taken into account. In graphene devices where disorder is strong, it has been shown [18, 29] that the effects of disorder become important above and below $\mathrm{T_{BG}}$ due to different mechanisms. Due to graphene's small Fermi surface compared to usual metals, the Bloch Gruneisen temperature dictates when quantum effects become important instead of the Debye temperature. $\mathrm{T_{BG}}$ is defined by the maximum phonon momentum that can cause a transition for an electron: $q_{max} = 2k_F$. Therefore, above $\mathrm{T_{BG}}$ only a fraction of the available phonons, those with $q_{max} \leq 2k_F$, can participate in cooling (see Fig 6); the energy transferred per scattering event is less than $\mathrm{k_B T_{BG}}$. Therefore, many scattering events are required to equilibrate hot electrons with larger energy to the (cold) lattice. In this case, if disorder is taken into account, phonons with momenta larger than $2k_F$ can scatter in a three-body collision termed as supercollision [29]. This mechanism is shown to increase the phonon-cooling rate at $\mathrm{T_{ph} > T_{BG}}$ and dominates over conventional acoustic phonon cooling for temperatures $\mathrm{T_{ph} > T^\star}$, where $\mathrm{T_{ph}}$ is the phonon temperature and $T^\star = (\frac{\pi}{6\zeta(3)} k_F l)^{1/2} T_{BG}$ [29]. It was shown by Song et al. that supercollision cooling power per area is given by [29],

$$\begin{aligned} P &= \alpha(T_e^3 - T_{ph}^3) \\ \alpha &= 9.62 \frac{g^2 N^2(E_F) k_B^3}{\hbar k_F l} \end{aligned} \tag{24}$$

Here, $N(E_F)$ is the density of states per spin and per valley degeneracy, l is the mean free path and $g = D/\sqrt{(2\rho s^2)}$ is the deformation potential coupling

factor. The calculation is carried out using Fermi's golden rule listed above by considering impurity scattering before and/or after phonon scattering. This mechanism was experimentally verified using Johnson noise technique to measure the electron temperature [30]. In this experiment by Betz et al., T_{BG} can be tuned above and below T_{ph} by tuning the Fermi energy and clean limit, low-temperature behavior of the power emitted into phonons $P \propto T^4$ and supercollision $P \propto T^3$ can be observed in the same device. Supercollisions are most clearly observed near the charge neutrality point which tunes T_{BG} to a small value of a few Kelvin. Experiments investigating cooling rates with photocurrent generation have also confirmed the supercollision regime [31].

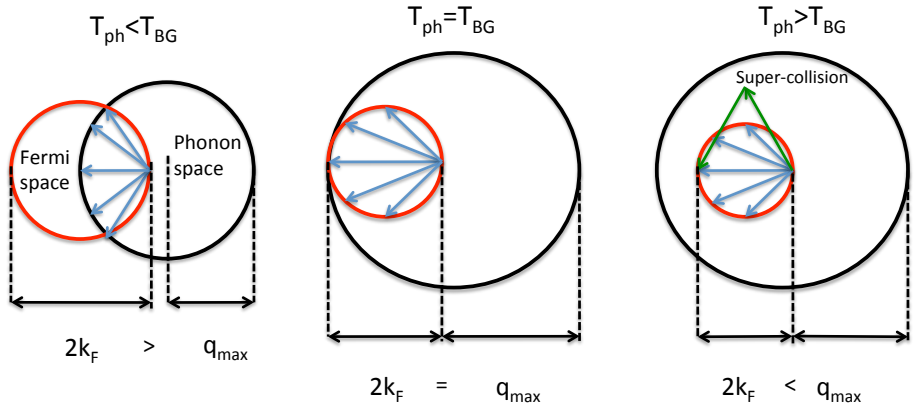

Figure 6: Supercollison mechanism. Available allowed phonon momentum space for electron scattering expands due to the presence of disorder at $T > T_{BG}$.

In the case of strong disorder (short mean free path), it is possible that the phonon wavelength becomes longer than electronic mean free path. A new temperature scale then comes into picture below which disorder effects become important [18]

$$k_B T_{dis} = hs/l \tag{25}$$

If the condition $k_F l >> 1$ is satisfied, T_{dis} is necessarily well below T_{BG} [18]. In this case of high impurity level, scattering calculations based on the golden rule are not useful and the Keldysh formalism is employed to obtain cooling power per area for deformation coupling given as,

$$P = \frac{2\zeta(3)}{\pi^2} D^2 \frac{E_F}{\hbar^4 \rho_m v_F^3 s^2 l} (k_B T)^3 \tag{26}$$

In a comprehensive study by Chen et al. [18], cooling power due to electron-phonon scattering due to different coupling mechanisms in the presence of disorder is calculated. Effects of disorder were included to show that when screening is considered, the deformation coupling-induced scattering rate is reduced. It is noted that the couplings for the unscreened deformation potential are largest and other effects remain less important. Below some of the main results for the phonon cooling power temperature dependence discussed so far in different regimes are summarized.

Clean limit $T < T_{BG}$	Disordered limit $T > T_{BG}$	Disordered limit $T < T_{dis} < T_{BG}$
$\Sigma(T_e^4 - T_{ph}^4)$	$\alpha(T_e^3 - T_{ph}^3)$	$\beta(T_e^3 - T_{ph}^3)$
$\Sigma = \frac{\pi^2 D^2 \lvert\mu\rvert k_B^4}{15\rho_m \hbar^5 v_F^3 s^3}$	$\alpha = 9.62\frac{g^2 N^2(E_F) k_B^3}{\hbar k_F l}$	$\beta = \frac{2\zeta(3)}{\pi^2} D^2 \frac{E_F}{\hbar^4 \rho_m v_F^3 s^2 l} {k_B}^3$

Table 1: Summary of phonon cooling power in different temperature and disorder regimes

1.2 Bilayer graphene

Bilayer graphene is a two atomic layer thick sheet of graphite. Thus, it is two dimensional in nature, much like a single layer graphene sheet, although it has a significantly different band structure. Here, the electronic band structure of bilayer graphene is presented along with a brief description of electron-phonon interactions in this system.

1.2.1 Electronic properties

Unlike single layer, a derivation of the bilayer tight binding band structure is not presented here since it becomes lengthy when more layers are involved, increasing the hamiltonian matrix dimensions. However, there are comprehensive reviews available which present this derivation in detail [32]. In this section, only the final result of this derivation is presented.

Bilayer graphene has a four atom unit cell, with two atoms in bottom and two in top layer. In a Bernal stacked (AB) bilayer graphene, B atom sits directly above an A atom in the bottom layer. For future discussion of results, only the case of Bernal stacked bilayer graphene is considered, most commonly found in exfoliated flakes.

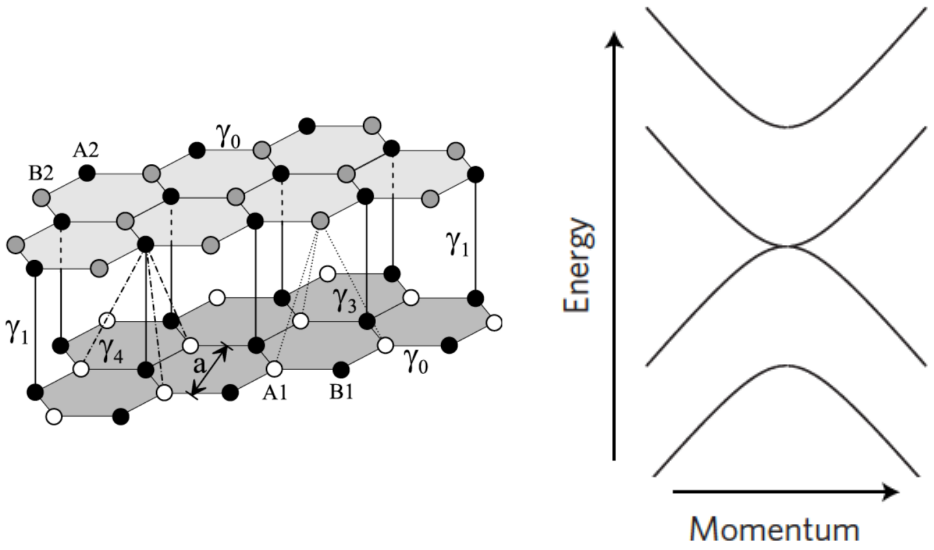

Figure 7: (left) Bilayer lattice structure, from McCann et al. [32] (right) Low energy dispersion relation of bilayer graphene [33].

Due to a four atom unit cell, bilayer graphene tight binding hamiltonian is a 4×4 matrix. In Slonczewski-Weiss-McClure (SWM) notation γ_1 (see Fig 7) denotes the vertical interlayer hopping energy between A and B atoms and γ_0 denotes in-plane nearest-neighbor hopping energy and is analogous to the nearest neighbor coupling t in a single layer graphene. γ_3 and γ_4 represent the interlayer skewed coupling energies. γ_2, appearing in the SWM calculations of bulk graphite, is absent in bilayer graphene. The full-tight binding band structure calculations reveal four bands in bilayer graphene. Two low-energy bands touch at the K and K' points of Brillouin zone and the other pair of conduction and valence band is separated by an energy gap of the order of interlayer coupling γ_1. Although a low energy two-band structure is most commonly used for experimentally relevant situations. In pristine bilayer graphene, as in the case of single layer, Fermi energy lies at the point where valence and conduction band meet. In the vicinity of K and K' points, small momentum dispersion relation of bilayer graphene is given as,

$$\varepsilon \approx p^2/2m \tag{27}$$

where $m = \gamma_1/2{v_F}^2$ and $v_F = \sqrt{3}a\gamma_0/2\hbar$ is defined analogous to single layer

graphene. At large momenta the bands become linear $\varepsilon \approx vp$. It is also possible to introduce a band gap in bilayer graphene by breaking the interlayer symmetry through applying external gate voltages. However, discussion of a gapped bilayer graphene system is not relevant in the electron-phonon coupling studied here pertaining to intrinsic bilayer graphene.

Based on this quadratic dispersion relation in a bilayer graphene, the density of states is given as,

$$N_{BLG}(E) = \frac{\gamma_1}{\pi\hbar^2 v_F^2} \tag{28}$$

It can be seen that the DOS in bilayer graphene is independent of the energy, contrary to that in single layer graphene which has a linear energy dependent DOS. At low temperatures, electronic heat capacity can be calculated from Eq 9 and the bilayer DOS. It is given as,

$$C_{e-BLG}(E) = \frac{\pi^2}{3} N_{BLG}(E) k_B^2 T \tag{29}$$

The heat capacity in bilayer graphene is energy independent as well. It can be noted that at a given temperature for a given chemical potential and flake area, bilayer graphene's electronic heat capacity is higher than that of its single layer counterpart.

1.2.2 Electron-phonon interactions

The use of bilayer graphene may be advantageous for bolometric detection and to determine its feasibility, it is necessary to understand the electron-phonon interactions in this system. As explained above, bilayer graphene differs from monolayer graphene by having an approximately parabolic band structure at low energies. The cooling power in this case, below the Bloch Gruneisen temperature of bilayer graphene $k_B T_{BG,BLG} = 2(s/v_F)\sqrt{\gamma_1|\mu|}$ (γ_1 is the SWM band parameter), also scales as T^4 [21]. The coupling parameter Σ in this case is given as [21]:

$$\begin{aligned} P &= \Sigma_{BLG}(T_e^4 - T_{ph}^4) \\ \Sigma_{BLG} &= \frac{\pi^2 D^2 \gamma_1 k_B^4}{60\rho_m \hbar^5 v_F^3 s^3} \sqrt{\frac{\gamma_1}{|\mu|}} \end{aligned} \tag{30}$$

Eq 30 is derived without taking disorder and reduced electronic mean free path into account. It further ignores screening effects as well. Thus, it would be instructive to compare the observed temperature dependence of cooling power in bilayer graphene with the predicted form in Eq 30.

2 Introduction to Bolometers

Bolometer is a thermal detector which detects electromagnetic radiation through a radiation absorber with a temperature dependent electrical quantity. In this thesis, two different subject matters of graphene and superconducting bolometers are combined with a goal to advance the knowledge in each field. In this combination, the field of superconducting bolometers has a long and rich history [34] while graphene is a more recently isolated two dimensional sheet of graphite [35]. Implementation of graphene in a bolometer device provides an ideal platform to study its fundamental physical properties such as electron-phonon interactions. In this chapter, basics of a bolometer device principle are outlined.

2.1 Operating principle of a bolometer

Bolometer devices are a subject of active research since more than a decade now, with design focus continuously shifting with technological advances. First demonstration of a bolometer operation was by an american astronomer Samuel Langley [36] in 1878, used for solar irradiance observation. The simple design of Langley's bolometer has evolved with the advances in technology. However, the basic principle of bolometer operation is still very much like the very first prototype, outlined below.

A most basic bolometer device schematic is shown in Fig 8. When radiation is applied, the absorber converts the applied radiation and goes through a change in temperature, which can be detected by the thermometer. The heated absorber then cools down via heat transfer through a heat-sink. The thermal link between the absorber and the heat-sink determines the ultimate bottleneck in cooling and in turn, the sensitivity of the device operation. The term bolometer which is a radiation power detector is often used interchangeably with a calorimeter, which is a photon detector and counts the number of photons in incoming radiation. In the photon detection regime, when a photon pulse of energy E is absorbed, the temperature increase in the absorber is given by,

$$\Delta T = \frac{E}{C} \tag{31}$$

where C is the heat capacity of the absorber-thermometer assembly.

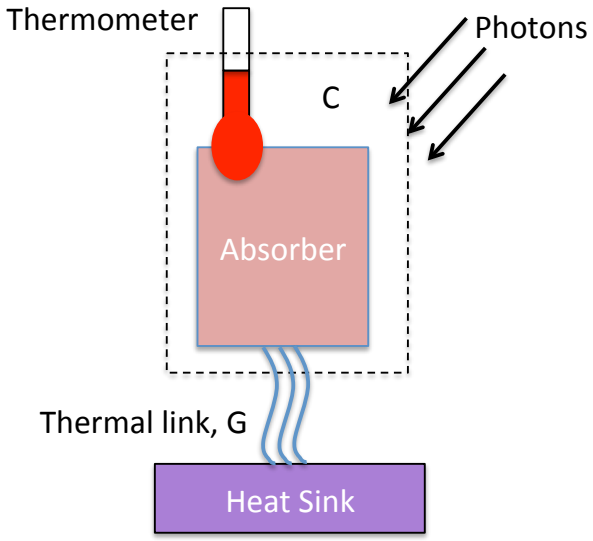

Figure 8: Schematic diagram of a bolometer device operations, outlining basic elements.

For a device operating at a bath temperature T_{t0}, if

$$\Delta T << T_{t0} \tag{32}$$

then the device is said to be operating in the linear regime. For operation as a power detector, when a power of amount P is absorbed in the device, the steady-state temperature increase is calculated by,

$$\Delta T = \frac{\Delta P}{G} \tag{33}$$

where, G is the thermal conductance of the thermal link between the absorber and the heat sink. And a similar constraint for the linear operation, as described in Eq 32 applies.

2.2 Bolometer device performance parameters

Depending on the targeted application, optimization of a particular bolometer parameter may be required. Since there is an inherent trade-off between some of the parameters, a general optimization scheme for bolometer as a power-detector is discussed in this thesis. Two most important parameters

of a bolometer device are the thermal conductance (G) of the thermal link between the absorber and the heat sink and the heat capacity (C) of the absorber. Sensitivity of these devices is measured as the Noise Equivalent Power (NEP) in units of $W/Hz^{1/2}$. This is defined as the noise measured to achieve a unity signal to noise ratio with a 1 Hz measurement bandwidth. The intrinsic sensitivity of a bolometer is characterized by the thermal noise equivalent power (NEP_{th}), which is the noise due to thermal fluctuations in the device. This is related to the thermal conductance (G) of the device by,

$$NEP_{th} = \sqrt{4k_B T^2 G} \tag{34}$$

Typically, the intrinsic thermal noise equivalent power is not the only contributor limiting the sensitivity of a bolometer and depending on the temperature readout method. The actual noise equivalent power can be higher. A list of some of the other limiting noise sources is given in ref [37]. The total NEP is then given by [38],

$$NEP_{total} = \left(NEP_{th}^2 + NEP_{readout}^2\right)^{1/2} \tag{35}$$

However, since the ultimate sensitivity is limited by thermal fluctuations of the device, this is the primary figure of merit used for characterization purposes in this thesis.

For an energy detector, the energy resolving power (R) is another figure of merit and it is given by,

$$R = \frac{E}{\delta E} \tag{36}$$

where δE is the full-width-half-max (FWHM) energy width which is limited by the intrinsic energy resolution and the resolution of the readout mechanism. This is related to the *rms* value as $\delta E = 2.35\delta E_{rms}$. The intrinsic energy resolution and the total energy width are given as follows,

$$\begin{aligned} \delta E_{total} &= \left(\delta E_{int}^2 + \delta E_{readout}^2\right)^{1/2} \\ \delta E_{int}(FWHM) &= 2.35\sqrt{k_B T^2 C} \end{aligned} \tag{37}$$

The time constant of the device operation is given as,

$$\tau = \frac{C}{G} \tag{38}$$

It can be seen from Eq 34 and 38 that achieving a high sensitivity (low NEP) in a bolometer requires a device design with low G, which would invariably make it slow. In order to achieve speed and sensitivity simultaneously, it would be necessary to choose an absorber with a small heat capacity. Typically, this is achieved by making the absorber volume as small as possible.

2.3 Bolometer Applications

Bolometers are mainly employed to detect thermal radiation in the THz/sub - mm range of the electromagnetic spectrum. A bolometer can either be used for a cooled or uncooled operation depending on the specific requirements. It can also be used in a coherent or non-coherent detection scheme. Coherent detection mode preserves the information about radiation energy as well as the spectral information. Non-coherent detection only allows for power detection. However, since amplitude and phase are non-commuting variables, coherent detectors have lower efficiency than their power detector counterparts, limited by the quantum efficiency of a detector.

2.3.1 Room temperature bolometers

Room temperature devices have mainly been developed for thermal imaging in industrial and security applications, such as military operations, night vision, airport security, equipment fault-tolerance etc. Microbolometers, as they are called, are now largely commercialized and use an oxide with a high temperature coefficient of resistance (e.g. vanadium oxide) as a sensing element [39]. These commercial microbolometers operate at room temperature and suffer from low sensitivities. Their spectral response is also limited to $8 - 14$ μm wavelength range. Besides this, there are many other designs developed which use different principles to detect temperature of a body. These include, Golay cells, pyroelectric devices, cantilever based devices etc. [40]. Golay cells use the Golay principle [41] of thermal expansion of a gas when it is heated up. They exhibit higher sensitivities than the commercial microbolometers.

2.3.2 Cryogenic bolometers

Sensitivities needed for astronomical applications require cryogenic operation of a bolometer device. Half of the total luminosity of the cosmic

microwave background and 98% of the photons emitted since big bang fall into the sub-mm range of the electromagnetic spectrum [42]. Spectral information in the sub-mm wavelength can give information about the molecular species present in a celestial body. Along with the doppler shift, it can also point to what kind of object is located in which region of the space. Gas composition and temperature of gas clouds and debris disks could yield information about the formation and evolution of galaxies and the universe itself.

Depending on the far infrared absorption of the atmosphere in the frequency region of interest, these cooled bolometer devices are employed in either ground-based or space-based telescopes. It is a considerable challenge to develop cryogenic bolometers for such experiments which have background limited sensitivities. Which means that the measurements are only limited by the statistical noise in arrival of photons. And this can be very low, for example in the case of cosmic microwave background radiation for $\nu > 1$ THz, it can be as low as $\mathrm{NEP_{ph}} = h\nu\sqrt{2N_{ph}} \sim 10^{-20}$ W/Hz$^{1/2}$ [43]. One such current state of the art detector which approaches this limit includes a transition edge nano-bolometer described in ref [43]. A transition edge sensor (TES) employs a superconducting sensing element and can detect very small temperature changes when it is carefully biased in the superconducting transition region. In this experiment employing superconducting Ti nano-bridge, a sensitivity of $\mathrm{NEP_{th}} < 10^{-20}$ W/Hz$^{1/2}$ at T = 65 mK for $\nu \leq 600$ GHz is achieved by biasing the Ti nano bridge near its superconducting transition. To achieve this low value, thermal isolation by using higher gapped (than Ti) superconducting contacts is achieved. This is done without sacrificing detector speed by reducing the dimensions of the nano-bridge to 5×10^{-3} μm^3.

In physical chemistry, fast bolometers are employed to study time domain spectroscopy of molecular dynamics of ns scale. THz imaging can also be used to biological systems as well as to study electrical characteristics of a solid-state system [44]. Other examples of THz detectors include kinetic inductance detectors [45], superconducting nano-wire single photon detectors [46], SIS mixers [34] etc.

3 Graphene-based Bolometers

3.1 Advantages of a graphene absorber

In the standard bolometer design given in chapter 2, graphene fits in the role of an absorber. There are several advantages in utilizing graphene absorber for bolometer applications. They are listed below.

3.1.1 Electronic heat capacity

Graphene, as a single atomic layer of carbon, has ultra-small volume. At the same time, electrons in graphene are described by the Dirac-Weyl Hamiltonian and hence follow a linear energy dispersion. This leads to a low electron density of states which depends linearly on energy in graphene. As a result of this small volume and low density of states, a very small electronic heat capacity can be achieved in graphene. This allows a large intrinsic energy resolving power (R), defined in Eq 36 for single photon detection and a fast device response (small τ). Calculations show that almost two orders of magnitude lower heat capacity ($C_e \sim 10^{-21}$ J/K at $T = 1$ K [3]) can be achieved in graphene than the Ti nano-bridge bolometer described in [43].

3.1.2 Weak electron-phonon coupling

Another advantage is the weak electron-phonon interaction in graphene at low temperatures, as a result of the small Fermi surface. This is seen in the transport measurements where graphene's resistance depends extremely weakly on temperature and a high mobility can be achieved at low temperatures [17, 47]. This means that at low temperatures, a small radiation power can heat up the electrons in graphene above the lattice temperature. And the electron and phonon subsystems exist at different effective temperatures. This is called the "hot-electron" effect and bolometer devices which utilize this effect to detect electromagnetic radiation are called hot electron bolometers (HEB). Weak electron-phonon coupling in graphene also allows a very small thermal conductance which is the ultimate hot electron cooling bottleneck when contribution from all other thermal channels has been suppressed. Therefore a high intrinsic sensitivity ($\mathrm{NEP_{th}}$) can be achieved in graphene-based bolometers.

3.1.3 Impedance matching

As a 2D material, due to a large contact area-graphene allows relatively low device resistance compared to one-dimensional nanomaterials (e.g., carbon nanotubes [48]). Since a graphene bolometer device structure is a few micrometers in size, an antenna is needed to couple the electromagnetic radiation with the graphene absorber. For a high coupling efficiency, it is necessary to have a close impedance match between the device and the antenna network. This impedance is either 50 Ω in case of an amplifier or 100 Ω for a planar antenna. The low and gate-tunable resistance in graphene makes it possible to integrate the devices with a planar antenna with high coupling efficiency.

3.2 Challenges of employing a graphene absorber

Graphene is indeed a very attractive material for detector applications for the reasons listed above. However, there are technical challenges in designing a bolometer that can take a full advantage of these properties.

3.2.1 Weak temperature dependence of resistance

In graphene, the electron-phonon coupling is predicted to be extremely weak at low temperatures. As mentioned above, this reduces the thermal conductance of the device and helps achieve higher sensitivities. But due to this weak-electron phonon scattering, resistance of a graphene flake does not show significant temperature dependence [17, 47]. This makes it challenging to measure the electron temperature change due to incoming radiation power. An alternate electrical quantity needs to be identified which has a sizable response to the temperature change. A scheme of graphene-superconductor junctions is described in chapter 4, which can provide a measurable temperature dependent quantity.

3.2.2 Efficiency vs. sensitivity

The next challenge is to confine the hot electrons within the graphene channel and minimize the thermal conductance to that due to electron-phonon coupling to achieve a high sensitivity bolometer. Doing so would allow the study of electron-phonon interactions in graphene, which is otherwise difficult due to a weakly temperature dependent resistance. As ex-

plained below, having a large contact resistance blocks the hot electrons from diffusing out of the electrical contacts. However, for high efficiencies, one must also design the devices to have low microwave impedance, in order to match with the antenna and external microwave readout circuit. Having a high contact resistance in order to minimize the thermal conductance would not therefore, allow impedance matching with the antenna. A trade-off exists between achieving a high sensitivity and a high efficiency device, which should be addressed in a graphene bolometer design. The design of graphene-superconductor junctions is demonstrated to include a solution to this problem, described in chapter 4.

3.3 Thermal conductance in a graphene device

For a substrate-supported graphene device, the graphene lattice, the substrate, electrical contacts and the environment can be identified as major heat sinks. Thus, four thermal channels shown in Fig 9 exist for hot electron cooling. The total thermal conductance (G) is the sum of all these contributions.

$$G = G_{e-ph} + G_{WF} + G_{photon} + G_{substrate} \tag{39}$$

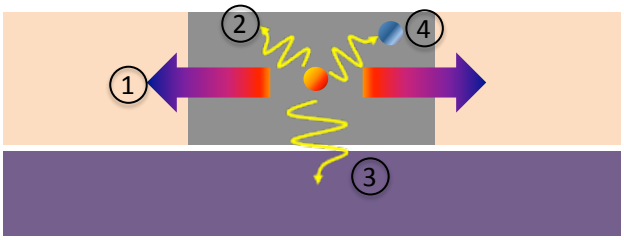

Figure 9: Four main hot electron cooling pathways are identified in a substrate supported graphene device. Orange dot represents a hot electron and the blue dot represents a phonon.

1. **Diffusion cooling:** In a cold graphene device when radiation is applied, electrons within the graphene channel heat up. However, electrical contacts remain cold and act as heat reservoirs. Hot electrons in graphene can thus diffuse through the electrical contacts and cool

down. Thermal conductance of this channel is given by the Widemann-Franz law and is related to the electrical resistance in the following way:

$$G_{WF} = \frac{\alpha \mathcal{L} T}{R} \tag{40}$$

Here, α is a geometrical factor based on the heating profile in the channel. For example, in one-dimensional Joule heating of a conductor with two electrical terminals, $\alpha = 12$ [49]. And in case of an oxide tunnel barrier at the two contacts, where heat flows out of the two contact resistors (with a contact resistance of $R/2$ each) in parallel, $\alpha = 4$ [50]. $\mathcal{L} = 2.44 \times 10^{-8}$ WΩK^{-2} is the Lorentz number. From the above equation, it is seen that $G_{WF} \propto 1/R$. Thus, having a large contact resistance would reduce the out-diffusion contribution to the total thermal conductance. However, in doing so, the advantage of impedance matching ability in graphene would be lost. It then seems that a sensitive device would become inefficient, as mentioned above.

2. **Black-body radiation:** Hot electrons can emit a photon and couple to the environment to cool down [51]. Thermal conductance due to this channel is proportional to the measurement bandwidth and in the case when noise measurements are used to read out electronic temperature, it is the bandwidth of an amplifier.

$$G_{photon} = k_B B \tag{41}$$

3. **Substrate cooling:** In case of substrate-supported graphene bolometers, remote phonons in the substrate can activate and provide a dominant cooling mechanism. In case of a SiO_2 substrate, transport evidence shows that the remote optical phonons are suppressed below T = 200 K [17].

4. **Electron-phonon interactions:** If an absorber is completely thermally isolated, so that above mentioned cooling channels have suppressed contributions, then the hot electrons cool down via interactions with the lattice. These electron-phonon interactions provide a cooling power which has a polynomial dependence on the temperature.

$$P = A\Sigma(T_e^{\delta} - T_{ph}^{\delta}) \tag{42}$$

Here Σ is called the electron-phonon coupling constant and A is the device area. The value of δ is determined by the dimensions of the device, range of the device operation temperature, disorder induced electron scattering, electronic screening and phonon coupling mechanism. For example, in a metallic thin film $\delta = 5$ is observed below the Debye temperature [22]. Thermal conductance due to electron-phonon interactions is given as:

$$G = \frac{dP}{dT}$$
$$\implies G_{e-ph} = A\delta\Sigma T_e^{\delta-1} \tag{43}$$

Thus, to design a graphene-based bolometer which provides optimum sensitivity, a fast response and high efficiency, it is necessary to determine the various parameters described above and their contribution. In subsequent chapters the concept of graphene-superconductor-based bolometers is described along with its implementation. It is demonstrated that this design can be successfully used to study the electron-phonon coupling in graphene and it is argued that it is capable of achieving a sensitive and fast bolometer device.

4 Graphene-Superconductor Junctions

Graphene-superconductor junctions have been fabricated and measured using a variety of superconducting materials with transparent contacts [52–57] and with a tunnel barrier [58, 59], to study different junction dynamics. Here, the aim is to use this design to build a bolometric device and to study electron-phonon cooling in graphene through its implementation. As mentioned in chapter 3, due to an extremely weak temperature dependence of graphene's resistance, it is necessary to design a graphene bolometer device which has an electrical quantity with a sizable temperature dependence. The approach described here towards the solution of this problem is through using graphene-superconductor junctions design. This is not the only approach to achieve a temperature dependence however, and there are other proposed schemes of implementing a graphene-based bolometer. These include a gate-tunable gapped bilayer graphene [60], Johnson noise measurement of graphene's electronic temperature [27, 61] and temperature-dependent supercurrent in a graphene based Josephson junction [54]. Details of the graphene-superconductor junction design and its advantages are explained below in more detail.

4.1 Graphene-superconductor junctions design scheme

In this thesis, two types of device geometries are explored (See Fig 10). Both include employing superconducting contacts on graphene, to create a planar graphene-superconductor junction. Here, in a two-terminal geometry the superconducting contacts act as source and drain terminals. However, the type of interface between graphene and the superconductor is different in both. One approach is to fabricate highly transparent contacts on graphene to implement a Superconductor(S) - Normal metal(N) - Superconductor(S) Josephson junction, with graphene as the normal metal. The other involves creating a tunnel barrier between graphene and the superconductor using a sandwiched oxide layer, to implement a Superconductor(S) - Insulator(I) - Normal metal(N) - Insulator(I) - Superconductor(S) structure, referred to as SIGIS structure with graphene as a normal metal. Both of these designs are explored to achieve three goals:

1. To provide a sizable temperature dependent electrical quantity.

2. To block hot electrons from cooling through the contacts so as to allow observation of cooling via electron-phonon interactions.

3. To achieve a device with an impedance that matches with the antenna circuitry.

Below it is outlined how both the design can achieve this.

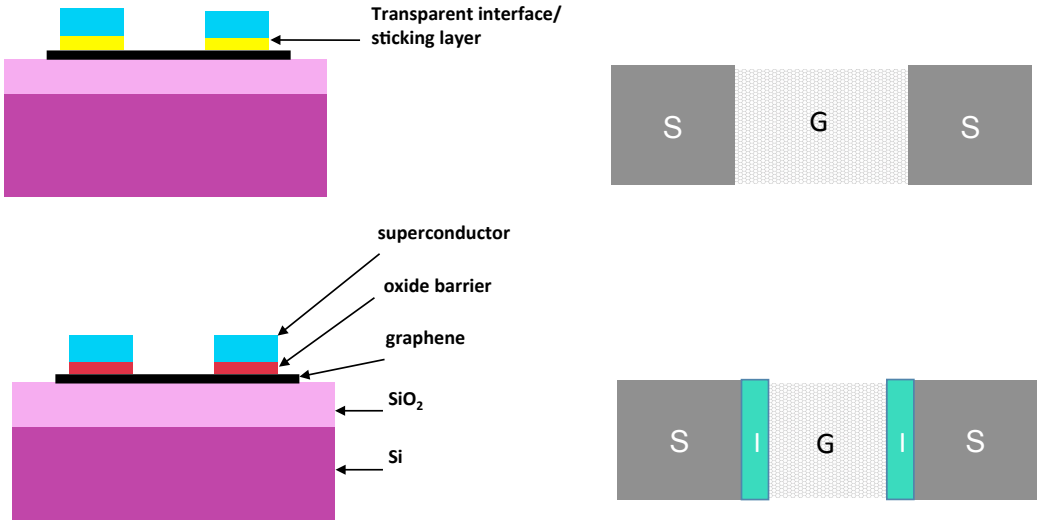

Figure 10: Top panel shows graphene-superconductor junction with transparent contacts geometry. Bottom panel shows graphene-superconductor tunnel junction geometry. The difference in the contact fabrication is the sandwiched tunnel oxide in the bottom panel instead of the transparent sticking layer in the top panel.

4.1.1 Graphene-superconductor tunnel junction (STJ)

Schematics of a graphene-superconductor junction with a sandwiched insulating oxide barrier is shown in Fig 10 bottom panel. A cartoon energy diagram of this geometry is shown in Fig 11. The resistance measured across this junction depends on the tunneling probability of the thermally excited charge carriers in graphene. At low temperatures and low bias, charge carriers in graphene do not have sufficient energy to tunnel through the oxide barrier into a superconductor. Thus, for a current-biased junction, resistance measured for junction voltage $V_b < 2\Delta$ is temperature-dependent. Here Δ is the

BCS superconducting energy gap [62]. The peak zero junction-bias-voltage resistance can thus be used as a thermometer. If this zero-bias resistance responds in the same way to applied radiation, as it does to the temperature increase then the device response is said to be bolometric.

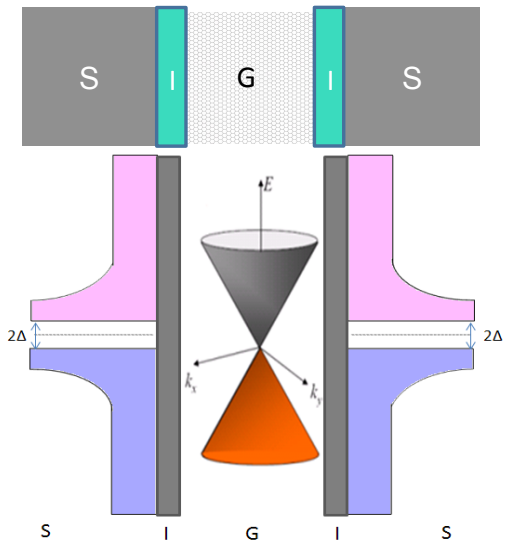

Figure 11: Cartoon energy diagram of a Superconductor(S) - Insulator(I) - Graphene(G) - Insulator(I) -Superconductor(S) device structure. The junction has a temperature dependent resistance and it also prevents hot electrons in graphene from leaking out of the superconducting contacts.

In this device scheme, due to the inability of charge carriers in graphene to tunnel across an insulating barrier into the superconducting gap, hot-electrons created by applying radiation are confined into the graphene absorber. Thus, the out-diffusion of hot electrons through contacts is reduced significantly and their cooling via phonon interactions can be studied. The diffusion thermal conductance given by the Wiedemann-Franz law, is inversely proportional to the device resistance:

$$G_{WF}(T) \propto \frac{T}{R(T)} \tag{44}$$

The tunnel resistance of this device structure is quite high, usually designed to be within a range of few kΩ to few MΩ. In an ideal SIGIS device

structure, this resistance is expected to increase exponentially as temperatures decrease. Thus, at low temperatures, below T < 1 K, where the phonon thermal conductance decreases, so does the out-diffusion thermal conductance due an increased contact resistance, still maintaining electron-phonon interactions as the dominant cooling mechanism. However, creating a high resistance device in order to keep G_{WF} contribution low, results in a loss of impedance match with the antenna network which requires the device resistance to be $\sim 50\ \Omega$. It seems that achieving one would sacrifice the other. However, a solution exists, as described below.

If an oxide with a high dielectric constant is used as the tunnel barrier then a large oxide capacitance exists between graphene and the superconducting contacts. This capacitive channel is in parallel with the high tunnel junction resistance. The graphene resistance is related to the sheet resistivity (ρ_s) by,

$$R = \frac{\rho_s}{W/L} \tag{45}$$

If the graphene channel aspect ratio (W/L) is so designed that it gives a very small resistive contribution to the total device impedance then at DC excitation, the tunnel resistance dominates the device impedance. However, at high frequencies the large oxide capacitance enters the picture and provides a short to the large tunnel resistance and only the small graphene channel resistance dominates the total device impedance. This way, even though the DC SIGIS junction resistance is of the order of few kilo-ohms its high frequency impedance can be tuned to a value of few tens of ohms. Details of this model describing contacts are given in chapter 5.

In summary, the SIGIS device structure can be designed to fulfill all the requirements listed above to build an efficient and sensitive graphene bolometer.

4.1.2 Graphene-superconductor junctions with transparent contacts

In this device geometry the tunnel oxide sandwiched between graphene and the superconductor is replaced by an adhesion layer, such as Ti or Pd, to form transparent contacts. Below the superconducting transition temperature, graphene becomes proximitized and if the graphene channel length is short compared to the superconducting coherence length ξ, a supercurrent

flows through the junction. A sustained supercurrent in these junctions indicates high transparency of the contacts. In this case, when the junction bias is less than the superconducting gap, $V_b < 2\Delta$, if an electron tries to enter the superconductor from graphene it is reflected back as a hole at the boundary [63]. The missing charge of $2e$ enters the superconductor as a cooper pair. This process, known as the Andreev reflection, conserves energy but generally does not conserve momentum and the hole reflected back is through a retro-reflection. However, in graphene, the Fermi energy is gate-tunable and if it is tuned near zero then the incident electron and the reflected hole come from conduction band and valence band respectively. This is unlike the Andreev process in metals where incident electron and reflected hole, both come from the conduction band. Due to this reason, specular Andreev reflection can take place [64] in graphene. However, this prediction is only true when the incident electron excitation energy (ε) is within the superconducting gap, $\varepsilon < \Delta$. In case of substrate supported graphene, it is not possible to tune the Fermi energy close enough to CNP so that this condition of specular Andreev reflection may be satisfied. To allow observation of specular Andreev reflection and the predicted diffusive dynamics of a graphene SNS junction at the CNP [64], it is necessary to approach the ballistic limit in suspended graphene Josephson junctions [65]. In substrate-supported graphene, as is the case here, retro-Andreev reflections still take place, converting an incident electron isothermally into a reflected hole. Thus, it prevents the heat energy from escaping out of the graphene channel, lowering out-diffusion contribution to the thermal conductance G_{WF}.

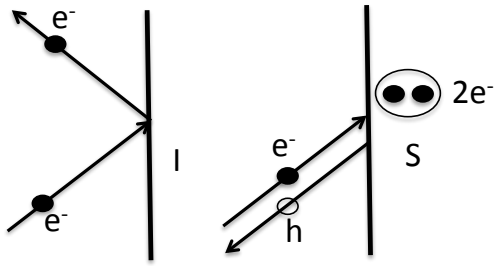

Figure 12: Difference between normal reflection of an electron at an insulator boundary and Andreev reflection at a superconductor boundary.

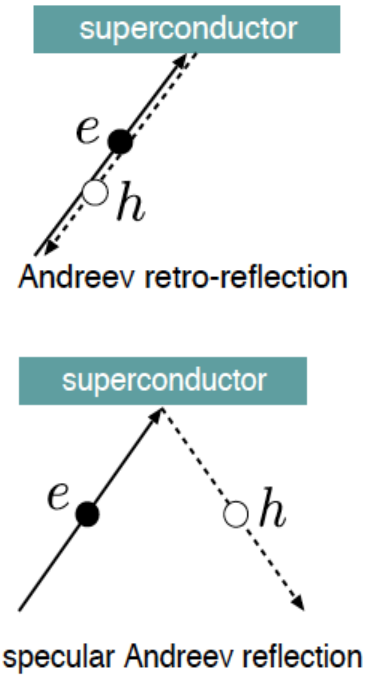

Figure 13: Andreev reflections at a normal-metal (N)/superconductor (S) boundary. In case of graphene as a normal metal, retro-Andreev reflections are predicted to become specular.

In this design, due to the supercurrent flowing across the proximitized graphene channel, there is no voltage drop and hence, the junction resistance cannot be calibrated as a thermometer. To then measure a temperature-dependent resistance in such a junction, supercurrent needs to be suppressed while preserving the advantage of suppressed hot electron out-diffusion due to Andreev reflections. A design of long junction in which the graphene channel is kept longer than the superconducting coherence length ($L >> \xi$) is proposed here to achieve this. The supercurrent formation can be eliminated for this design [62]. When radiation is applied, part of this long graphene channel heats up and becomes 'normal' (Fig 14). This 'normal' region resistance depends on the temperature increase induced through the applied radiation. Thus, in this design of a long SGS junction, temperature change can be detected through the temperature dependent junction resistance and diffusion of hot electrons through contacts is blocked through Andreev reflections at the SN boundary. To fabricate SGS junctions, a very high contact

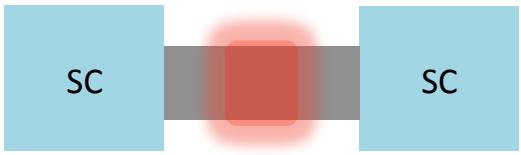

Figure 14: Cartoon diagram of a long graphene STJ geometry. Due to the long length of the channel, the entire graphene doesn't proximitize and a hot-spot is created. This is in order to avoid calibration complications from supercurrent formation.

transparency is needed which gives an extremely low contact resistance (few tens of ohms). Thus, here too, like the SIGIS case, impedance matching with the antenna network can be achieved by adjusting the aspect ratio of the graphene channel.

From the above discussion, it is seen that by using two different configurations of graphene-superconductor junctions, a highly sensitive bolometer device can be realized in each case. The difference in these two geometries lies in the contact fabrication. These are realized by carefully controlling several experimental parameters. To characterize in which regime (SGS or SIGIS) a given device lies, it is compared with theoretical simulations. A theory known as the BTK theory differentiates two regimes and its predictions are briefly mentioned below.

4.2 The Blonder-Tinkham-Klapwijk theory of SN junctions

The characteristics of graphene-superconductor junctions can vary significantly depending on the contacts fabrication procedures used. Some of the factors affecting the nature of these junctions are the level of vacuum in the metal deposition chamber, method of titanium oxidation, thickness of titanium oxide, thickness of palladium buffer layer etc. Since both transparent and tunnel superconductor (S) contacts to graphene (N) are studied here, it is useful to describe the contact transparency using a theory of S-N interface developed by Blonder, Tinkham and Klapwijk, known as the BTK theory [66]. The theory calculates current flowing through a normal metal-superconductor (NS) junction. Since in the bolometric devices studied here, there are two such junctions in series (SNS) (with graphene as a normal

metal) the current would be twice as that calculated in ref [66]. This current is given as:

$$I_{SNS} = 2I_{NS} = 4N(0)ev_F\mathcal{A}\int_{-\infty}^{\infty}[f_0(E-eV) - f_0(E)][1 + A(E) - B(E)]dE \tag{46}$$

Here, N(0) is the density of states per spin at the Fermi energy and in graphene's case, it is derived based on Eq 8. $\mathcal{A}$ is the cross-sectional area of the weak-link. $f_0(E)$ is the Fermi distribution function.

A and B are reflection coefficients for Andreev and ordinary reflections respectively. In a ballistic graphene-superconductor junction, Andreev reflections are predicted to be specular rather than the usual case of retro-reflections [2]. However, since the devices described here are fabricated using graphene on a substrate, they are diffusive and would not show specular Andreev reflections. For $E < \Delta$ (Δ is the superconducting energy gap) reflection coefficients A and B are given as,

$$\begin{aligned} A(E) &= \frac{\Delta^2}{E^2 + (\Delta^2 - E^2)(1+2Z^2)^2} \\ B(E) &= 1 - A(E) \end{aligned} \tag{47}$$

Here, $2ZE_F/k_F$ is the barrier strength of a δ-function potential barrier. Z is called the dimension-less barrier strength. For $E > \Delta$,

$$\begin{aligned} A(E) &= \frac{u_0^2 v_0^2}{\gamma^2} \\ B(E) &= \frac{(u_0^2 - v_0^2)^2 Z^2(1+Z^2)}{\gamma^2} \end{aligned} \tag{48}$$

The BCS coherence factors are given as,

$$\begin{aligned} u_0^2 = 1 - v_0^2 &= \frac{1}{2}\{1 + [(E^2 - \Delta^2)/E^2]^{1/2}\} \\ \gamma^2 &= [u_0^2 + Z^2(u_0^2 - v_0^2)]^2 \end{aligned} \tag{49}$$

For a voltage-biased junction, for a given applied voltage V, current in the junction can be numerically calculated using Eq. 46. In Fig 15, a comparison

of differential resistance vs. junction voltage plots calculated through the BTK theory and those obtained experimentally is shown. Plots at different temperatures are compared as well.

For a graphene-titanium oxide-aluminum (SIGIS) tunnel junction it is found that a barrier strength of $Z = 3$ best describes the contact transparency. Higher temperature experimental data (just below T_c) are matched with the BTK prediction to obtain the value of Z. However, the entire range of plots at different temperatures do not match the BTK calculations. This is most likely due to hopping conduction through states in an imperfect titanium oxide barrier which causes suppression of tunneling. At lower temperatures an exponential increase in the resistance predicted by the BTK calculations is not observed. In Fig 15, a normalized differential resistance variation with junction voltage is plotted. R_N is calculated as the resistance just below T_c, where the lead resistance has disappeared.

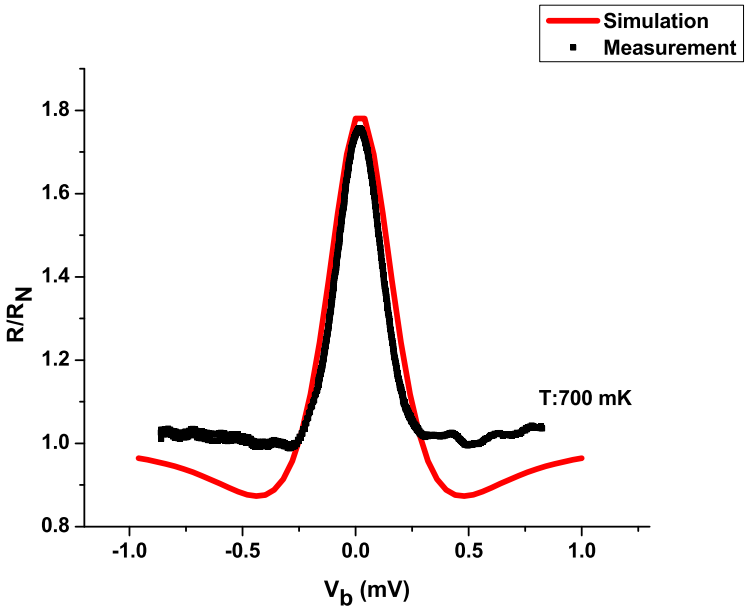

Figure 15: Comparison between the experimental data and BTK calculations for a SIGIS device using titanium oxide - aluminum contacts with a $T_c \sim 0.9$ K. For the device plotted here, $R_N \sim 1.5$ kΩ. Calculations indicate $Z = 3$ for this particular device.

For a graphene-titanium oxide - niobium nitride (SIGIS) device, measured at higher temperatures, the BTK calculations do not predict the experimentally observed behavior. This is due to the fact that at higher temperatures, hopping conduction is less suppressed and dominates over the superconducting tunneling process.

Even though a perfect tunnel barrier is not achieved using titanium oxide at this point, to observe the electron-phonon coupling only having a large resistance suffices. This is due to the fact that large contact resistance is able to minimize the Wiedemann-Franz contribution of the out-diffusion thermal conductance allowing the observation of inherent electron-phonon coupling dominated cooling. However, development of a close to ideal tunnel barrier which gives exponential increase of resistance at low temperatures may be necessary in order to achieve the ultimate sensitivity that these graphene-superconductor bolometer devices have to offer.

For a graphene-Josephson junction, observation of a fully developed supercurrent along with Andreev reflections is taken as the evidence for highly transparent contacts with Z close to zero and these plots are not compared with the BTK simulations.

5 Fabrication and Measurement Setup

In this chapter, the fabrication process adapted and refined to realize graphene-superconductor junctions is described. Until the metal contacts definition step, fabrication method is similar for both types of junctions, tunnel and transparent. However, for clarity the process specific to transparent superconducting contacts fabrication is described in chapter 7. For the study of electron-phonon coupling in bilayer graphene, an additional step of Raman spectroscopy is required for identification.

5.1 Nanofabrication

5.1.1 Mechanical exfoliation of graphene

Graphene flakes are mechanically exfoliated either from a highly oriented pyrolytic (HOPG) graphite using the "blow-press method" or from natural graphite flakes using the "tape-method". "The Blow-press method" consists of exfoliating a thin foil of graphite by gently peeling the HOPG graphite with a scotch tape, and transferring it to a substrate with the use of a sharp and clean tweezer [67]. The foil is pressed down on the substrate by applying pressure using compressed high purity nitrogen gas through a stainless steel needle, for ~ 5 s. Pressure of the N_2 gas is maintained between $20 - 30$ psi. This foil is then removed from the substrate, also by the use of pressurized nitrogen gas, and the substrate is carefully checked under an optical microscope for candidates of single layer graphene. This process is repeated until a few graphene flakes are identified as single atomic layer thick. This process has the advantage of having almost no tape residue on the substrate. It is found that for the optimum exfoliation conditions, humidity levels in the surroundings should not exceed 30%, which is ensured using a dehumidifier. All the results included in this thesis pertaining to single layer graphene, were obtained by using the "blow-press" exfoliation method. However, with this method it is difficult to find large and isolated graphene pieces, which are helpful in studying electron-phonon interactions in graphene. For this purposes, we use natural graphite flakes and the standard scotch-tape peeling method to exfoliate graphene [35]. This process is useful to exfoliate large-area isolated single and bilayer graphene flakes.

A standard substrate consisting of SiO_2 deposited on Si is used. In this thesis, devices described are made from either a 300 nm SiO_2 on a highly

doped Si substrate or a 500 nm SiO_2 on a lightly doped high resistivity Si bottom layer ($15 - 20\ \Omega - \text{cm}$ at 300 K) substrate. Latter is preferred in order to avoid radiation losses in the substrate for high frequency measurements. However, as described later, this choice of substrate makes gate tuning of graphene resistance very difficult since the substrate becomes insulating below $T \sim 150$ K.

5.1.2 Raman Spectroscopy

Single layer graphene devices rely on identification through optical microscope contrast. However, to definitely differentiate bilayer from single and trilayer graphene, it is necessary to perform Raman Spectroscopy. These measurements are performed with a WiTec Alpha combination microscope using a 532 nm wavelength laser, situated at the Center for Functional Nanomaterials, Brookhaven National Laboratory.

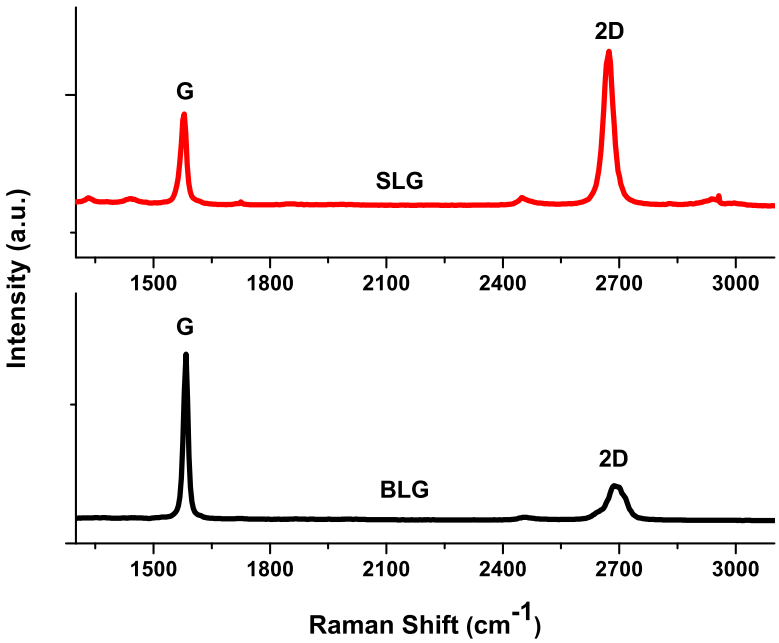

Figure 16: Measured Raman spectra of a single (top) and a bilayer (bottom) graphene flake. Difference in $2D$ peak at $\sim 2700\ \text{cm}^{-1}$ clearly identifies a bilayer graphene.

Raman spectrum of a bilayer graphene differs from that of single layer graphene as described by Ferrari et al. [68]. Spectra for single layer and bilayer graphene are shown in Fig 16, identifying characteristic being the $2D$ peak at ~ 2700 cm^{-1} wavelength. $2D$ peak in a single layer graphene is sharper and of higher intensity than the G peak at ~ 1580 cm^{-1}. The G peak corresponds to a first order Raman scattering process involving the doubly degenerate in-plane longitudinal and transverse optical phonon modes at the Γ point shown in Fig 5 in chapter 1. The $2D$ peak is a result of a second-order process involving two transverse optical phonons at the K point of first Brillouin zone. In bilayer graphene the $2D$ peak is less intense and broader than in the single layer counterpart. Since bilayer graphene consists of two stacked graphene layers with two conduction and two valence bands, phonon selection rules are more complex [11] and the $2D$ peak is a composite of four smaller peaks, which makes it appear broader.

5.1.3 Nanolithography

Spin-coating

After a suitable graphene flake is found, it is spin coated with a ~ 190 nm thick film of Microchem$^{\text{TM}}$ polymer (950 A4 PMMA) resist by spinning at 3000 RPM for 60 s. PMMA is then pre-baked at 180°C for 90 s. There is no post-baking involved.

Electron-beam lithography

Electron beam lithography is used to pattern the devices. In this process, the PMMA is exposed with an electron-beam at a dose of ~ 400 μC/cm^2. Since there is no lithographically defined antenna, metal leads are designed to be as short and wide as possible in order to reduce lead capacitance. All the devices are in a two terminal geometry. They are also designed to be as close as possible to the edge of the substrate in order to reduce the length of wire-bonds and in turn wire inductance. For large flakes of graphene, obtained using natural graphite, additional metal-clamps are designed to pin the graphene flake at corners so that it does not roll-up during the lift-off process. A recipe of developing the patterned device with de-ionized (DI) water is used which has demonstrated lower resist residue [69]. Patterned

devices are developed in 1:3 water: isopropyl alcohol (IPA) at 5°C for 2 min and then rinsed in IPA for 30 s before blow-drying with clean nitrogen gas.

Plasma etch

For the bilayer graphene devices, additional steps of electron-beam lithography and reactive oxygen plasma etching are performed before defining electrical contacts using e-beam lithography. This is done in order to obtain regular shaped smaller area flakes from the large irregular shaped flakes found from natural graphite ($\sim 100 - 200\ \mu\text{m}^2$). Typical plasma etching is done at ~ 20 W power with an O_2 flow rate of 5 ccm at 50 mtorr pressure for 35 s. This is found to etch upto $2 - 3$ layers of graphite.

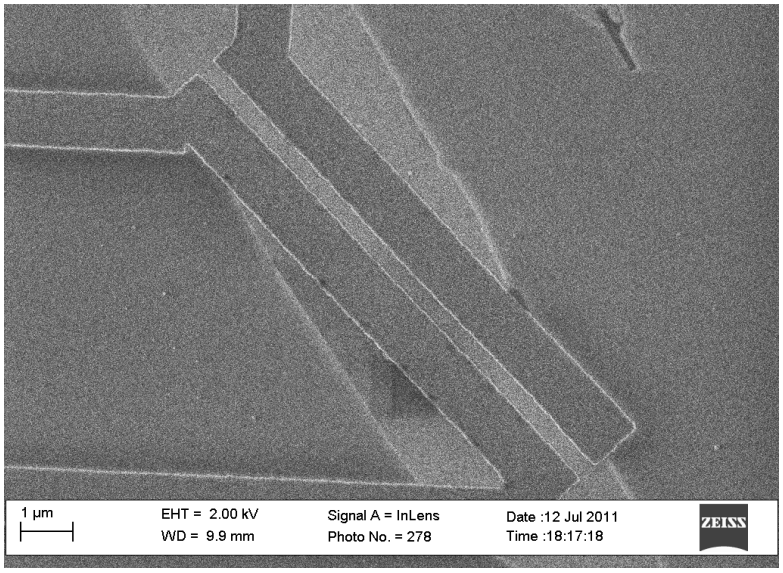

Figure 17: Scanning Electron Microscope (SEM) image of a typical graphene-superconductor junction device. Light gray region is the graphene flake and two dark gray bars on top are the metal contacts.

5.1.4 Thin film deposition

Electron-beam evaporation process is used to fabricate devices with Al superconductor contacts. However, to fabricate graphene-superconductor junctions using either Nb or NbN as a superconductor, it is essential to use a

combination of electron beam evaporation and sputtering process. The reason for this is a high intrinsic stress in the electron-beam evaporated Nb, as explained later.

Electron-beam evaporation

Devices are loaded into the metallization chamber after pattering contacts following brief cleaning using UV-ozone for ~ 1.5 min. Physical vapor deposition technique of electron-beam evaporation is used to coat the first layer of metal on graphene. In electron beam evaporation a crucible containing metal is heated using an electron-beam through a tungsten filament to eject metal in gaseous form. This assembly sits in a high vacuum chamber and the substrate located directly in-sight of the crucible gets coated by the precipitated solid metal film. For graphene-superconductor junctions, the first step is to evaporate a thin layer of Ti, with a typical growth rate of $\sim 1.5 - 2$ Å/s. It is found that a growth rate slower than this introduces contaminants in the evaporated film, which can be detrimental to the tunnel barrier formed or the transparency of Josephson junction contacts. This is the first step in creating either a transparent Josephson junction or tunnel junction. From here on, method of fabricating a tunnel junction differs from that for transparent contacts. Latter is described in chapter 7.

Creating a tunnel barrier

To create a tunnel junction, evaporated Ti is then oxidized. Titanium oxide is chosen as the tunnel oxide for its high dielectric constant, as explained later in this chapter. Several methods of oxidation were tried: exposure to pure oxygen for several hours at different partial pressures, oxidation via plasma or UV generated ozone and oxidation in air at an elevated temperature. Eventually, the method which was found most reliable used oxidation under ambient conditions on a hot-plate at 80°C for ~ 90 min. Oxidation on a hot plate is most likely aided by the presence of moisture in the air [70], especially for devices fabricated during the summer. The reason for choosing a particular oxidization temperature is so that it shouldn't reach above 110°C and melt the resist during the entire oxidation process. After the oxidation, devices are cleaned for 1 min using UV-ozone and loaded back into the metallization chamber for sputtering.

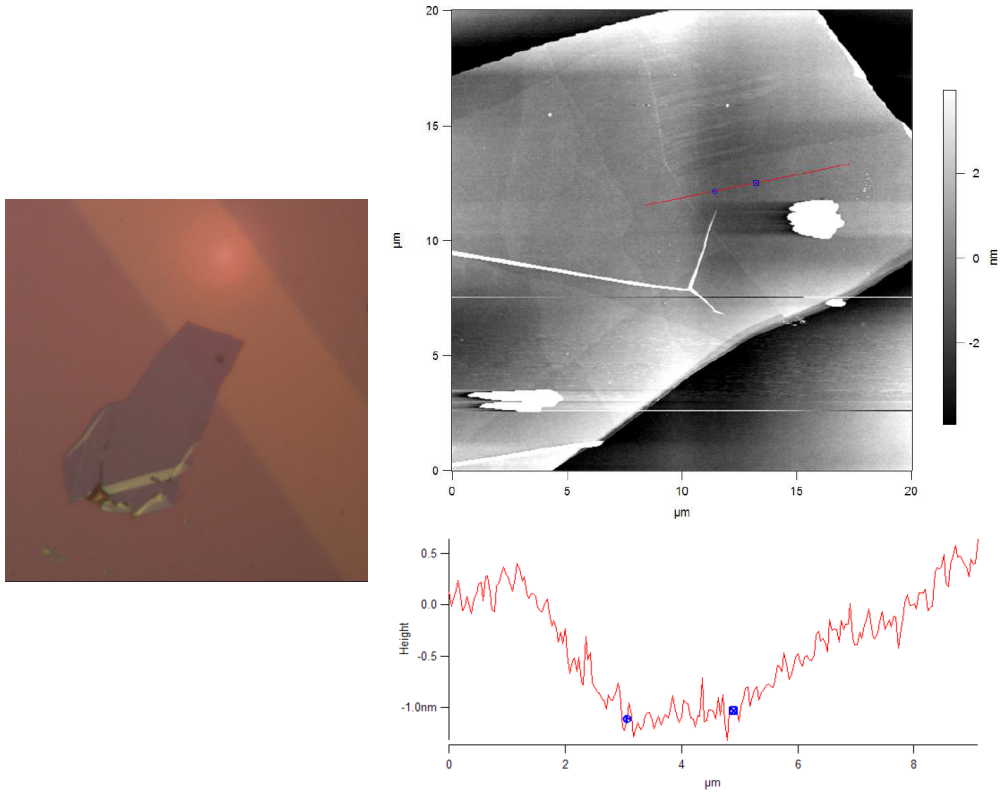

Figure 18: (left) Optical image of a graphite flake with and without Ti coverage. Lighter shade area is without Ti coverage due to a wire mask placed during metal deposition. (right) AFM scan of graphite flake regions with and without Ti coverage. Height scan on the flake area with Ti does not show dips comparable to the height scan of the area without Ti coverage. This indicates a complete coverage of graphene by Ti without pinholes. Height difference of the area with and without Ti coverage demonstrates that the deposited Ti thickness is different from the readings on the thickness monitor.

Thickness of the oxidized titanium determines the tunneling resistance of the device. A $\sim 0.9 - 1$nm thick Ti film is used to create a tunnel barrier with a resistance range of a few tens to few hundreds of $\mathrm{k}\Omega \cdot \mu\mathrm{m}^2$. It can be difficult to precisely determine the thickness of Ti deposited at this range by the thickness monitor crystal and a reading of ~ 1 nm, could have an error as large as ± 0.5 nm. The important thing to insure is that Ti fully covers graphene without having pinholes, so as to prevent leakage into the tunnel

barrier. Although it has been demonstrated that as little as ~ 0.5 nm thick Ti provides full coverage on graphene [71], this is verified through a simple test using an atomic force microscope (AFM).

A relatively thick and big piece of graphite is chosen and then a part of it is covered by a bonding wire. ~ 1 nm thick Ti film (according to the thickness monitor) is deposited on top of it. The wire is then removed and the graphite surface beneath it remains without any Ti coverage. Parts of flake with and without Ti are scanned using AFM to reveal that indeed there are no pinholes present and that the deposited thickness of Ti is ~ 1.5 nm instead of 1 nm measured by the thickness monitor. The optical image of the graphite flake with and without Ti and the AFM profile is shown in Fig 18.

Sputtering

Niobium nitride is chosen as the superconducting material for its high superconducting gap value. As mentioned before, growing Nb or NbN contacts via electron-beam evaporation introduces significant stress in the graphene sheet. For a contact separation of up to ~ 0.5 μm, all of the devices made by using evaporated Nb show open circuit. This is confirmed by the scanning electron microscope image of the torn graphene device below in Fig 19. Here, the graphene sheet is torn due to a high tensile stress induced by contacts.

To create stress-free niobium nitride contacts, sputtering technique is used. Sputtering is a form of physical vapor deposition technique of thin-film deposition where by atoms are removed from a solid target by bombardment of energetic ions. The target sits at the end of a sputter gun in a vacuum chamber. Argon ions created by applying a high DC power (470 W) bombard the target, removing material from it and depositing it on the substrate. In case of reactive sputtering, a reaction of the target metal with a gas takes place during the sputtering process. This is the technique used to deposit NbN contacts which includes Nb target reaction with a N_2 gas to form NbN film on the substrate. Directly sputtering on graphene, however, may result in a damaged graphene sheet due to bombardment of high-energy ions during the sputtering process. The Ti layer evaporated to form a tunnel oxide (in case of transparent contacts fabrication, Ti is used as an adhesion layer as described in chapter 7) protects graphene from this damage due to sputtering.

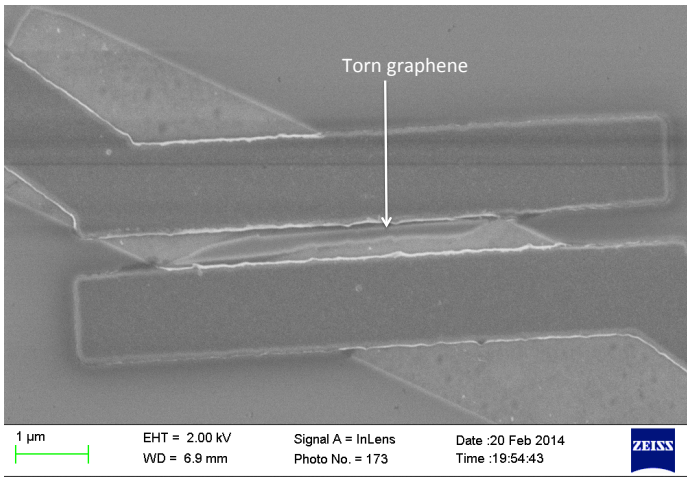

Figure 19: Scanning electron microscope image of a torn graphene (white) channel by highly stressed Nb contacts (gray) deposited through electron-beam evaporation.

NbN is sputtered from a $\sim$ 3" Nb target using a Ar/N_2 mixture. The partial pressure of the mixture is adjusted depending on the target conditions, which changes over time, to produce lowest stress films. A typical film, such as the one used for the bilayer graphene devices is sputtered with a partial pressure of Ar/N_2 mixture at $\sim$ 6.4 mTorr and an Ar pressure of $\sim$ 1.1 mTorr. Sputtering is done at a fixed power of 470 W. The target is first pre-sputtered for 80 s and then the device is exposed to the plasma for NbN coating without turning off the sputter gun in between. $\sim$ 30 nm of NbN is coated onto the device. During sputtering, the total pressure drops by $\sim$ 0.15 mTorr as a result of $Nb - N_2$ reaction. The voltage and current values of the sputter gun are in the ranges of $314 - 319$ V and $1.48 - 1.51$ A, respectively. These numbers, however, depend on the condition and usage of the target.

The lowest stress point of the film, which changes with the eroding target, is determined periodically using a series of tests [65]. The sign of the NbN film stress is determined by sputtering the films on top of stress-free Al films pre-evaporated onto PMMA. In acetone, the lifted-off NbN/Al bi-metal films roll either upward or downward depending on the sign of the stress in NbN. Consistent with literature [72], it has been found that a low Ar pressure results in a compressive stress, while a high Ar pressure causes a tensile stress. N_2 proportions affect the T_c of the film. It is also seen that the NbN film can have the internal stress gradient, possibly caused by the change of

local sputtering pressure/stoichiometry of the Ar/N_2 mixture. This effect is reduced by allowing a large flow of the gas mixture. The reaction of N_2 with Nb causes the pressure to decrease during the sputtering. The pressure drop is used as a key parameter to determine if the flow is sufficient to produce uniformly stressed films. To achieve a preferred uniform stress, the pressure decrease is found to be less than 0.2 mTorr. A typical value of ~ 0.15 mTorr drop is used in the sputtering process.

5.2 Measurement setup

There are several temperature scales at which devices described in this thesis are measured, depending on the superconducting transition temperature (T_c) of the contacts. For superconductors with $T_c > 4$ K, using liquid He dewar suffices. For devices with $T_c < 1.5$ K, a dilution fridge is required.

5.2.1 Dilution refrigerator setup

The devices using Al as a superconductor are measured in an Oxford^{TM} dilution refrigerator. A dilution refrigerator uses the spontaneous phase separation between liquid ^{3}He and ^{4}He below 800 mK to achieve a dilute ^{3}He phase. This allows the device to cool to temperatures as low as few tens of mK. Since Al superconducts below 1 K, it is necessary to use the dilution fridge to perform measurements. Transport measurements are performed by supplying the devices with a sweeping DC offset current and a small AC modulation current, both using a Keithley 6221 current source. The junction voltage response under the AC modulation current is measured using a SR830 lock-in amplifier, from which the dynamic resistance dV/dI was calculated. The DC junction voltage bias, V_b, is measured using a Keithley 2182A nanovoltmeter. A variable gain voltage amplifier (SIM 900 scaling amplifier) isolates the input current from output voltage. The measurement circuit diagram is shown in Fig 20.

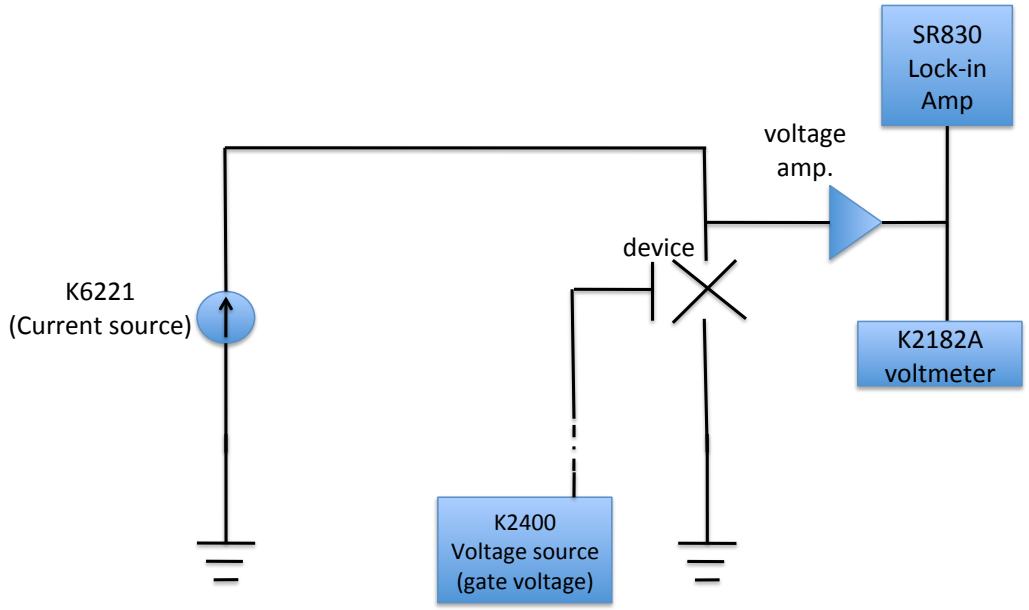

Figure 20: Circuit diagram for differential resistance measurements in a graphene-superconductor junction device with a gate terminal.

Both the current source and the lock-in amplifier are connected to the device through twisted-pair cables which are filtered with EMI π-filters at room temperature and RC filters (with $\sim$ 1 kHz cut-off frequency) at $\sim$ 1.5 K. In the dilution fridge, RF power is applied through a coaxial cable with an open end located about 10 cm away from the devices. To decide on the frequency of the applied radiation, the frequency response of the device at fixed applied RF power is measured. The RF frequency at which a minimum RF power is required to generate a large bolometer response is chosen. In this way, the RF heating to the fridge/bath is minimized. No antenna is used, so only a small fraction of the applied power radiates out and is picked up by the device [3].

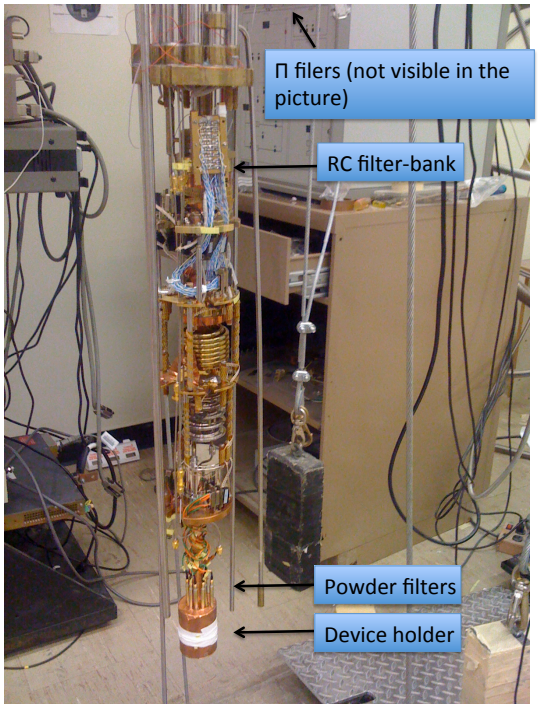

Figure 21: Devices with Al as a superconductor are measured using a cryogenic dilution refrigerator at $\sim$ 160 mK. Three stage filters that work in different frequency spectrum are labeled in the picture, a π filter-bank at the top is not visible in this picture.

Absorbed power calibration

Graphene superconductor tunnel junctions are chiefly used for bolometric characterization. Hence, it is essential to have a close estimate of the amount of power absorbed for these devices. Since most of the applied power radiates out due to lack of an antenna, only a small fraction gets picked up by the devices. To calibrate the power received by a device, a 50 Ω resistor (on a PCB) is placed in series in the close vicinity of the device. Radiation is applied the same way as it is during a real experimental situation, via an open-ended co-ax cable. An RF oscilloscope with a 50 Ω input impedance is used to measure voltage across the resistor, from which the current through the device can be estimated. The device tunnel contacts are modeled as a resistor in parallel with a capacitor with source-drain capacitance. And the

heating of the sample was calculated using the current through the resistive channel as $P = I^2R$ [3]. For tunnel devices with Al as a superconductor, a doped Si substrate was used, which has a capacitive coupling to graphene labeled as C_{chan} in Fig 22. High frequency losses through this conductive substrate are not taken into account in the calculation of absorbed power. Hence, the estimate of thermal conductance for graphene - titanium oxide - aluminum devices is only an upper bound.

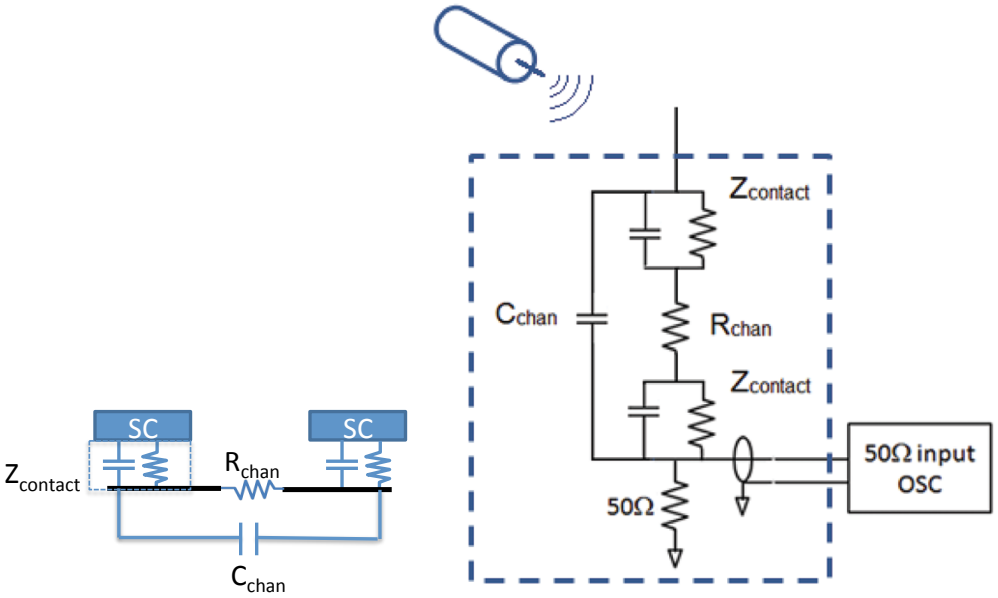

Figure 22: (left) Lumped parameter model of a graphene-superconductor tunnel junction. Graphene channel is modeled as a resistor and the superconducting tunnel contacts are modeled as a tunnel resistance in parallel with an oxide capacitance. (right) A 50 Ω resistor placed in series with the device is used to estimate power absorbed in the device.

5.2.2 High frequency insert

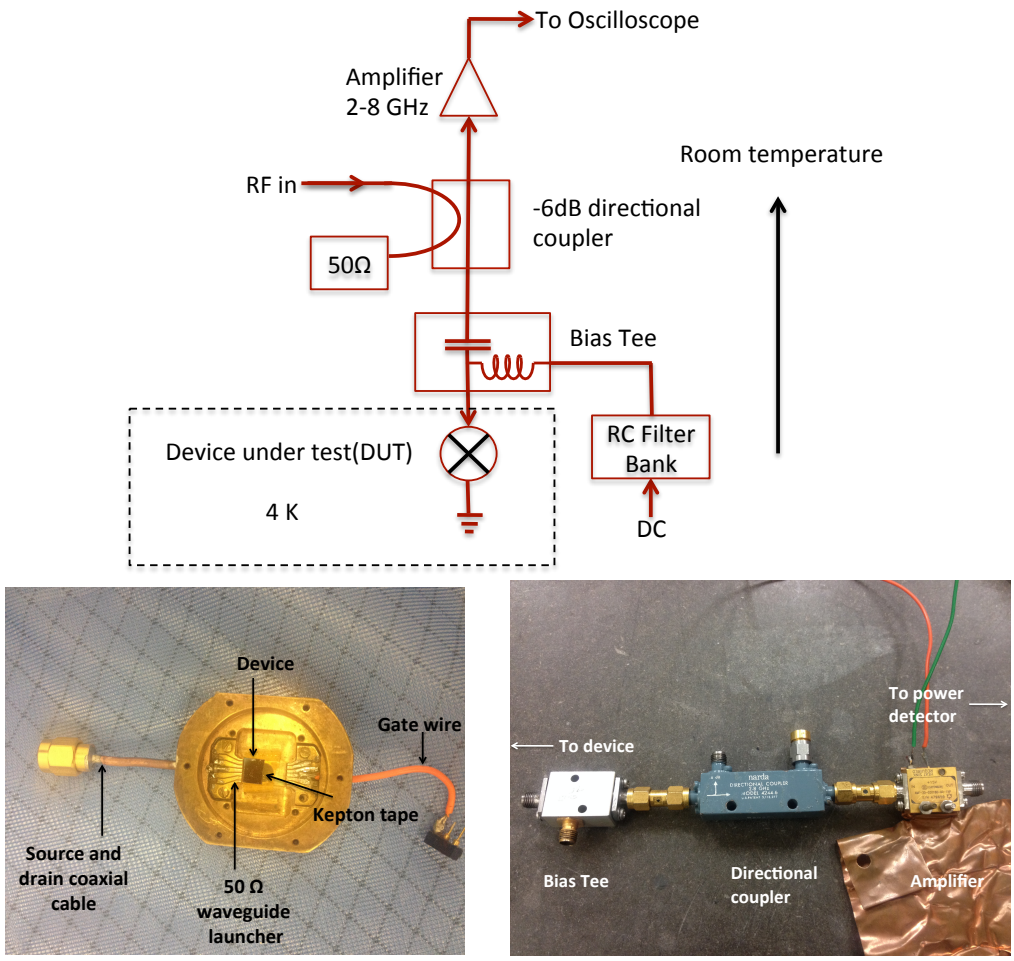

Figure 23: (top) Schematics of the setup used to measure NbN devices at liquid helium temperature $\sim$ 4.2 K. (bottom left) Sample holder used to measure the DC response of the device and simultaneously apply RF heating signal. Connection of wire bonds to the co-ax cable is through a 50 Ω waveguide launcher. (bottom right) High frequency components to apply radiation power and measure the reflected power.

For NbN devices, superconducting transition occurs at $T_c \sim 11$ K. Hence, these devices are measured at liquid helium temperature and do not require

the use of dilution refrigerator. The measurement setup schematic used for this temperature range is shown in Fig 23. The RF signal which heats the absorber is provided by an Agilent E4422 RF signal generator. A directional coupler couples the input RF signal through the RF/capacitive port of a bias tee into the device under test(DUT). The reflected RF signal from the device, appearing at the capacitive port of the bias tee is amplified by an RF amplifier before being measured by an Agilent E4416 power meter. The DC characteristics of the devices are measured by passing a low frequency current using a Keithley 6221 current source through the DC/inductive port of the bias tee. At the same time, the voltage drop is measured using a SR830 lock-in amplifier. At room temperature, a bank of two-stage RC low pass filters is used to heavily filter out the high frequency noise in the DC branch. All of the RF components have their responses limited to frequencies between $2 - 8$ GHz, and the measurements are done at 4 GHz where the amplifier has a maximum gain ($\sim$ 26 dB) for the reflected power. All RF components are kept at room temperature in this setup and the connection to the device in the cryostat is through a semi-rigid coaxial cable. A calibrated Lakeshore^{TM} Ruthenium oxide thermometer is used to measure the bath temperature [50].

The device holder shown in Fig 23 (bottom) consists of a 50 Ω waveguide launcher designed using a Au-coated PCB microstrip waveguide design. The coaxial cable used to carry source/drain signal is soldered to this waveguide which is then wire bonded to the device. Multiple short wire-bonds (3 to 4) on each pad are used to reduce the wire inductance added into the device impedance. It is ensured that the devices are close to the substrate edge to shorten the wire lengths. Kepton tape is inserted between the device chip and sample holder in order to prevent any accidental short to the ground. A DC wire soldered to the opposite end of the sample holder carries a gate signal to the device.

Absorbed power calibration

To accurately obtain the RF power absorbed by the device, measurement setup is calibrated by measuring the gain/loss of each section and by calibrating using a 50 Ω, short and open loads, from which the gain/loss of each branch of the circuit is obtained. The voltage reflection coefficient Γ_R for the

device is given by,

$$\Gamma_R{}^2 = \frac{P_o}{P_i} \tag{50}$$

where, P_o and P_i represent reflected (output) power and applied (input) power in watts respectively at the device under test (DUT). From equation 50 and the relation, $P_{abs} = (1-\Gamma_R{}^2)P_i$ we can calculate the power absorbed in the device. The voltage reflection coefficient in turn can be used to determine the device impedance as seen by the RF signal:

$$\Gamma_R = \frac{Z_{device} - Z_{source}}{Z_{device} + Z_{source}} \tag{51}$$

where $Z_{source} = 50\ \Omega$. The measurement of the absorbed power in the device is reasonably accurate when the device impedance is comparable to 50 Ω.

Measurement setup shown in Fig 23 allows measurement of power reflected from the device. In a graphene-TiOx-NbN device, for an applied power of −61 dBm at the DUT, the measured temperature dependence of the reflected power is shown in Fig 24 (top) [50]. For $T > T_c$, when the leads are resistive, applied power is mostly reflected back, implying $\Gamma_R \sim 1$. As the leads become superconducting at $T \sim T_c$, the reflected power sharply drops, and after a small dip it settles to a constant value for $T < T_c$. This is mirrored in the reflection coefficient magnitude as a sharp drop to a minimum value before slightly turning up and roughly flattening out when $T < T_c$. This is in contrast with the DC resistance measurement in which the device resistance increases continuously with decreasing temperature for $T < T_c$ (Fig 24 (bottom)), signaling that the device impedance at high frequencies is very different from the DC resistance.

The lumped parameter model of the device, shown in Fig. 22 (left) can explain this difference. With C being the contact capacitance of each metal-graphene junction, the device impedance can be written as

$$Z_{device} = \frac{2R_cZ_c}{R_c + Z_c} + R_L + R_g \tag{52}$$

where R_g is the resistance of the graphene channel, R_L is the lead resistance, R_c is the DC contact resistance for each contact and $Z_c = j/2\pi fC$. Since titanium oxide has a large dielectric constant ($\epsilon \sim 100$), a large capacitance between graphene and the superconducting contacts is present.

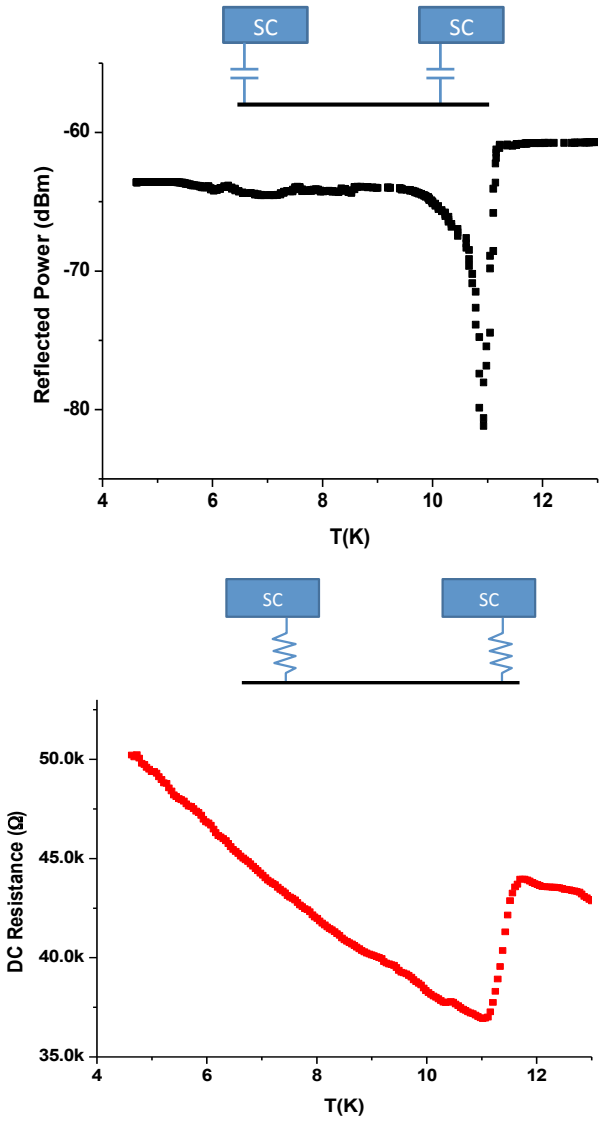

Figure 24: Difference in reflected power vs. DC resistance temperature trends. (top) Variation of power reflected by the device with temperature. (bottom) Variation of DC resistance of the device with temperature. Difference in the top and bottom curves suggests that the RF device resistance is different from the DC resistance.

For example, for one of the devices with 14 μm^2 contacts, this capaci-

tance is estimated to be $\sim$ 12 pF for each contact, which leads to a capacitive impedance of 3 Ω at the frequency of 4 GHz used in the measurements. This capacitive impedance, which is in parallel with the tunneling/contact resistance of a few kΩ, provides a short circuit path for the RF signal. Consequently, the resistance of the graphene channel, which is roughly temperature independent, is the main contribution to RF impedance. For the RF signal, neglecting the DC contact resistance, R_c,

$$Z_{device} \approx 2Z_c + R_L + R_g \equiv 2Z_c + R \tag{53}$$

where $R = R_L + R_g$ is the real component of the impedance.

Thus, for $T < T_c$, the device impedance at high frequencies can be estimated from the design geometry by using the estimated capacitance and graphene resistance based on the gate voltage applied and the device aspect ratio. It is however, difficult to determine this high frequency impedance accurately due to the presence of reflective components along the channel used to apply/measure power. Although these reflections are difficult to estimate and give a large error margin on the calculated reflection coefficient and the high frequency device impedance, the absorbed power calculation is not affected by the presence of these reflections, which is the quantity subsequently used to calculate thermal conductance and the sensitivity of a bolometric device.

In case of the presence of reflective components along the way, the input/output channel can be divided into sections of known loss and unknown reflections. Detailed calculations of how applied and reflected power propagate through the insert give the relation between absorbed power and applied/measured power which does not require the knowledge of reflections along the channels. The final expression then becomes,

$$P_{abs} = \frac{P_{applied}}{\beta} + \frac{P_{measured}}{\alpha} \tag{54}$$

Here, $P_{applied}$ and $P_{measured}$ are power applied at the directional coupler end and power measured at the amplifier end, respectively. Both $P_{applied}$ and $P_{measured}$ in Eq 54 are in Watts. α is the loss of input line and β is total loss in the input and output channels combined, in Watts. α can be calculated as the difference in the applied power at the RF port of directional coupler and the measured power at the device end. β is calculated as the difference in measured and applied power when all of the applied power is reflected.

This is given as the power reflected by the device when $T > T_c$, since a high two-terminal resistance including the lead resistance acts as an open load. This way, wire binding losses/reflections are also taken into account.

Amplifier noise subtraction

The RF amplifier which is kept at room temperature has a finite noise power, which is the minimum reflected power that can be measured. Measured reflected power does not change beyond the amplifier noise threshold until the applied power reaches a certain value. In the amplifier used for measurements described here, the amplifier output noise power is ~ -47 dBm. This noise power is subtracted from the measured reflected power. The exact noise power is determined by linearizing noise subtracted reflected power vs. applied power curve as shown is Fig 25 (bottom).

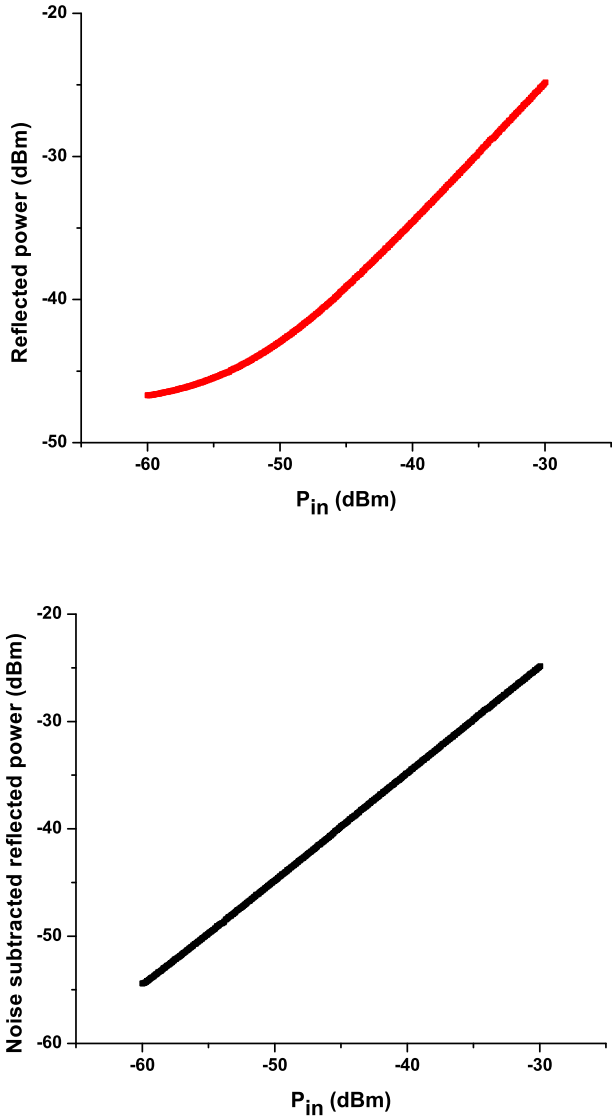

Figure 25: (top) Amplified reflected power vs. applied power without the amplifier noise subtracted. (bottom) Amplified reflected power vs. applied power with the amplifier noise subtracted.

It is also noteworthy that the room temperature RF miteq^{TM} amplifier used here, requires a heat sink. For optimum operation it should be allowed

to stabilize for $t > 15$ min as shown in Fig 26.

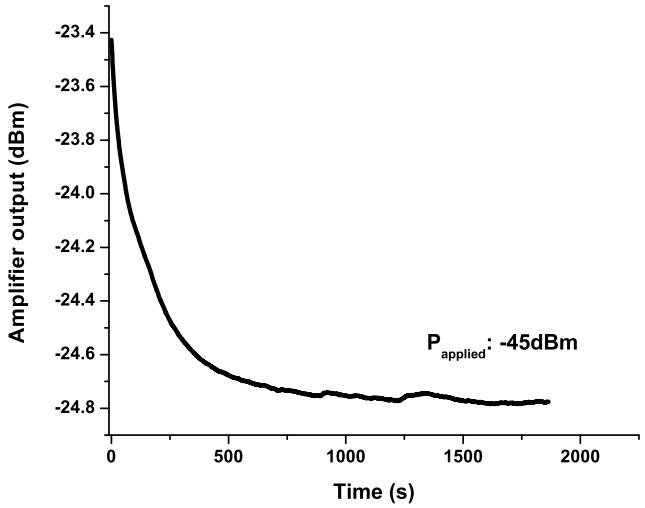

Figure 26: Amplifier gain vs Time. For the particular amplifier used, it takes ~ 16 min to stabilize.

6 Graphene Superconductor Tunnel Junctions (STJ)

Graphene-superconductor tunnel junction (STJ) devices are implemented with an oxide barrier sandwiched between graphene and superconducting contacts. Due to its large dielectric constant, useful for achieving an antenna impedance matched device, titanium oxide (TiOx) is used as the tunnel oxide. Devices with two different superconductors as contacts are demonstrated, aluminum (Al) and niobium nitride (NbN). The STJ device structure discussed here serves two purposes:

1. To provide a sizable temperature response of the junction resistance. In a typical graphene device with normal contacts, due to the weak contribution of resistance from electron-phonon scattering, resistance away from Dirac point is rather insensitive to temperature [17, 47], making it difficult to achieve sufficient responsivity. In a graphene STJ, the junction resistance at bias $V_b < 2\Delta$ is dominated by the tunneling of the thermally excited quasiparticles, which shows strong temperature dependence (Fig 27 (top)).

2. To provide thermal isolation to the electrons within the graphene channel. This is achieved by significantly cutting down the quasiparticle tunneling from graphene into the superconductor when the Fermi level is within the superconducting gap of the leads.

By applying radio frequency (RF) radiation to the devices, the graphene absorber is heated up, its electronic temperature-induced decrease in the tunneling resistance (voltage) can be measured using a DC setup. By comparing the device characteristics under radiation with that in absence of radiation at various bath temperatures, the temperature increase at corresponding RF power is obtained. This relation is then used to calculate the noise equivalent power and responsivity of the graphene STJ bolometers. Apart from the characterization as a bolometer, graphene STJ geometry can also be employed to study hot-electron cooling mechanism in graphene. By blocking cooling from various mechanisms, this device geometry allows hot electrons in graphene to cool chiefly via electron-phonon interactions. Thus, allowing observation of the phonon cooling power temperature dependence and its variation due to disorder, doping etc.

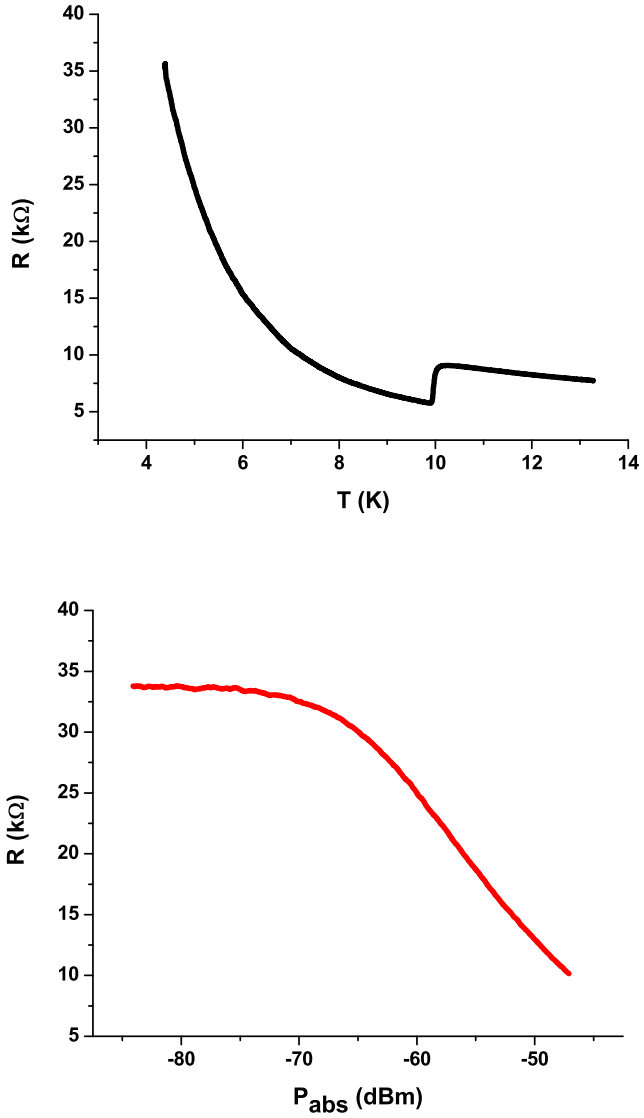

Figure 27: (top) Temperature dependence of zero-bias resistance in a graphene STJ junction with NbN superconducting contacts. (bottom) Radiation response of a graphene STJ junction, measured at $T \sim 4.5$ K. Both plots are measured with 20 nA excitation.

6.1 Single layer graphene

Single layer graphene STJ devices with Al and NbN as superconductors are used to characterize bolometric parameters of thermal conductance (G) and noise equivalent power (NEP).

6.1.1 Graphene STJ junctions with Al

These devices are measured in the dilution refrigerator setup, since Al superconducts at T $\sim$ 1 K. Details of the setup along with absorbed power calibration is described in chapter 5, section 5.2.1.

In this particular experiment, a $\sim$ 1 nm thick titanium film is oxidized by brief exposure to pure oxygen at a low partial pressure. Upon cooling down a graphene/TiOx/Al device below 1 K, characteristics of a S-I-N tunnel junction with non-ideal semitransparent barrier are observed in the dynamic resistance (dV/dI) vs. bias voltage dependence, as shown in Fig 28. This dynamic conductance vs. bias voltage dependence is fitted with the BTK model as described in chapter 4 and a barrier strength of $Z \sim 3$ is estimated. The dynamic resistance is measured by supplying the devices with a combination of a small AC current ($I_{mod} = 10$ nA) and sweeping offset current, both provided by a Keithley 6221 current source. The AC component of the voltage response V_{mod} is measured using an SR 830 Lock-In amplifier, from which the dynamic resistance $dV/dI = V_{mod}/I_{mod}$ is calculated. The DC bias is amplified (with a gain of $\sim$ 1000) and measured by a DC voltmeter. When the junctions are biased outside the superconducting gap $V_b > 2\Delta$, the dynamic resistance is roughly bias-voltage independent. For $V_b < 2\Delta$, the quasiparticle tunneling is suppressed by the superconducting gap, resulting in increasing of dynamic resistance. The observed critical bias voltage below which the dynamic resistance increases gives $2\Delta \sim 0.25$ mV, consistent with the reported superconducting gap of aluminum. Reducing the temperature induces significant increase of the dynamic resistance within the superconducting gap, as a result of reduced thermal excitation and hence quasiparticle tunneling.

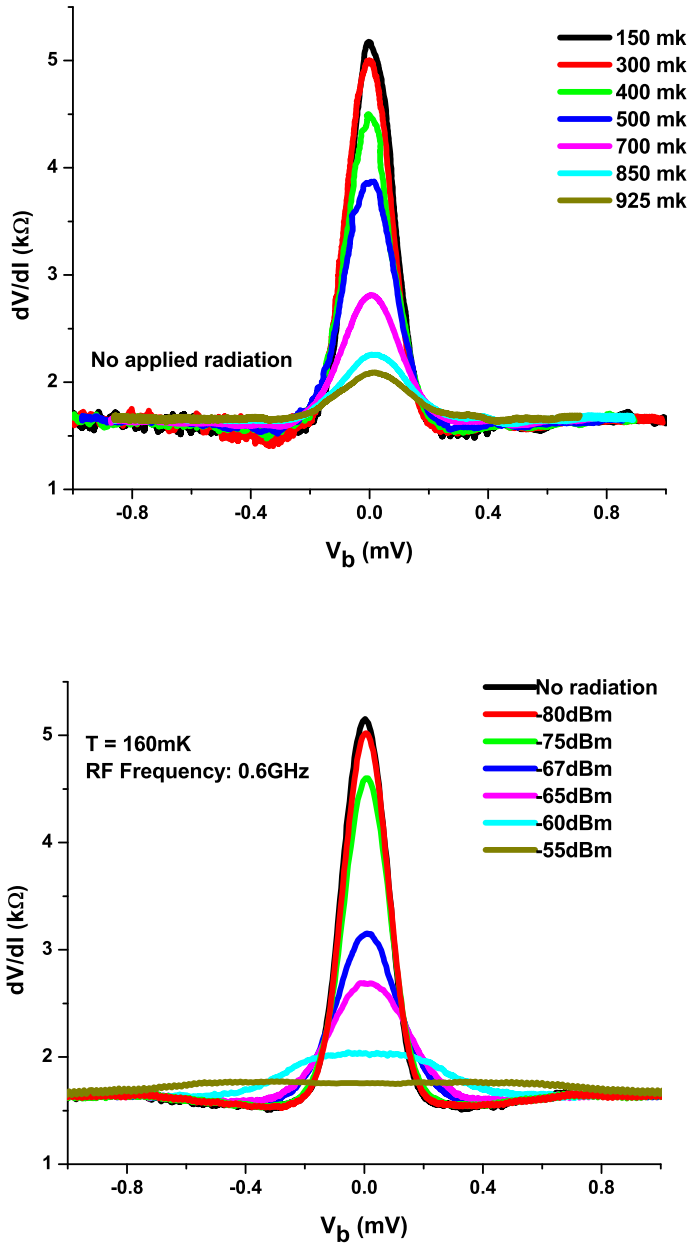

Figure 28: Differential resistance vs. junction voltage. Comparison for differential voltage vs. voltage bias curves at different bath temperatures (top) and different applied radiation levels (bottom) for a graphene-TiOx-Al STJ device.

By measuring the bias voltage dependence of the dynamic resistance at various temperatures in absence of the RF radiation, a temperature calibration is obtained. In this measurement scheme, heating of electrons is achieved through RF power. At the base temperature of 160 mK, RF power is applied at a fix frequency of 600 MHz. In the dilution fridge, due to the radiation shield and the open-ended co-axial cable used for power delivery, resonances are created in the device (Fig 29). The frequency of RF power delivery is chosen so that maximum power is absorbed in the device.

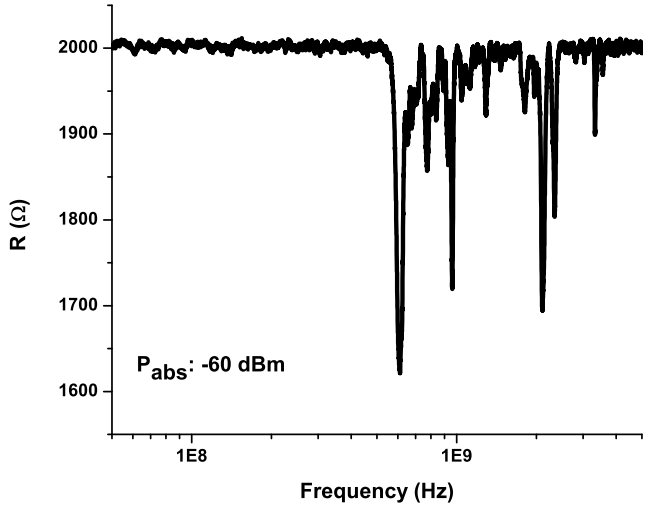

Figure 29: Response to radiation power vs. frequency of the applied power. Frequency chosen for subsequent measurements is based on the maximum recorded response at ~ 600 MHz.

Amplitude of the RF power is limited so that the bath temperature measured by a calibrated Lakeshore cernox^{TM} thermometer shows no observable increase. For $P < -90$ dBm on the devices, no significant change in the differential resistance is observed. Between $P = -90$ and -50 dBm, decrease of tunneling resistance within $V_b < 2\Delta$ is observed with increasing applied RF power (Fig 28 (bottom)), similar to that observed with increasing bath temperature. Above $P = -50$ dBm on the device, an increase in the bath temperature is observed. Thus, calibration is limited to the range of $P = -90$ to -50 dBm.

To understand the nature of the RF radiation-induced dynamic resistance change, dV/dI vs V_b plots measured under RF radiation and those measured in absence of RF radiation but at higher bath temperatures are compared. Figure 30 (top) shows such comparison between two measurements: T = 160 mK/ − 75 dBm vs. T = 400 mK/no RF. The near-perfect overlap of the two curves strongly indicates that the effect of RF radiation on the devices is predominantly of electronic heating. Thus, the response of the device is said to be bolometric. The slight difference may be attributed to the small difference in superconducting gap for these two situations, resulting from the different bath temperatures and hence temperature of the superconducting leads. This hypothesis is supported by the comparison of plots at stronger radiation power/higher temperature, such as shown in Figure 30 (bottom) (T = 160 mK/ − 60 dBm vs. T = 925 mK/no RF). Here a clear difference is seen. The 950 mK/no RF curve is narrower compared to the 160 mK/ − 60 dBm curve, as a result of significantly reduced superconducting gap close to T_c. The comparisons here suggest that the RF radiation drives the electrons in graphene out of thermal equilibrium, as the superconducting leads stay at the bath temperature.

Characterization of the graphene STJ device as a bolometer is done in the following way. Consider graphene as a radiation absorber which sits inside a bath of temperature T_t, and is heated up by two different power sources: applied radiation P_a, and background radiation P_b. The electronic temperature of graphene is therefore given as:

$$T_e = T_t + f(P_a) + f(P_b) \tag{55}$$

where $f(P)$ describes the heating of electrons under radiation power P. The junction resistance is a monotonic function of electronic temperature $R(T_e)$. In absence of applied radiation ($P_a = 0$), the measure junction resistance is,

$$R_1 = R(T_t + f(0) + f(P_b)) = R(T_t + f(P_b)) \tag{56}$$

On the other hand, at the base temperature, $T_t = T_{t0}$, the measured junction resistance is,

$$R_2 = R(T_{t0} + f(P_a) + f(P_b)) \tag{57}$$

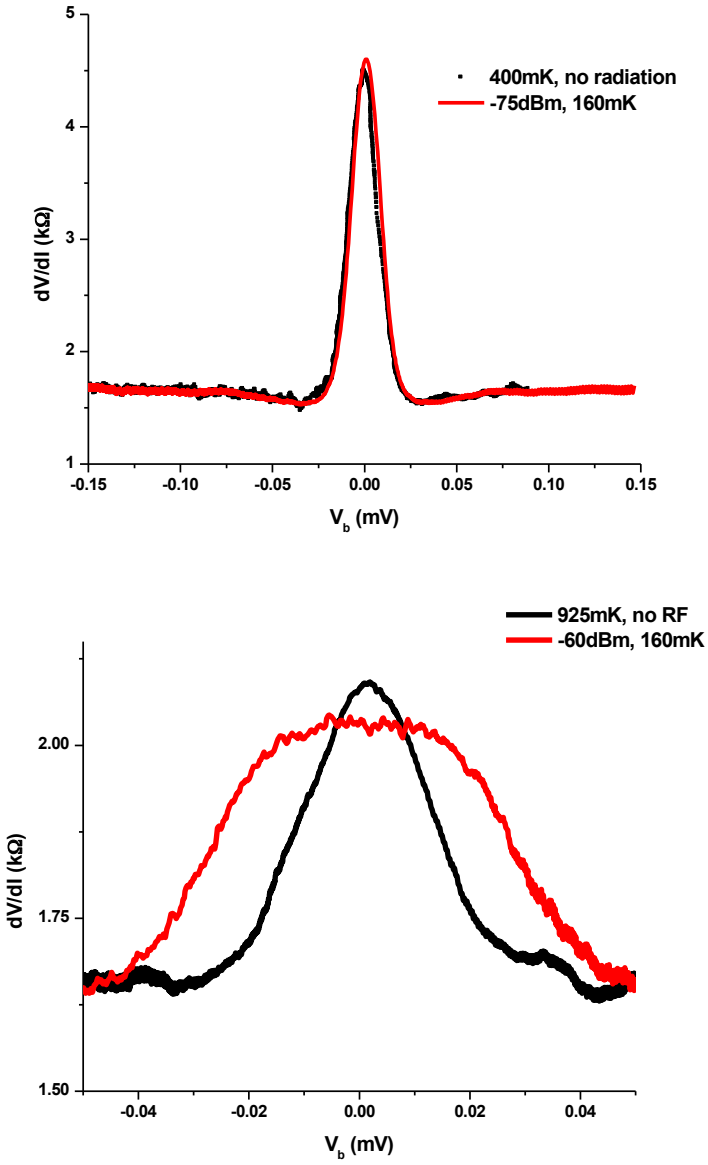

Figure 30: Overlap of the differential resistance vs. junction voltage plots at an elevated bath temperature, with and without any radiation applied. (top) A very good match between the plots at 400 mK and with -75 dBm radiation. (bottom) Plots at higher radiation power and temperatures do not overlap due to the change in superconducting gap at elevated bath temperature close to T_c.

Correlating Eq 56 and Eq 57,

$$\begin{aligned} & R_1 = R_2 \\ \Longrightarrow\ & T_t + f(P_b) = T_{t0} + f(P_a) + f(P_b) \\ \Longrightarrow\ & f(P_a) = T_t - T_{t0} \end{aligned} \tag{58}$$

By matching the dynamic resistance equivalent of two cases: a) at base temperature and under RF radiation; b) higher temperatures without radiation, radiation-induced electronic heating can be deduced. Following this model, the two sets of measurements shown in Fig 28 are compared. This comparison is limited for applied power between -90 and -70 dBm, where the radiation-induced changes in dV/dI vs. V_b curves match well with those at higher temperatures in the absence of radiation.

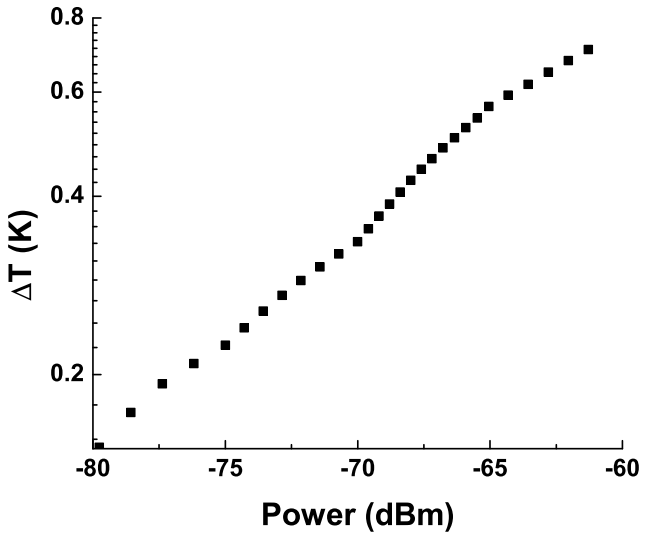

Figure 31: Calibrated relation between temperature raised by the applied radiation power in a a graphene/TiOx/Al device.

With this range, for each applied radiation power at base temperature T_{t0}, a corresponding bath temperature T_t is found, for which the device shows the same dV/dI vs. V_b dependence. Figure 31 plots the relation between applied

RF power and the corresponding electronic heating $\Delta T = T_t - T_{t0}$, for one such graphene/TiOx/Al tunnel junction [3].

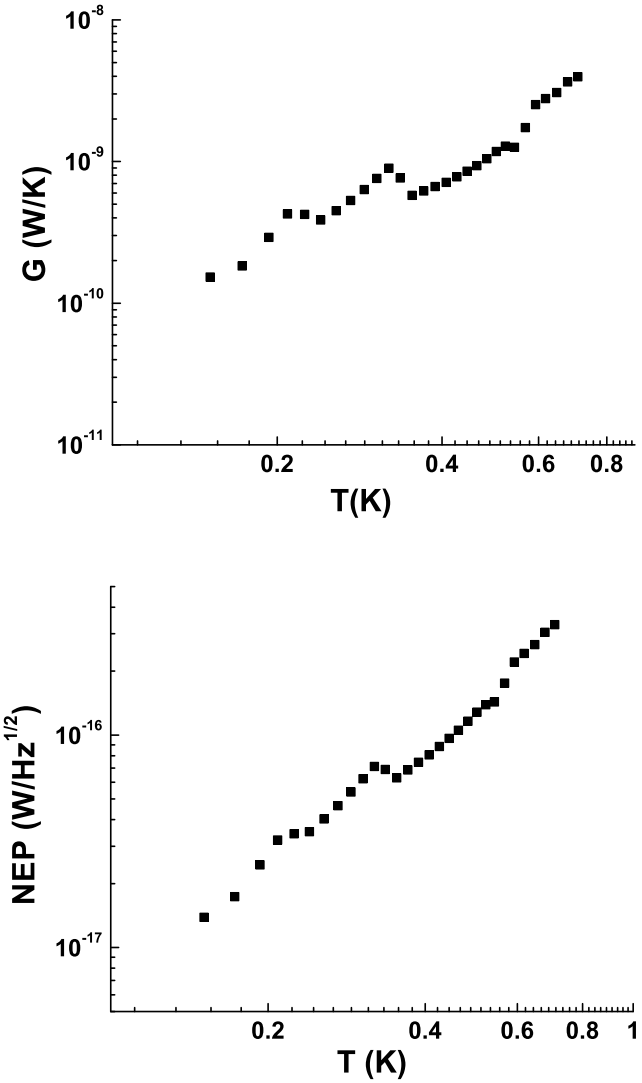

Figure 32: Calculation of bolometric parameters, thermal conductance (G) and the thermal noise equivalent power (NEP) of a graphene STJ device with Al as a superconductor.

From this relation, the heat conductance of the graphene channel ($G = dP/dT$), and the thermal-noise-limited noise equivalent power ($NEP = \sqrt{4k_B T^2 G}$) of this graphene STJ device can be calculated. This is shown in Figure 32.

Next, an order-of-magnitude estimation of the device responsivity (dV/dP) can be obtained by noticing that ~ -60 dBm radiation is required to smear out the superconducting tunnel junction features. This gives,

$$dV/dP \sim \frac{\Delta/e}{-60 \text{ dBm}} \sim 10^5 \text{ V/W} \tag{59}$$

The applied current is limited so that $V = IR << 2\Delta/e$. For the particular device described above with $R \sim 5$ kΩ at zero-bias, an excitation current of $I = 10$ nA is used. This yields $V \sim 50$ μV, which is significantly small compared to $2\Delta/e \sim 200$ μV. Based on this, calculated responsivity dV/dP is shown in Fig 33. At low radiation power $P < -70$ dBm (10^{-10} W), the responsivity is 10^5 V/W. At higher radiation powers, the electron temperature in graphene rises close to the T_c of aluminum, and the responsivity decreases sharply.

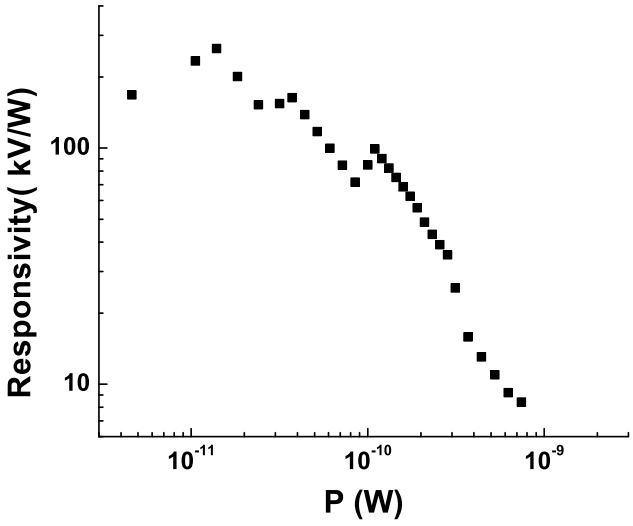

Figure 33: Responsivity of a graphene/TiOx/Al STJ bolometer.

The observed value of thermal conductance at $T = 160$ mK ($G \sim 2 \times$

10^{-10} W/K) can give insight into the dominant cooling mechanism of hot electrons in graphene. For this particular device, no back-gate voltage is applied. However, graphene is assumed to be doped sufficiently far away from the CNP due to substrate-induced electron-hole puddles, doping due to contacts, moisture etc. This would entail $T_{ph} < T_{BG}$. In this regime, the theoretical value of electron-phonon interaction-dominated thermal conductance (G_{e-ph}) in disordered graphene is given as [18],

$$G_{e-ph} = 3\Sigma A {T_e}^2 \tag{60}$$

Here, Σ is the electron-phonon coupling constant. For $E_F \sim 100$ eV, the deformation potential coupling $D \sim 20$ eV and an estimated flake area of $A \sim 10\ \mu m^2$, this contribution is calculated according to ref [18] as, $G_{e-ph} \sim 8 \times 10^{-14}$ W/K. This is orders of magnitude lower than the observed G. Moreover, observed cooling power temperature dependence does not match with that predicted in [18].

Thermal conductance due to out-diffusion of hot electrons from the contacts is given by the Wiedemann-Franz law,

$$G_{WF} = \frac{4\mathcal{L}T_e}{R} \tag{61}$$

Where $\mathcal{L} \sim 2.44 \times 10^{-8}$ WΩK^{-2} is the Lorentz number. The geometrical factor of $\alpha = 4$ comes from the two tunnel resistances of R/2 in parallel as the heat flow channel. For the base temperature ($T = 160$ mK) zero-bias device resistance of ~ 5 kΩ, diffusion thermal conductance is estimated as $G_{WF} \sim 3 \times 10^{-12}$ W/K. This contribution also fails to account for the observed large thermal conductance in these devices. However, it is believed that the dominant error comes from the estimation of absorbed power into the device, which is not measured here accurately. High frequency radiation losses from the conducting substrate have not been taken into account and could be a potential factor contributing to the error in absorbed power calculations.

It can be observed that a contact resistance of 5 kΩ is not sufficient and at mK range of temperatures, the diffusion thermal conductance is higher than that from the electron-phonon coupling.

6.1.2 Graphene STJ junctions with NbN

The devices discussed in the previous section, did not demonstrate phonon cooling due to a number of reasons such as, low contact resistance, the errors

in absorbed power calculations caused due to the particular measurement setup and conducting substrate losses. Thus, to create a phonon bottleneck for electron cooling, a larger resistance titanium oxide barrier and metal contacts with a higher superconducting gap than aluminum need to be implemented. With the use of a higher gapped superconductor, an insert capable of calibrating absorbed power can also be used due to the ease of implementation at higher temperatures. This is achieved with niobium nitride (NbN) as the superconductor. The conducting substrate losses are reduced by using an insulating one.

In the NbN devices described here, titanium is oxidized in the load-lock of metallization chamber using exposure to pure oxygen at ~ 1 atm pressure, for five-six hours. NbN leads show a superconducting transition at $T_c \sim 11$ K. Hence, these devices are measured at liquid helium temperatures using the high frequency cryostat. As discussed in chapter 4, these devices do not fit the BTK description due to the dominance of hopping conduction through a non-ideal titanium oxide barrier. A similar set of differential resistance (dV/dI) vs. voltage bias plots, as those measured for aluminum devices, are obtained here (Fig 34). Albeit, these plots are measured at higher temperatures.

Calibration of the power absorbed in these devices, as well as an estimate of the high frequency device impedance is made using techniques described in chapter 5. The relation between the power absorbed and the electron temperature rise in the TiOx/NbN device is obtained by comparing the dependences of the zero-bias resistance on temperature and on radiation power, similar to the process described in previous section for Al devices. The resulting cooling power vs. temperature curve is shown in Fig. 35. Temperature dependence of the cooling power can be used to determine the dominant hot carrier energy relaxation process, for these higher gapped superconductor devices.

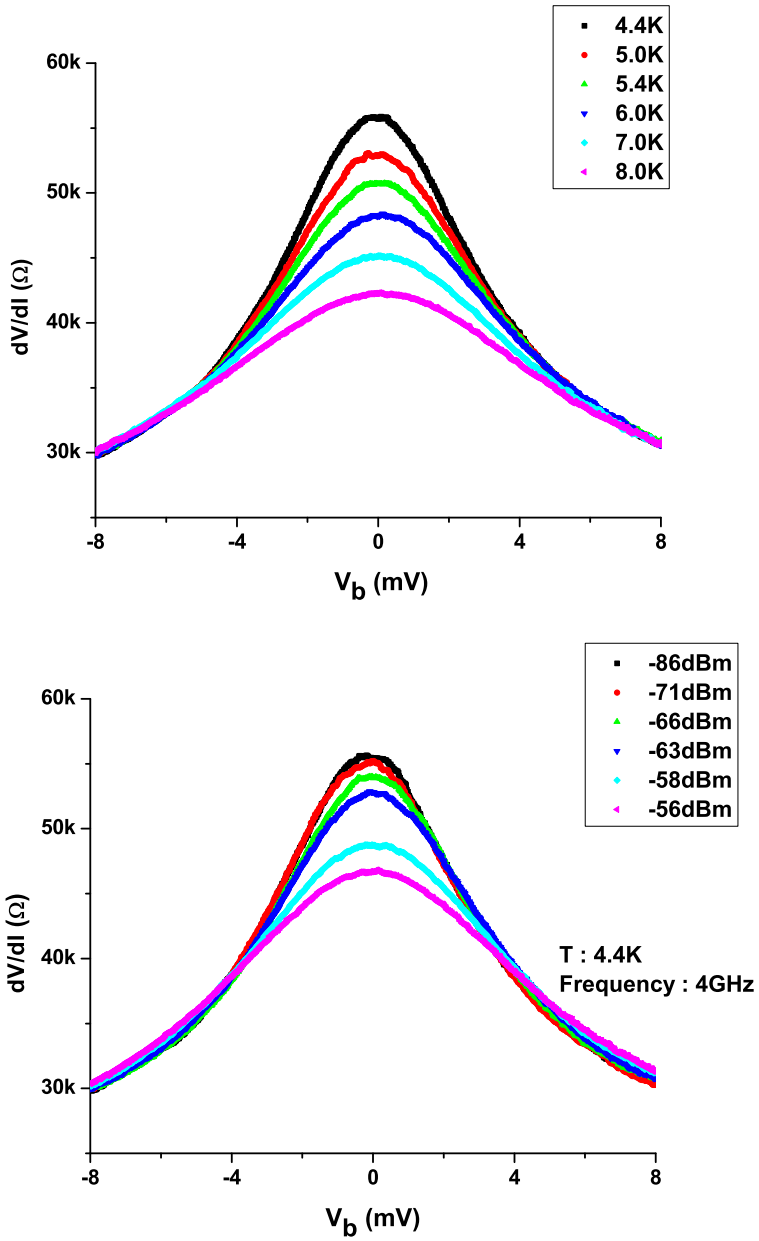

Figure 34: Differential resistance vs. junction voltage. Comparison for differential voltage vs. voltage bias curves at different bath temperatures (top) and different applied radiation levels (bottom) for a graphene-TiOx-NbN STJ device.

Hot electrons can diffuse through metallic leads, given by Wiedemann-Franz law, G_{WF}. The large tunneling resistance, as a result of suppression of quasiparticle tunneling, allows a small diffusion thermal conductance. At $T = 4.5$ K, $R = 51$ kΩ gives $G_{WF} \sim 8.6\times10^{-12}$ W/K, which is orders of magnitude lower than the measured thermal conductance in this particular device, $G \sim 6.7 \times 10^{-10}$ W/K. Hot electrons might then cool down via scattering with graphene phonons, specifically through acoustic phonons in the temperature range of NbN device measurements [13, 24]. Heat transfer between electron and acoustic phonons at low temperatures follows a power law given by [21],

$$P = A\Sigma(T_e^{\delta} - T_{ph}^{\delta}) \tag{62}$$

where A is the area of the graphene flake, Σ is the electron-phonon coupling parameter and $\mathrm{T_e(T_{ph})}$ is the electron(phonon) temperature. The magnitude of the coupling constant Σ and the exponent δ have been calculated in ref [21, 24] for a disorder-free graphene flake. In this case the temperature dependence has been calculated and observed to give $\delta = 4$ [26, 27]. This power-law has been shown to be modified to $\delta = 3$ in the presence of disorder in the graphene flake, although under different mechanisms in different temperature regimes as explained in 1. When $\mathrm{T_{ph} >> T_{BG}}$, ($\mathrm{T_{BG}}$ is the Bloch-Gruneisen temperature of graphene) the presence of disorder affects electron-phonon scattering via the supercollision mechanism [29]. However, when $\mathrm{T_{ph} < T_{BG}}$, as is the case in this experiment, a new temperature regime, based on the disorder level present needs to be taken into account. At these low temperatures, the phonon wavelength becomes comparable to electronic mean free path. This temperature is given by Chen et al. as $T_{dis} = hs/k_B l$, with l being the electron mean free path and $s = 2 \times 10^4$ m/s being the sound velocity in graphene. Below this temperature due to diffusive transport, an electron has longer time to interact with phonons in the graphene channel and according to ref [18], in the case of deformation potential coupling and in the absence of screening, electron-phonon scattering is enhanced and $\delta = 3$ in equation 62.

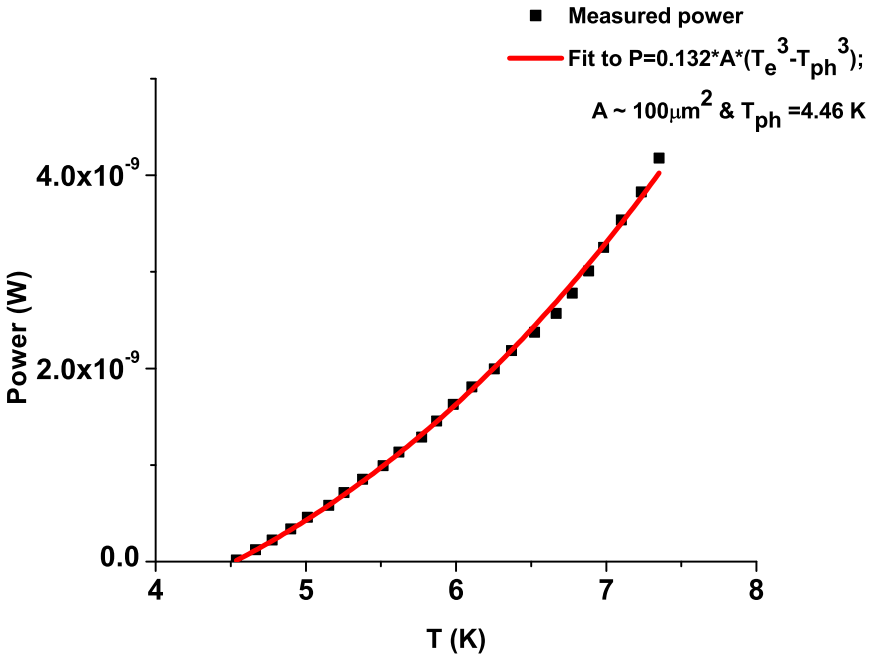

Figure 35: Calibrated relation between temperature raised by the applied radiation power for a graphene/TiOx/NbN device. Cooling power follows a polynomial temperature dependence fitted to a relation $P = 0.132A({T_e}^3 - {T_{ph}}^3)$.

As shown in Fig 35, experimentally observed temperature dependence of power can be fitted to the relation:

$$P = 0.132A(T_e^3 - T_{ph}^3) \tag{63}$$

with an estimated graphene area of $A \sim 100\ \mu\text{m}^2$. Comparing this to equation 62, an electron-phonon coupling of $\Sigma = 132\ \text{mW/K}^3\text{m}^2$ can be extracted. Using a typical mean free path value of $l \sim 20$ nm [52] for graphene on a SiO_2 substrate, T_{dis} is close to 50 K. To avoid high frequency losses, a high resistivity Si substrate is used. This prevents the application of back gate voltage at low temperatures. Due to this, the Fermi energy is not accurately determined. Although, as discussed in case of aluminum devices, it can be safely assumed that the graphene channel is sufficiently doped away from the CNP to satisfy the relation $k_F l << 1$, required for the disorder assisted electron-phonon scattering derived in [18]. Based on the calculations by Chen

et al. in [18], the observed temperature dependence of $P \sim T^3$ occurs only for the case of electron-phonon coupling through deformation potential in the weak screening limit. For this case, Σ is given by,

$$\Sigma = \frac{2\zeta(3){k_B}^3}{\pi^2} D^2 \frac{E_F}{\hbar^4 \rho_m v_F^3 s^2 l} \tag{64}$$

where D is the deformation potential, ρ_M is the mass density of graphene and ζ denotes the Riemann-zeta function. For a highly doped graphene flake on SiO_2 substrate, Fermi energy is assumed to be $\geq$ 100 meV. From the experimentally fitted value of Σ, a lower bound of E_F and assuming a typical mean free path of 20 nm, deformation potential can be estimated to be $D \sim 20$ eV. This matches with the theoretical predictions of the deformation potential in graphene to lie between $10 - 30$ eV [13]. However, the estimated flake area of $A \sim 100\ \mu m^2$ is not exact since there are other flakes connected to the one which is measured and whether these are near-enough to be accounted for in these electron-phonon interaction calculations is not clear.

A lower temperature bound for this disordered regime prediction is given by $(s/v_F)T_{dis} \sim 1$ K, when mean free path $l \sim 20$ nm. It would be useful for potential applications, including bolometry, to study the electron-phonon interactions below this temperature. Although in graphene devices with non-superconducting contacts, diffusion typically dominates over electron-phonon conduction pathway at lower temperatures; the graphene-STJ scheme would be particularly useful here, allowing observation of low-temperature cooling power in graphene due to phonons. From the relation $NEP_{th} = \sqrt{4k_B T^2 G}$, the intrinsic thermal noise equivalent power is calculated to be 0.8 fW/Hz$^{1/2}$ at 4.6 K.

In graphene/TiOx/NbN scheme it can be concluded that,

1. These devices clearly show bolometric response under RF radiation, with higher sensitivity and phonon dominated cooling power compared to the devices with aluminum as a superconductor.

2. Their high frequency impedance matches well with the standard RF devices/antenna, which allows high coupling efficiency.

3. Disorder in graphene plays an important role in determining the performance of these devices.

6.2 Bilayer graphene

The motivation for a graphene STJ device structure stems from the ultimate goal of these devices to be implemented for detection at THz frequencies. In a typical operating environment of such detectors [73] bath temperature is kept at $T_{t0} = 0.1$ K. Upon arrival of a THz photon pulse with energy,

$$E_{photon} = hf \sim 6.63 \times 10^{-22} \text{ J} \tag{65}$$

the temperature increase in a graphene device due to this THz photon energy pulse is given as,

$$\Delta T = \frac{E_{photon}}{C_e} \tag{66}$$

For a graphene device with a carrier density of $n \sim 10^{12}$ cm^2, electronic heat capacity can be calculated as $C_e = A \times 7 \times 10^{-10} \times T$ [38]. For a device with a graphene flake area of $A \leq 100$ μm^2 and a bath temperature of $T_{t0} = 0.1$ K, this increase is,

$$\Delta T \geq T \tag{67}$$

This prevents a linear device operation which is essential for a bolometer as a power detector in the THz regime. However, a material with a heat capacity slightly higher than graphene but still with a small area (for small phonon thermal conductance) would be able to provide a linear device operation. It can be argued though, that the electronic heat capacity in graphene can be tuned to a higher value by tuning the Fermi energy through gate voltage, it should be kept in mind that the electron phonon coupling constant Σ, also tunes linearly with Fermi energy. Hence, in order to tune the single layer heat capacity for linear device operation, sensitivity would be compromised. Another solution, can be implemented by using bilayer graphene instead. As noted in chapter 1, at a given temperature for a given chemical potential and flake area, bilayer graphene has a higher electronic heat capacity than a single layer one. Also, the electron-phonon coupling constant in bilayer graphene has an inverse square-root dependence on the chemical potential. This means that by tuning the Fermi energy to a higher value by applying a large gate voltage, low NEP can be achieved.

Single layer graphene	Bilayer graphene
$C_{e-SLG} \propto \lvert\mu\rvert$	$C_{e-BLG} \propto$ const
$\Sigma_{SLG} \propto \lvert\mu\rvert$	$\Sigma_{BLG} \propto \frac{1}{\sqrt{\lvert\mu\rvert}}$

Table 2: Comparison of heat capacity and electron-phonon coupling constant in single and bilayer graphene.

This theoretically calculated inverse dependence on chemical potential of the electron-phonon coupling constant is yet to be observed experimentally, due to a weakly temperature dependent resistance of bilayer graphene. A bilayer graphene STJ device geometry is ideal to study this prediction.

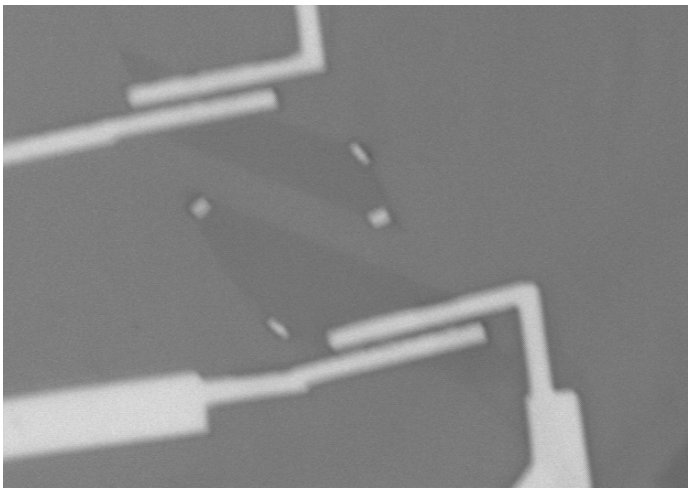

Figure 36: Magnified optical images show two bilayer graphene STJ devices with their sides clamps to prevent the flakes from rolling up. Smaller flake has an area of ~ 45 μm^2 and the larger flake area is ~ 65 μm^2. Contacts do not occupy more than 20% of the total flake area so that Fermi energy of the flake dominates.

As described in chapter 1, these devices are made with large bilayer flakes exfoliated using natural graphite. This is done so that the phonon thermal conductance, directly proportional to the flake area, dominates all other cooling contributions. These are then plasma etched into isolated, regular shaped

flakes to determine the flake area accurately, in order to minimize the error in calculation of Σ. Care is also taken to define contacts to this flake so that the metal pads do not cover more than 20% of the total flake area. This is done so that the Fermi energy in the flake is defined with not more than 20% error due to contact doping. For bilayer devices, titanium is oxidized on a hot-plate at 80°C for $\sim$ 90 min. For the particular device discussed here, the large graphene flake was broken into a smaller piece during the fabrication process and the area is reduced to $A \sim 7\ \mu\text{m}^2$. Despite this, contact resistance achieved is large enough to keep hot-electron out-diffusion small in order to allow the observation of phonon cooling contribution.

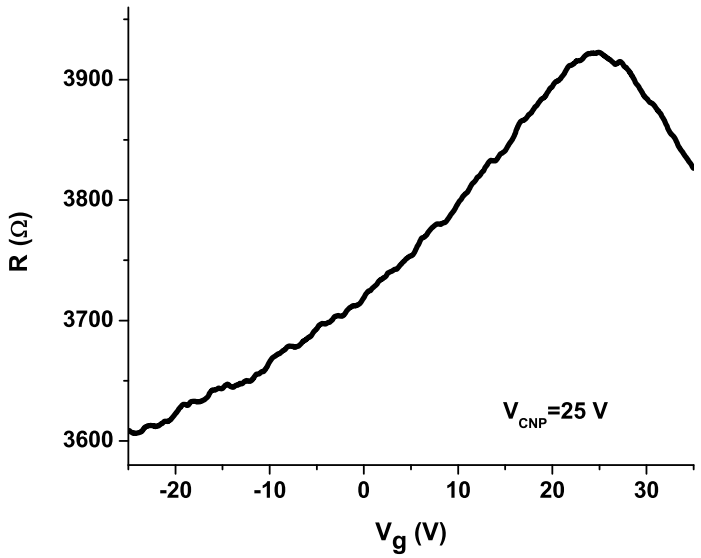

Figure 37: Gate dependent resistance of the bilayer graphene. Due to an insulating substrate, gate voltage can only be tuned above 150 K. This plot is measured at T $\sim$ 180 K, with the CNP at $V_g \sim 25$ V.

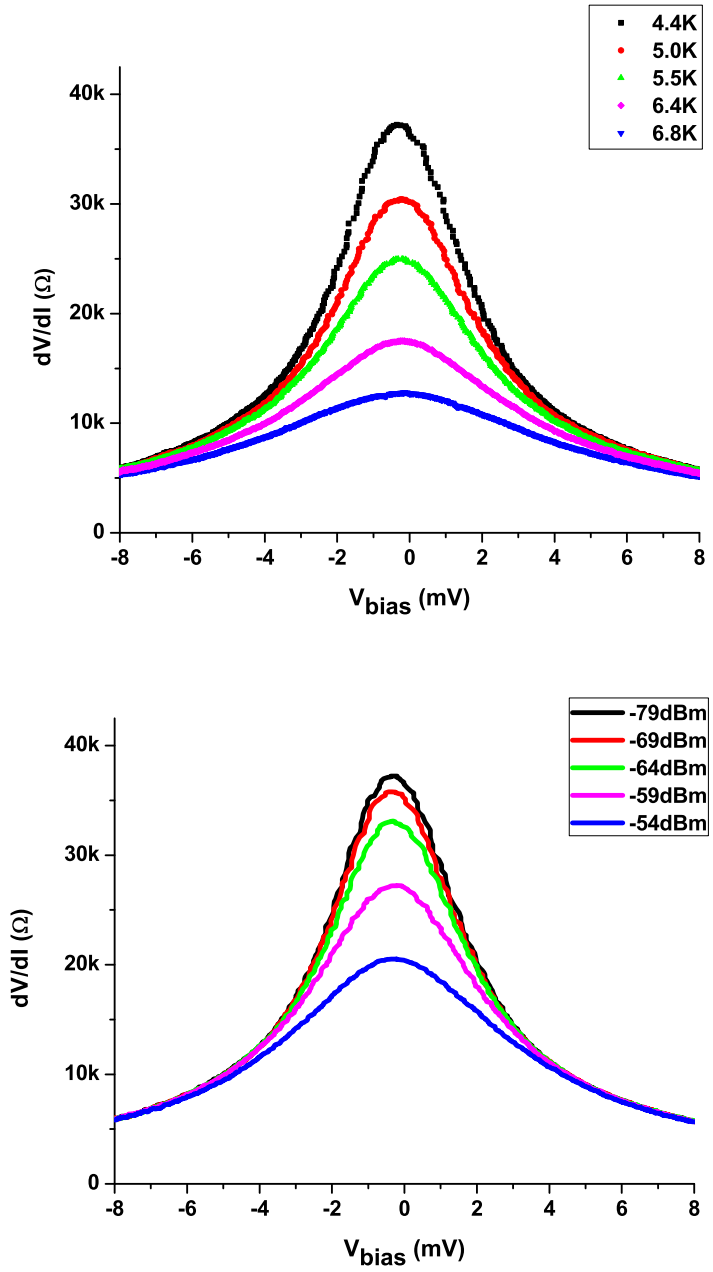

Figure 38: Differential resistance vs. junction voltage in bilayer graphene STJ devices. Comparison for differential voltage vs. voltage bias curves at different bath temperatures (top) and different applied radiation levels (bottom) for a bilayer graphene-TiOx-NbN STJ device.

Substrate used here has a lightly doped, high resistivity Si as the back layer. This prevents gating at low temperatures and makes it difficult to observe the chemical potential dependence of the electron-phonon coupling constant. This is circumvented by changing gate voltage at higher temperature where there is still finite conduction in the lightly doped Si. It is found that the gate becomes insulating below $\sim$ T $<$ 150 K. Hence, each time a power vs. temperature calibration is completed for a particular gate voltage, the device is warmed up above 150 K so that a different gate voltage can be applied. This way for the particular device described here, three different gate voltages are measured. Gating curve for this particular device is shown in Fig 37, with the charge neutrality point at $V_g \sim 25$ V.

As shown in Fig 38, for a bilayer graphene-TiOx-NbN junction similar radiation and temperature dependence of the differential resistance vs. junction voltage bias curves is observed, as that described in the previous sections for single layer graphene.

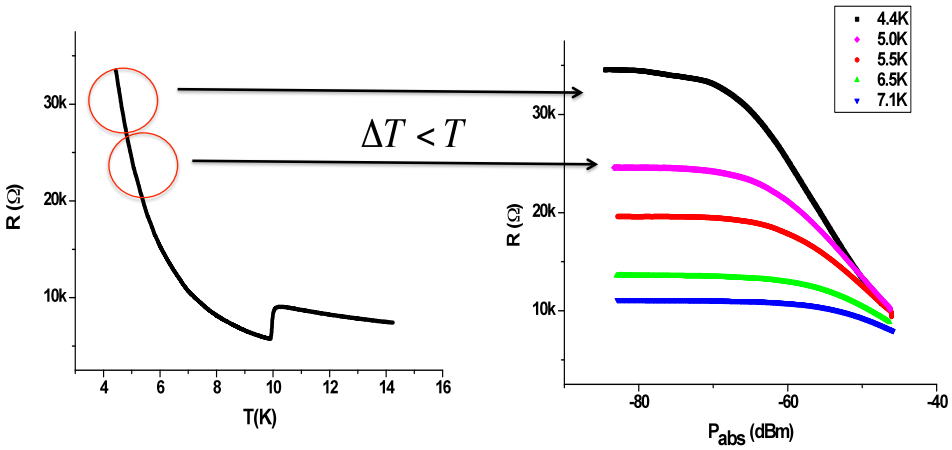

Figure 39: Piece-wise overlap scheme to maintain linear operation of the device. Base temperature is varied to measure radiation power dependence of the resistance (right) for a specific range of temperatures.

However, because of the large cooling power in a big flake, heating due to a given applied radiation power is small. To achieve a sizable hot electron temperature, a large radiation power needs to be applied. This would

increase the contribution due to the device non-linear characteristics over the bolometric effect. Also, for a correct estimation of thermal conductance from the cooling power (P) using equation:

$$G = \left.\frac{dP}{dT}\right|_{T=T_e} \tag{68}$$

it is necessary that $\Delta T_e << T_{ph}$. To ensure that this condition is satisfied, a scheme of piece-wise overlapping of differential resistance is implemented. This is different from that described in section 6.1.1, where all the radiation power is applied while keeping the bath temperature constant. In this scheme of piece-wise overlap, base temperature is varied and the radiation-induced change in the differential resistance is compared at each base temperature range. This process is outlined in Fig 39.

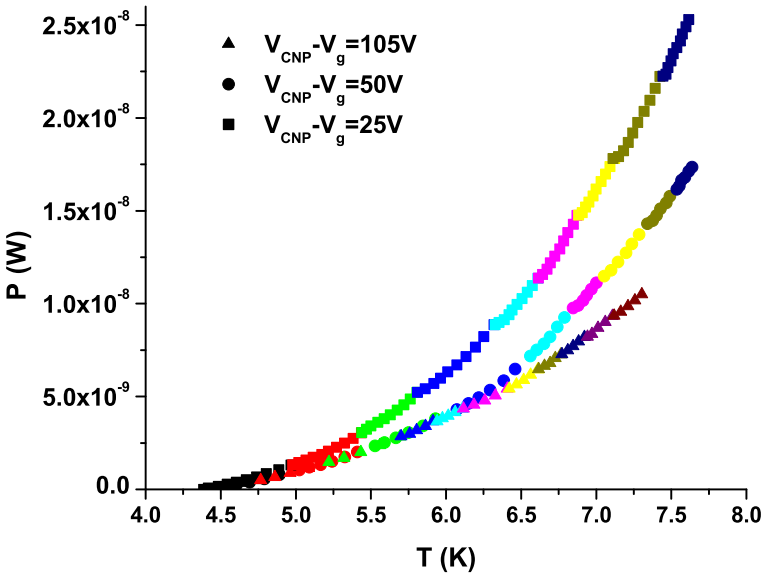

Figure 40: Gate voltage dependence of the phonon cooling power. Temperature dependence of the bilayer graphene measured cooling power is plotted at three different gate voltages, with decreasing cooling power at increasing gate voltage.

Following this procedure, a calibration of cooling power vs. temperature is obtained as shown in Fig 40. Piece-wise overlap scheme is manifested in different colored sections for Fig 40.

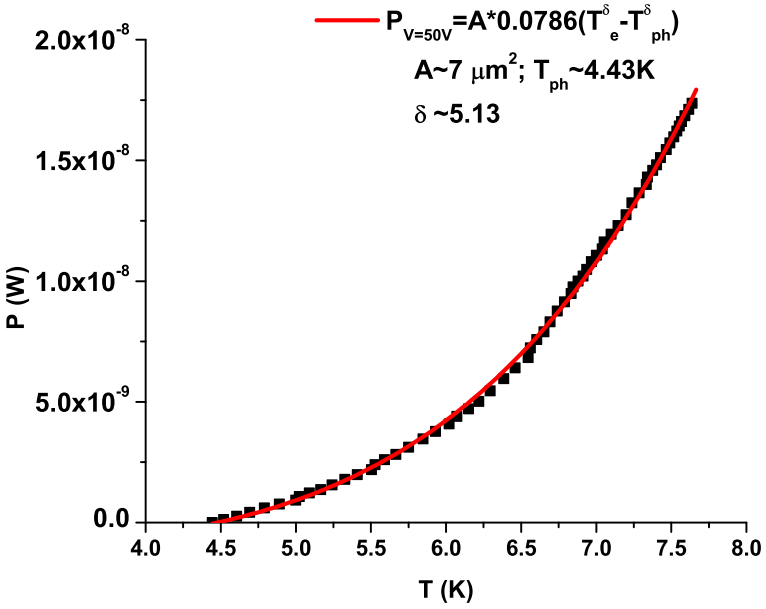

Figure 41: Measured cooling power is fitted to a T^5 temperature dependence for a plot measured at $|V_g - V_{CNP}| = 50$ V

In Fig 41, the temperature dependence is fitted to a power law of the form,

$$P = A\Sigma(T_e^\delta - T_{ph}^\delta) \tag{69}$$

which gives $\delta \sim 5$. For each gate voltage, this value of δ is observed to be different, closer to $\delta \sim 4$ for V_g away from CNP and $\delta \sim 5$ for V_g closer to CNP. This is different from the theoretically predicted behavior of $\delta = 4$ [21]. Albeit, the calculations for a bilayer graphene in ref [21] is only for a clean graphene channel at high carrier density without considering the effects of screening. Similar to the discussion above for single layer graphene, due to the presence of electron-hole puddles in a substrate-supported bilayer graphene on SiO_2, the working temperature range is maintained at $T < T_{BG-BLG}$ for all

gate voltages. Thus, it remains to be determined which mechanism is causing the modification of the temperature dependence of the phonon cooling power.

If all the plots in Fig 41 are fitted to $\delta = 5$, to extract a gate voltage dependence of Σ, it is seen that the electron-phonon coupling parameter does indeed depend on the inverse square root of gate voltage, as predicted in ref [21]. This is shown below in Fig 42.

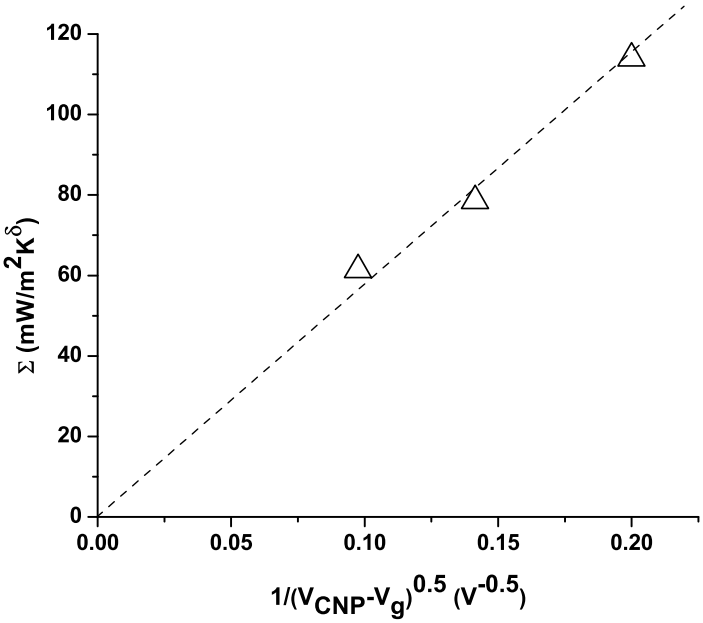

Figure 42: Gate voltage dependence of the electron-phonon coupling parameter for $\delta = 5$. It follows $\Sigma \propto 1/\sqrt{\mu}$ dependence as calculated by the theory.

Two other devices with $A = 45\ \mu\text{m}^2$ and $A = 25\ \mu\text{m}^2$, show similar temperature dependence of power.

7 Graphene-Superconductor Junctions with Transparent Contacts

Graphene-superconductor junctions with highly transparent interfaces offer unique advantages as radiation detectors [50]. At the superconductor-graphene interface, hot electrons diffusing from graphene into the superconductor are converted isothermally into holes by the Andreev reflection process, as long as their energy is within the superconducting gap [63]. This provides thermal isolation of the hot electrons, reducing the diffusion contribution to the thermal conductance allowing a high sensitivity. The Andreev reflection process, which is retro-reflective under normal circumstance, is predicted to become specular for the massless Dirac fermions in graphene. [2] These junctions have an extremely low contact resistance (of the order of few tens of Ohms), allowing the device resistance to be tuned around 50 Ω for impedance matching.

7.1 Transparent contacts fabrication

Fabrication steps for a graphene superconductor with transparent contacts, until the metal contact deposition are similar to that listed for a graphene STJ in chapter 5. First, a $\sim$ 2 nm thick Ti film is e-beam evaporated as an adhesion layer on graphene. For transparent contacts, instead of exposing the devices to air in order to oxidize Ti, as is done in case of tunnel junctions, a 1.5 nm thick Pd is deposited using electron-beam evaporation on top of the Ti film. The relatively chemically inert Pd layer is sandwiched to prevent the Ti layer from reacting with the nitrogen gas introduced during the sputtering process, as explained below. The next step is to sputter a superconductor (Nb/NbN) on top in situ. Ensuring a very good vacuum pressure in the metallization chamber (close to 2×10^{-8} torr) is essential for the fabrication of transparent contacts. Graphene -superconductor transparent contacts junctions using Pd-Al contacts are also measured. These are made using exclusively electron beam evaporation process for contact definition.

A series of tests are performed in order to understand the reaction of Ti adhesion layer with the N_2 plasma used in sputtering [65]. At a base pressure of 2×10^{-8} torr, Ti is evaporated onto graphene to form a 2 nm adhesion layer. Ar/N_2 gases are then let in for 3 min, after which the gas mixture is pumped out. Finally, a Au layer of 30 nm thickness is evaporated onto the device to

form Au/Ti contacts. Following such metallization and lift-off procedure, the contact resistance of the device is measured to be $< 300\ \Omega \cdot \mu$m, similar to that of a typical Au/Ti contacts [74] without exposure to the Ar/N_2 gases after Ti evaporation. This suggests that Ar/N_2 itself does not affect the Ti adhesion layer. By contrast, when NbN is directly sputtered on the device after the 2 nm Ti coating in Ar/N_2 plasma, the device shows much higher contact resistance of $\sim 5\ k\Omega \cdot \mu$m, suggesting the immediate reaction of Ti in the Ar/N_2 plasma upon starting of the sputter gun. This result is further proved by the fact that the contact resistance is lowered by reducing the N_2 partial pressure during the reactive sputtering. To solve the problem of $Ti - N_2$ plasma reaction, the Ti adhesion layer is coated with a 1.5 nm thick layer of Pd which is non-reactive to the N_2 plasma. Here Pd is chosen for its formation of good contact with graphene by itself [74]. As a result, a low contact resistance of $\sim 300\ \Omega \cdot \mu$m is recovered.

7.2 Measurements

Transparent graphene-superconductor weak links are used for bolometric detection of small microwave signals by directly using the DC resistance as the readout. In this device scheme, complications in calibration arising from the lack of voltage drop due to supercurrent need to be avoided. Thus, supercurrent is suppressed by making the graphene channel relatively long so that the entire graphene channel doesn't become superconducting by proximitizing. Another way to suppress supercurrent is by tuning the chemical potential close to the charge neutrality point (CNP) which increases channel resistance. Even in the absence of supercurrent, the advantages of low contact resistance, for impedance matching and high coupling efficiency and thermal confinement from the superconducting contacts are still present.

Results discussed here are from junctions made with 2 nm Pd and 30 nm Al contacts. Similar results are obtained with Ti/Pd/NbN junctions measured at higher temperatures are shown in Fig 46. The results shown below are for a device with approximately 6 μm wide Pd/Al contacts separated by $\sim 0.7\ \mu$m long graphene channel. Measurements are carried out by supplying a sweeping DC bias along with a small AC modulation of 50 nA at 13 Hz, both applied with a Keithley 6221 current source. The differential resistance (dV/dI) is measured using a lock-in amplifier, while the dc voltage is measured using Keithley 2182 nanovoltmeter. Measurements are done in a dilution refrigerator setup described in chapter 5. The RF power is de-

livered to the device through a co-axial cable at approximately 1.29 GHz, where maximum device response is recorded. The co-axial cable is located about 10 cm away from the device and no antenna is used. This allows a very small fraction of the applied power to be coupled to the devices. The high quality of the graphene-Al interface is confirmed by fabrication and characterization of a junction with leads separated by ~ 0.3 μm. At temperatures $\mathrm{T} < \mathrm{T_c}$ ($T_c \sim 1$ K being the superconducting transition temperature of Al), a well-defined supercurrent is observed in this shorter junction. Together with the pronounced features of multiple Andreev reflections, these indicate high transparency of the graphene-Al interfaces. (See Fig 43.)

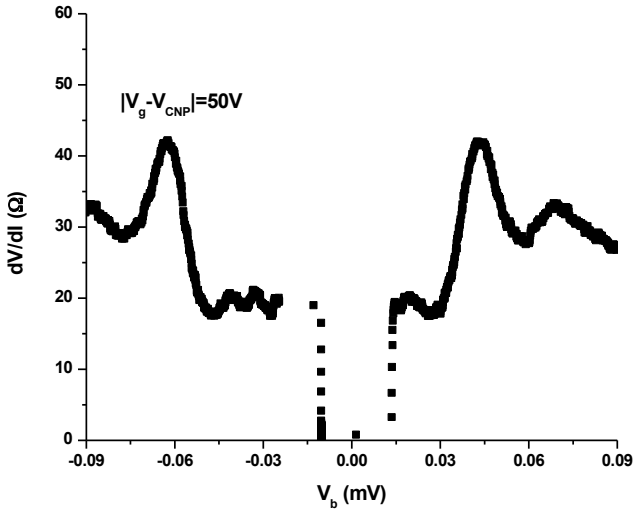

Figure 43: Developed supercurrent along with Andreev reflections in a shorter (~ 0.3 μm long) channel graphene/Pd/Al Josephson junction indicates high contact transparency.

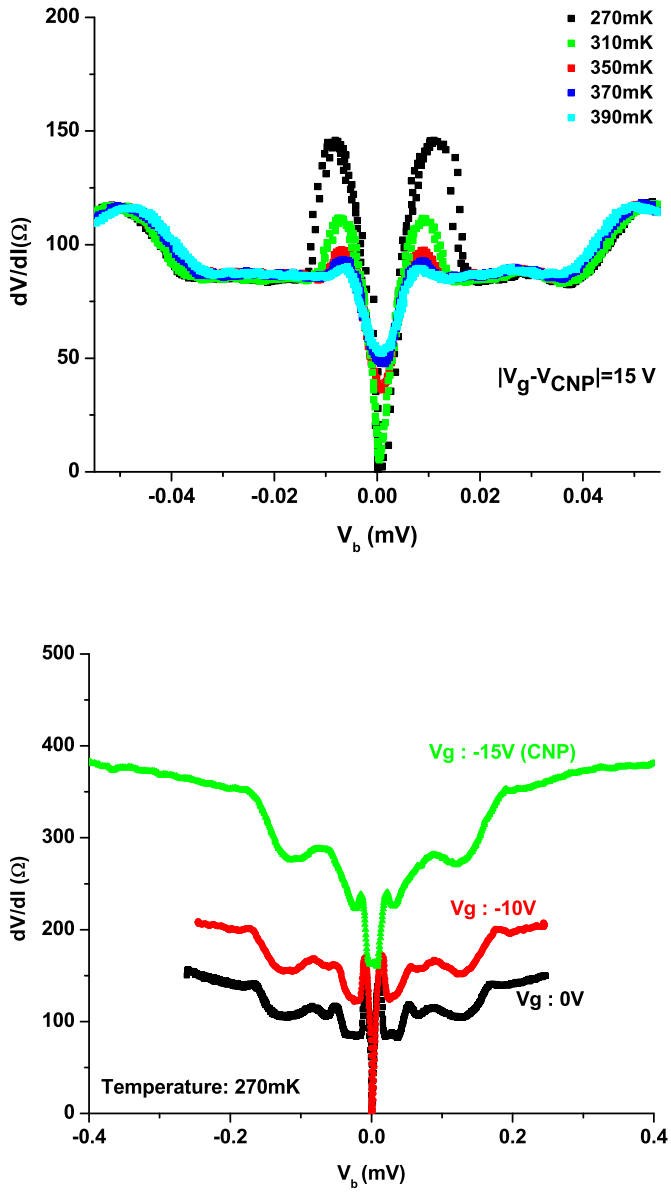

Figure 44: (top) Temperature dependence of a long channel graphene-Al Josephson junction differential resistance. (bottom) To avoid supercurrent formation, the long graphene-Al Josephson junction is gated near the CNP to increase graphene channel resistance.

With exactly the same procedure, a device with slightly larger lead separation (~ 0.7 μm) is fabricated and measured, where within a wide range of temperatures and gate voltages in the vicinity of the CNP, the supercurrent is absent. Fig 44 (top) shows dV/dI vs. bias voltage curves at different bath temperatures, for the longer channel device away from the CNP. Even with no evident supercurrent a significant reduction in zero-bias resistance along with multiple Andreev reflections is still observed, again indicating high transparency of the contacts. From Fig 44 (top), it is seen that the differential conductance changes with the temperature in the range $|V_b| < 2\Delta$ and is independent of the temperature outside the superconducting gap (Δ). As shown in Fig 44 (bottom), by applying $V_g = V_{CNP} = -15$ V and by raising the bath temperature to 320 mK the supercurrent is effectively suppressed. Here, a contact resistance of only few tens of Ohms allows the device resistance to be tuned around 50 Ω by changing channel doping or temperature. A similar scheme of characterization of the RF response in these devices is adapted as that described for a graphene STJ device, in chapter 6: by correlating the dV/dI vs. bias voltage curves in the presence of RF radiation vs. those measured at elevated bath temperatures. The response to applied radiation in dV/dI vs. bias curves is shown in Fig. 45 bottom panel. At higher applied radiation power, it is observed that the dV/dI vs. bias voltage curve develops a rather complicated behavior with oscillation-like features near zero-bias. Such features are not observed by heating the device through bath, where a temperature increase simply causes the curve to be more smeared.

7.3 Non-linear response

The origin of these features can be explained by the strong non-linearity in device response. The applied RF signal averages over a portion of the non-linear I-V curve to generate a voltage. Due to the nature of low-frequency lock-in amplifier measurements, this voltage mixes with the lock-in amplifier reference frequency. This kind of mixing produces low-frequency harmonics of the device response, which appear in the 13 Hz lock-in measurement. If this effect is greater or comparable to the device bolometric response, the outlined detection scheme of overlapping curves at different bath temperatures with curves at different radiation fails. To test this hypothesis, the lock-in amplifier response to the device I-V curve taken at 320 mK, at $V_g = -15$V, with no

radiation is simulated. The Lock-in amplifier response is given by,

$$V_{LIA} = \frac{2}{\tau} \int_0^{\tau} V_{device}(I_{applied}) \sin(\omega_{lf}) dt \tag{70}$$

where, $\omega_{lf} = 2\pi \times 13$ s^{-1} is the frequency of lock-in amplifier operation, τ is the lock-in integration time constant and $I_{applied} = I_0 \sin(\omega_{lf}) + I_{bias}$ in absence of a RF signal. (Here, $I_0 = 50$ nA). The voltage developed in the device is calculated based on the input I-V curve information through interpolation at a range of applied currents $\mathrm{I_{applied}}$, which is a superposition of a small low-frequency ac current $\mathrm{I_0}$ on a DC bias current I_{bias}. Applied radiation is mimicked by adding a high frequency current, $\mathrm{I_{RF}}$, as an external input. Then, the device response is calculated for $I_{applied} = I_0 \sin(\omega_{lf}) + I_{bias} + I_{RF} \sin(\omega_{lf})$. Observed non-linear features can be reproduced this way and it is seen that the simulated curves overlap with the ones measured to a high degree inside the superconducting gap (Fig 45). The slight mismatch at higher biases and higher radiation power could be thought of due to the small bolometric device response that is not included in the simulation.

Even though the onset of non-linearity-induced features is at a high applied RF signal, if it is taken into account that only a fraction of this signal reaches the device due to the lack of antenna and conducting substrate losses, it can be said that non-linear detection dominates the device radiation response when the device voltage is used as readout. Further exploration of graphene-superconductor junctions with highly transparent interfaces may instead focus on excitation-free readout techniques such as Johnson noise thermometry.

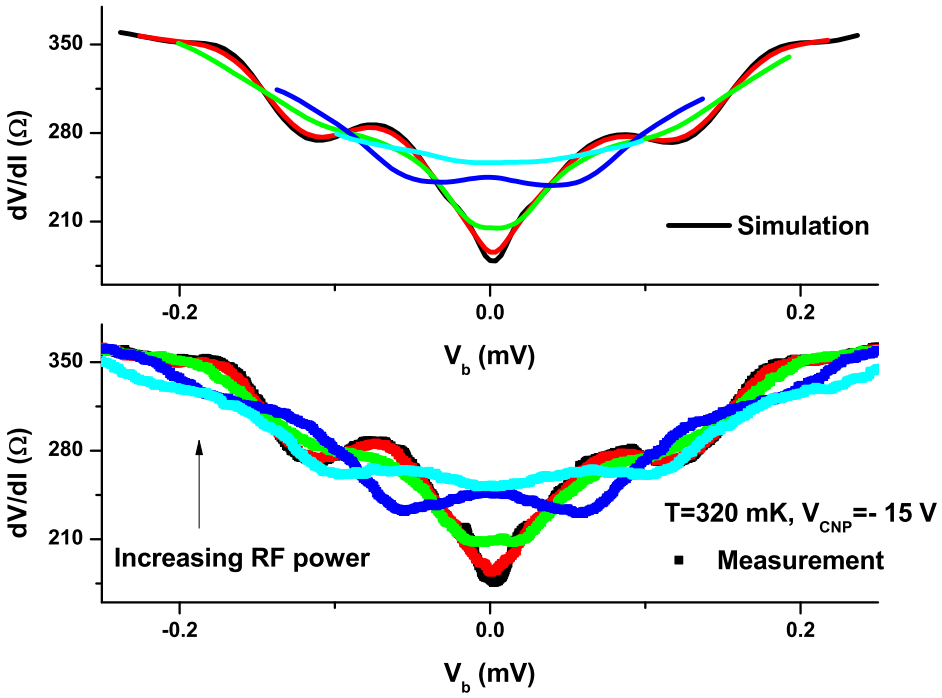

Figure 45: Device non-linearity-dominated radiation response in graphene-Pd/Al Josephson junctions. (top panel) Simulation of the lock-in amplifier response to the non-linear device I-V curve with radiation current as an external input. (bottom panel) Measured radiation device response, which does not match the temperature response of the device.

In Fig 46 similar non-linearity-induced radiation response is seen for a graphene/Ti/NbN device. Although, since these junctions are measured at higher temperatures (T $\sim$ 4.2 K), due to a higher T_c of NbN, supercurrent is not developed even far away from CNP and these non-linear features are observed.

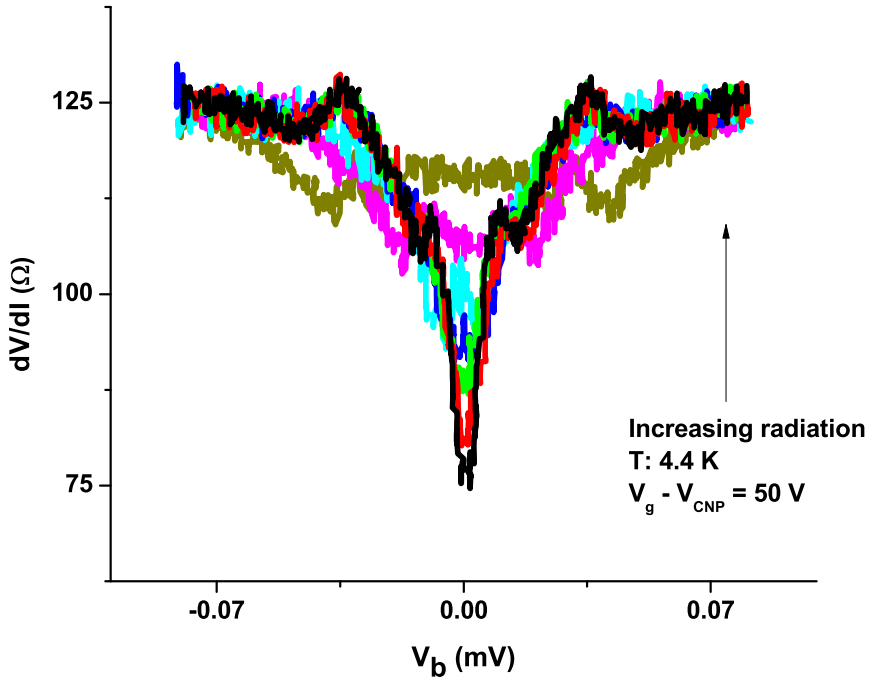

Figure 46: Device non-linearity-dominated response in graphene-superconductor Josephson junctions with NbN as a superconductor. Similar non-linearity-dominated response to radiation is found as that observed for graphene Josephson junction using Al.

8 Future of Graphene-based Bolometers

To achieve a high sensitivity bolometer device, extensive research has been carried out on graphene-based bolometers which exploit graphene's promising properties including small heat capacity, weak electron-phonon coupling, and small resistance. Focus of the theoretical efforts has been on understanding the phonon cooling mechanism from acoustic and optical phonon modes, as well as the impact of temperature, doping, and disorder on electron-phonon scattering. Experimental work is mainly channeled towards finding various approaches for measuring the electron temperature and for achieving the phonon-cooling bottleneck. At the current stage, there are still gaps in the understanding of graphene's properties such as electron-phonon coupling, important in designing a sensitive bolometer.

In this thesis, the design of graphene-superconductor junctions is presented. With the graphene-superconductor tunnel junction design, hot electrons cooling through electron-phonon interactions is demonstrated. Thus, it provides a tool to study electron-phonon interactions-dominated cooling in graphene and its dependence on disorder, chemical potential, screening etc., which is beneficial in designing a high-sensitivity bolometer as well as to design high mobility graphene devices which are ultimately limited due to phonon scattering.

The resistive readout of a graphene-based SGS Josephson junction is shown to be dominated by the highly non-linear characteristics of the device. However, advantages of this structure can be availed by using other readout methods, such as the Johnson noise measurement technique to measure electronic temperature. This work is being carried out in collaboration with the Prober Lab at Yale University by performing Johnson noise measurements at dilution temperatures on the graphene/Ti/Pd/NbN devices fabricated at Stony Brook [75]. Phonon cooling power measured in the tunnel junction devices via resistive readout at Stony Brook and via noise readout in the devices with transparent contacts at Yale has shown similar disorder-enhanced behavior [50, 75]. Further characterization of the SGS devices at temperatures < 1 K would provide an estimate on the required contact transparency to block electrons from diffusing out of the contacts in these devices. The design considerations to employ graphene-superconductor junctions with Johnson noise readout in the photon counting regime have been outlined in ref [61]. For the photon counting mode of operation, non-linear device operation may be required [38].

The observed temperature dependence of phonon cooling power in bilayer graphene needs further theoretical explanation. So far, the theory of electron-phonon interactions in bilayer graphene is developed only for the case of a clean graphene without screening effects taken into account [21]. The temperature at which effects of screening and disorder become important is yet to be established. Difference in the cooling power behavior observed in a gapped bilayer graphene bolometer [60] with an ungapped one also should be explored further. Experiments using bilayer-graphene bolometer device spanning over a much larger temperature range might be used to determine if a crossover temperature exists below which the effects of screening and/or disorder start playing an important role in electron-phonon interactions.

Even though graphene-based bolometer devices have been employed to demonstrate disorder-induced enhancement of phonon cooling power at low temperatures [50, 54, 76], it would be instructive to build a high mobility graphene-based bolometer device and observe the low temperature cooling power to follow a T^4 dependence, as predicted by the theory. Currently, this can be achieved in either of the two ways:

- **Graphene-hBN devices:** Using an atomically flat hexagonal boron nitride substrate can give higher electronic mobilities in graphene than those found in devices with SiO_2 substrate [77]. However, depending on the temperature range of the device operation, remote optical phonon energies of hBN might provide a cooling pathway [77] and care should be taken to avoid this. Experiments using graphene on hBN substrates have reported an order of magnitude lower electron-phonon coupling constant than that predicted by the theory [21, 26].

- **Suspended graphene devices:** Suspended graphene devices have been known to demonstrate some of the highest mobilities [67] and it avoids the substrate cooling channel altogether. So if in this case, hot electron diffusion through contacts has also been eliminated then the only dominant cooling will be through phonons in an extremely high mobility graphene. However, in a suspended graphene, flexural phonons are also present as an additional out-of plane mode of vibration [16]. Flexural phonons might be detrimental to the bolometer sensitivity but the study of their contribution to hot electron cooling using this device structure would provide insight into a dominant source believed to limit mobilities in suspended graphene devices.

To design a bolometric detector that meets the requirements for a particular application, calculations can be made for a range of graphene flake area that would give linear operation. For example, a SIGIS device can be considered for an application requiring a background limited sensitivity of $\mathrm{NEP_{background}} \leq 2 \times 10^{-19}$ W/$\sqrt{\mathrm{Hz}}$ at 300 GHz with an incoming photon flux of $\mathrm{N_{ph}} = 10^6$ photons/s [78]. For particular detector requirements, a solution is found by scanning the parameter phase space including graphene flake area, device operating temperature, superconducting transition temperature of the contacts, normal state device resistance, carrier density etc. which satisfy following conditions.

1. **Linearity requirements:**

   - $\Delta T < 0.1 T_0$ for linear operating regime. Here, $\Delta T = E/C$ and a typical carrier density of $n \sim 10^{12}$ cm^{-2} is assumed for the calculation of specific heat. $\mathrm{T_0}$ is the device operation temperature.
   - The resistance change from $R(T_0)/R(T_0 + \Delta T)$ is not too high so as to allow for linear device operation range. Here, the constraint chosen confines $R(T_0)/R(T_0 + \Delta T) \leq 1/2$. A normal state resistance, $R_N = 1500\ \Omega$ is assumed which increases exponentially below $\mathrm{T_c}$.

2. **Resolution requirements:** Operation is fast enough to keep up with the photon arrival rate.

$$\tau (= \frac{C}{G}) < \frac{1}{N_{ph}} \tag{71}$$

   with $\mathrm{N_{ph}} = 10^6$ photons/s.

3. **Readout requirements:**

   - Assuming the worst case scenario where the heat generated by the measurement signal is the same amount as that generated by the photon signal,

$$N_{ph} h\nu = I_{DC} V_{DC} \tag{72}$$

     For a current biased device the voltage measured should be above the amplifier noise. $\mathcal{N}$ is the available amplifier noise, typically found to be ~ 1 nV/$\sqrt{\mathrm{Hz}}$.

- $NEP_{readout} < NEP_{th}(T) < NEP_{background}$. $\mathrm{NEP_{background}}$ is calculated for operation at 300 GHz radiation frequency with a photon arrival rate of $\mathrm{N_{ph}} = 10^6$ photons/s. T is the actual device operating temperature, which includes heating due to absorption of photon power.

$$NEP_{background} = \sqrt{2N_{ph}}h\nu$$
$$NEP_{readout} = P_{photon}\frac{\mathcal{N}}{V_{dc}} \tag{73}$$

A SIGIS device (with an ideal tunnel barrier assumed) with a graphene flake of area $\sim 300\ \mu\mathrm{m}^2$, operating at ~ 0.1 K temperature is found as a solution which fulfills the conditions listed above. The time constant of this device is $\tau \sim 0.6\ \mu$s and the thermal noise equivalent power is $\mathrm{NEP_{th}} \sim 1.5 \times 10^{-19}\ \mathrm{W/Hz^{1/2}}$. These device parameters would ensure linear operation with a background-limited sensitivity. The calculations are made by assuming a clean limit phonon cooling power temperature dependence $P \propto T^4$ and $\Sigma \sim 25\ \mathrm{mW/K^4m^2}$ at a typical carrier density of $n \sim 10^{12}\ \mathrm{cm^{-2}}$.

Even though the calculations show an achievable device, however there are still discrepancies between experimentally reported values of the electron-phonon coupling constant Σ and significant technological advances are required to produce such a large area disorder-free flake of graphene.

To summarize the main achievement, the design of graphene-superconductor tunnel junctions presented here allows to study the electron-phonon interaction dominated cooling in graphene. It can also be implemented to achieve a sensitive, fast and efficient bolometer device.

References

[1] A. H. Castro Neto, F. Guinea, N. M. R. Peres, K. S. Novoselov, and A. K. Geim, Rev. Mod. Phys. **81**, 109 (2009).

[2] C. W. J. Beenakker, Rev. Mod. Phys. **80**, 1337 (2008).

[3] H. Vora, P. Kumaravadivel, B. Nielsen, and X. Du, Applied Physics Letters **100**, 153507 (2012).

[4] J. Wang and G.-Z. Liu, Phys. Rev. D **85**, 105010 (2012).

[5] T. Stauber, N. M. R. Peres, and F. Guinea, Phys. Rev. B **76**, 205423 (2007).

[6] T. Ando, Journal of the Physical Society of Japan **75**, 074716 (2006).

[7] F. T. Vasko and V. Ryzhii, Phys. Rev. B **76**, 233404 (2007).

[8] M. Katsnelson and A. Geim, Philosophical Transactions of the Royal Society A: Mathematical, Physical and Engineering Sciences **366**, 195 (2008).

[9] S. Datta, *Electronic transport in mesoscopic systems* (Cambridge university press, 1997).

[10] A. K. Geim and K. S. Novoselov, Nature materials **6**, 183 (2007).

[11] L. Malard, M. Pimenta, G. Dresselhaus, and M. Dresselhaus, Physics Reports **473**, 51 (2009), ISSN 0370-1573.

[12] R. Bistritzer and A. H. MacDonald, Phys. Rev. Lett. **102**, 206410 (2009).

[13] E. H. Hwang and S. Das Sarma, Phys. Rev. B **77**, 115449 (2008).

[14] E. V. Castro, H. Ochoa, M. I. Katsnelson, R. V. Gorbachev, D. C. Elias, K. S. Novoselov, A. K. Geim, and F. Guinea, Phys. Rev. Lett. **105**, 266601 (2010).

[15] H. Ochoa, E. V. Castro, M. I. Katsnelson, and F. Guinea, Phys. Rev. B **83**, 235416 (2011).

[16] E. Mariani and F. von Oppen, Phys. Rev. Lett. **100**, 076801 (2008).

[17] J.-H. Chen, C. Jang, S. Xiao, M. Ishigami, and M. S. Fuhrer, Nature nanotechnology **3**, 206 (2008).

[18] W. Chen and A. A. Clerk, Phys. Rev. B **86**, 125443 (2012).

[19] J. M. Dawlaty, S. Shivaraman, M. Chandrashekhar, F. Rana, and M. G. Spencer, Applied Physics Letters **92**, 042116 (2008).

[20] D. Sun, Z.-K. Wu, C. Divin, X. Li, C. Berger, W. A. de Heer, P. N. First, and T. B. Norris, Phys. Rev. Lett. **101**, 157402 (2008).

[21] J. K. Viljas and T. T. Heikkilä, Phys. Rev. B **81**, 245404 (2010).

[22] F. C. Wellstood, C. Urbina, and J. Clarke, Phys. Rev. B **49**, 5942 (1994).

[23] D. K. Efetov and P. Kim, Phys. Rev. Lett. **105**, 256805 (2010).

[24] S. S. Kubakaddi, Phys. Rev. B **79**, 075417 (2009).

[25] W.-K. Tse and S. Das Sarma, Phys. Rev. B **79**, 235406 (2009).

[26] A. C. Betz, F. Vialla, D. Brunel, C. Voisin, M. Picher, A. Cavanna, A. Madouri, G. Fève, J.-M. Berroir, B. Plaçais, et al., Phys. Rev. Lett. **109**, 056805 (2012).

[27] K. C. Fong and K. C. Schwab, Phys. Rev. X **2**, 031006 (2012).

[28] H. Min, E. H. Hwang, and S. Das Sarma, Phys. Rev. B **83**, 161404 (2011).

[29] J. C. W. Song, M. Y. Reizer, and L. S. Levitov, Phys. Rev. Lett. **109**, 106602 (2012).

[30] A. Betz, S. H. Jhang, E. Pallecchi, R. Ferreira, G. Fève, J.-M. Berroir, and B. Plaçais, Nature Physics **9**, 109 (2013).

[31] M. W. Graham, S.-F. Shi, D. C. Ralph, J. Park, and P. L. McEuen, Nature Physics **9**, 103 (2013).

[32] E. McCann and M. Koshino, Reports on Progress in Physics **76**, 056503 (2013).

[33] M. Freitag, Nature Physics **7**, 596 (2011).

[34] J. Zmuidzinas and P. Richards, Proceedings of the IEEE **92**, 1597 (2004), ISSN 0018-9219.

[35] K. S. Novoselov, A. K. Geim, S. V. Morozov, D. Jiang, Y. Zhang, S. V. Dubonos, I. V. Grigorieva, and A. A. Firsov, Science **306**, 666 (2004).

[36] S. Langley, Proc. Am. Ac. Arts Sci. **342** (1881).

[37] P. L. Richards, Journal of Applied Physics **76**, 1 (1994).

[38] X. Du, D. E. Prober, H. Vora, and C. B. Mckitterick, Graphene and 2D Materials **1** (2014).

[39] R. Wood, *Use of vanadium oxide in microbolometer sensors* (1995), uS Patent 5,450,053.

[40] A. Rogalski, *Infrared detectors* (CRC Press, 2010).

[41] M. J. E. Golay, Review of Scientific Instruments **18**, 347 (1947).

[42] A. W. Blain, I. Smail, R. Ivison, J.-P. Kneib, and D. T. Frayer, Physics Reports **369**, 111 (2002), ISSN 0370-1573.

[43] J. Wei, D. Olaya, B. S. Karasik, S. V. Pereverzev, A. V. Sergeev, and M. E. Gershenson, Nature Nanotechnology **3**, 496 (2008).

[44] M. C. Beard, G. M. Turner, and C. A. Schmuttenmaer, The Journal of Physical Chemistry B **106**, 7146 (2002).

[45] P. K. Day, H. G. LeDuc, B. A. Mazin, A. Vayonakis, and J. Zmuidzinas, Nature **425**, 817 (2003).

[46] G. N. Gol'tsman, O. Okunev, G. Chulkova, A. Lipatov, A. Semenov, K. Smirnov, B. Voronov, A. Dzardanov, C. Williams, and R. Sobolewski, Applied Physics Letters **79**, 705 (2001).

[47] S. V. Morozov, K. S. Novoselov, M. I. Katsnelson, F. Schedin, D. C. Elias, J. A. Jaszczak, and A. K. Geim, Phys. Rev. Lett. **100**, 016602 (2008).

[48] J. D. Chudow, D. F. Santavicca, C. B. McKitterick, D. E. Prober, and P. Kim, Applied Physics Letters **100**, 163503 (2012).

[49] D. E. Prober, Applied Physics Letters **62**, 2119 (1993).

[50] H. Vora, B. Nielsen, and X. Du, Journal of Applied Physics **115**, 074505 (2014).

[51] D. R. Schmidt, R. J. Schoelkopf, and A. N. Cleland, Phys. Rev. Lett. **93**, 045901 (2004).

[52] X. Du, I. Skachko, and E. Y. Andrei, Phys. Rev. B **77**, 184507 (2008).

[53] H. B. Heersche, P. Jarillo-Herrero, J. B. Oostinga, L. M. Vandersypen, and A. F. Morpurgo, Nature **446**, 56 (2007).

[54] I. V. Borzenets, U. C. Coskun, H. T. Mebrahtu, Y. V. Bomze, A. I. Smirnov, and G. Finkelstein, Phys. Rev. Lett. **111**, 027001 (2013).

[55] A. Shailos, W. Nativel, A. Kasumov, C. Collet, M. Ferrier, S. Guéron, R. Deblock, and H. Bouchiat, EPL (Europhysics Letters) **79**, 57008 (2007).

[56] P. Rickhaus, M. Weiss, L. Marot, and C. Schönenberger, Nano Letters **12**, 1942 (2012).

[57] J. Voutilainen, A. Fay, P. Häkkinen, J. K. Viljas, T. T. Heikkilä, and P. J. Hakonen, Phys. Rev. B **84**, 045419 (2011).

[58] Y. Li and N. Mason, Applied Physics Letters **102**, 023102 (2013).

[59] C. E. Malec and D. Davidović, Journal of Applied Physics **109**, 064507 (2011).

[60] J. Yan, M. Kim, J. Elle, A. Sushkov, G. Jenkins, H. Milchberg, M. Fuhrer, and H. Drew, Nature nanotechnology **7**, 472 (2012).

[61] C. B. McKitterick, D. E. Prober, and B. S. Karasik, Journal of Applied Physics **113**, 044512 (2013).

[62] M. Tinkham, *Introduction to superconductivity* (Courier Dover Publications, 2012).

[63] A. Andreev, Sov. Phys. JETP **22**, 18 (1966).

[64] C. W. J. Beenakker, Phys. Rev. Lett. **97**, 067007 (2006).

[65] N. Mizuno, B. Nielsen, and X. Du, Nature communications **4** (2013).

[66] G. E. Blonder, M. Tinkham, and T. M. Klapwijk, Phys. Rev. B **25**, 4515 (1982).

[67] X. Du, I. Skachko, A. Barker, and E. Y. Andrei, Nature nanotechnology **3**, 491 (2008).

[68] A. C. Ferrari, J. C. Meyer, V. Scardaci, C. Casiraghi, M. Lazzeri, F. Mauri, S. Piscanec, D. Jiang, K. S. Novoselov, S. Roth, et al., Phys. Rev. Lett. **97**, 187401 (2006).

[69] S. Yasin, D. Hasko, and H. Ahmed, Microelectronic engineering **61**, 745 (2002).

[70] C. Chang, D. Fraser, M. Grieco, T. Sheng, S. Haszko, R. Kerwin, R. Marcus, and A. Sinha, Journal of The Electrochemical Society **125**, 787 (1978).

[71] B. Fallahazad, K. Lee, G. Lian, S. Kim, C. M. Corbet, D. A. Ferrer, L. Colombo, and E. Tutuc, Applied Physics Letters **100**, 093112 (2012).

[72] N. Iosad, T. Klapwijk, S. N. Polyakov, V. V. Roddatis, E. K. Kov'ev, and P. Dmitriev, Applied Superconductivity, IEEE Transactions on **9**, 1720 (1999), ISSN 1051-8223.

[73] B. Karasik, A. Sergeev, and D. Prober, Terahertz Science and Technology, IEEE Transactions on **1**, 97 (2011), ISSN 2156-342X.

[74] F. Xia, V. Perebeinos, Y.-m. Lin, Y. Wu, and P. Avouris, Nature nanotechnology **6**, 179 (2011).

[75] C. McKitterick, H. Vora, X. Du, B. Karasik, and D. Prober, Journal of Low Temperature Physics **176**, 291 (2014), ISSN 0022-2291.

[76] K. C. Fong, E. E. Wollman, H. Ravi, W. Chen, A. A. Clerk, M. D. Shaw, H. G. Leduc, and K. C. Schwab, Phys. Rev. X **3**, 041008 (2013).

[77] C. Dean, A. Young, I. Meric, C. Lee, L. Wang, S. Sorgenfrei, K. Watanabe, T. Taniguchi, P. Kim, K. Shepard, et al., Nature nanotechnology **5**, 722 (2010).

[78] B. Karasik and A. Sergeev, Applied Superconductivity, IEEE Transactions on **15**, 618 (2005), ISSN 1051-8223.